

**Granular Sloshing Absorbers
for Vibration Control**

Sergiu Ciprian Dragomir

A thesis submitted to Victoria University for the Doctor of Philosophy
Degree (Mechanical Engineering)

2011

ACKNOWLEDGEMENTS

I would like to thank the supervisors of this thesis, Dr. Eren Semercigil and Dr. Özden Turan. They have been a constant source of support and patience, and always provided a way out when I got stuck. Additionally they entrusted me with tremendous amounts of freedom, which has helped me transition from an undergraduate student and into an engineer and a scientist.

I would like to thank Drs. Semercigil and Turan for the initial concept of this project and for their guidance through experimental setups and methodologies.

I would like to also thank the thesis co-supervisor from CSIRO, Dr. Matthew Sinnott. His contribution has been critical in obtaining and analysing the numerical results presented in Chapters 2, 3 and 5. Through his help, I am also thankful for access to the CSIRO computing facilities, which provided all of the number crunching required for the numerical work.

I would like to thank Professor Greg Baxter for his co-supervision and cooperation in getting the thesis through the last couple of hurdles encountered.

During my candidature I was a recipient of a Faculty of Health Engineering and Science Postgraduate Research Scholarship at Victoria University. This financial support was greatly appreciated and made this research possible.

I would also like to thank my parents for their support and belief in me throughout these past few years. Without that belief I would never have started and then finished what is likely to be one of my greatest personal accomplishments.

Last, but not least, I would like to thank my wife, Camelia, for her unwavering support during the time of my candidature. She was a source of inspiration, strength and joy. However, the greatest joy was seeing the first smile on my daughter's face. While you are still young, you have given me strength and determination at the most difficult of times, and for that I thank you, Sienna Clarisse.

Sergiu Ciprian Dragomir

ABSTRACT

Tall, flexible structures may be exposed to excessive oscillations when subjected to wind, earthquakes or other shocks. Passive and active absorbers are employed, often at great expense, to stabilise the structures for the safety and comfort of the occupants. Current passive damper technologies include Tuned Mass Dampers and Tuned Liquid Dampers. These devices provide optimal damping at the natural frequency of the structure.

This thesis proposes a novel passive damping device, that uses a granular material sloshing in a rotating cylindrical container as the energy sink. Tuning of a granular sloshing absorber is shown to be effective using a laboratory prototype, increasing the inherent damping of the structure by two orders of magnitude with an added mass of about 1%. The energy dissipation is found to be dependent on granular material properties and speed of rotation. A numerical model is also developed and validated, and can be used as a design tool for a large scale absorber.

In this thesis a new and innovative passive damper design is proved on a small prototype and numerical tools required to implement a real device are developed. These tools can be used to create safer infrastructure or more comfortable buildings.

Table of Contents

ACKNOWLEDGEMENTS	ii
ABSTRACT	iv
TABLE OF CONTENTS	v
LIST OF TABLES	viii
LIST OF FIGURES	ix
Chapter 1	1
Introduction	
Chapter 2	5
Energy Dissipation Characteristics of Particle Sloshing in a Rotating Cylinder	
2.1 Introduction	5
2.2 Experimental Work	8
2.2.1 Experimental Setup	8
2.2.2 Experimental Observations	11
2.2.2.1 General Motion	11
2.2.2.2 Roll without slip	14
2.3 Numerical Model	16
2.3.1 Discrete Element Method	17

2.3.2 Numerical Predictions	21
2.4 Conclusions	27
Chapter3	29
Critical speed and energy dissipation in a rotating cylinder	
3.1 Introduction	29
3.2 Experiments	33
3.3 Numerical model	35
3.4 Comparison of the predicted and observed critical speeds	39
3.5 Comparison of the predicted and observed particle distribution	41
3.6 Further flow details from numerical simulations	42
3.7 Parametric Study	49
3.8 Conclusions	58
Chapter 4	61
Experiments to control structural vibrations with granular flow damper	
4.1 Introduction	61
4.2 Experimental Setup	64
4.3 Structural damping	66

4.4 Effect of tuning – change in radius of curvature for ramp	71
4.5 Effect of initial displacement	75
4.6 Conclusions	77
Chapter 5	79
Energy dissipation characteristics of a granular flow damper	
5.1 Introduction	79
5.2 Discrete Element Method – dynamic object	80
5.3 Numerical Predictions and Comparisons	82
5.4 Energy Dissipation Events	86
5.5 Conclusions	89
Chapter 6	90
Conclusion	
Appendix A: Particle Based Energy Sink	93
Appendix B: Damped Tuned Vibration Absorbers	119
References	126

List of Tables

Table 2.1: Container properties.

Table 2.2: Particle properties given as ranges and averages of 16 particles. Values for Particle 4, sand, are approximations based on high resolution pictures of the particles used. All other particle measurements have error margins of ± 0.5 mm.

Table 3.1. Levels of the three design parameters.

Table 3.2. Standard Response Table of the three design parameters on the critical speed.

Table 4.1: Experimental parameters.

Table A1: Ramp properties.

Table A2: Container properties.

Table A3: Particle properties.

Table A4: Summary of experiments.

List of Figure Captions

Figure 2.1: Schematic of experimental setup, showing stopping distance X along surface, ramp and bump-stop.

Figure 2.2: Depiction of 15 particles of each type. (1) lentils; (2) soy beans; (3) broad beans; (4) sand. The inset represents a close-up of Particle 4.

Figure 2.3: Variation of the stopping distance, X , with fill level for containers 1 (1.1L), 2 (0.5L) and 3 (0.625L). All experiments use Ramp 1, Particle 2 on glass surface.

Figure 2.4: Effect of particle size and shape 1 (lentil), 2 (soy bean) and 3 (broad bean). All experiments with Ramp 1 and Container 3 on glass surface.

Figure 2.5: Comparison between Particles 1 (lentil); 2(soy bean) and 4(sand) for (almost perfect) roll.

Figure 2.6: Comparison between Particles 1 (lentil); 2(soy bean) and 4(sand) for potential energy.

Figure 2.7: Normal and tangential elastic and dissipative elements used to evaluate contact forces.

Figure 2.8: Super-quadric shapes for (a) $n = 2$, (b) $n = 2.5$, (c) $n = 3.0$, (d) $n = 4.0$, (e) $n = 5.0$, and (f) $n = 10$.

Figure 2.9: Sample container locations for the simulation (above) and experiment (below) at 160-ms intervals. Simulation particles coloured by speed from stationary (blue) to 1.5 m/s (red).

Figure 2.10: Comparison of experimental and numerically predicted surface shapes. The first row of each group is a schematic illustration of the photographs from the experiment shown in the second row. The third row contains the corresponding DEM predictions. The same results are coloured using the same scale as in Figure 2.9.

Figure 2.11: History of instantaneous energy dissipation.

Figure 2.12: Energy dissipation for the first event in Figure 2.11. Top row is for the normal direction, and the bottom row for the tangential direction.

Figure 2.13: Energy dissipation for the second event in Figure 2.11.

Figure 2.14: Energy dissipation for the third event in Figure 2.11.

Figure 3.1: Schematic representation of the suggested rotating absorber with granular flow.

Figure 3.2: Photograph of the experimental setup on the left and its schematic representation on the right, with the electric motor (1), belt (2), bearings (3), container (4), granular material (5) and camera (6).

Figure 3.3 (a) Frame from experimental video recording, where the light background and container markings are shown. Slight skew due to high speed container rotation is also apparent. (b) Frame from experimental video recording, where the dark background denotes that the material has centrifuged.

Figure 3.4: Numerical determination of the centrifuging speed. (a), (b) and (c) Granular material flow just prior to and immediately after centrifuging occurs. (d) Average number of near neighbors, a DEM variable, increases considerably when centrifuging occurs in a rotating container.

Figure 3.5: (a) Variation of energy dissipation with tangential speed of the container boundary, and velocity contours for just before (b) and (c) and immediately after centrifuge (d).

Figure 3.6: Variation of normalized critical speed with fill level. Triangles represent experiments with centrifuging particles, circles indicate numerical results with centrifuging particles and filled circles numerical results where particles do not centrifuge.

Figure 3.7: Comparison between the time-averaged granular flow from the DEM numerical simulations colored by particle speed (left) and experiment recordings (right) for the 16% fill level at 20 rad/s

Figure 3.8: Variation of energy dissipation with boundary speed for 5%, 10%, 15% and 20% fill levels. Final data point denotes a simulation where centrifuging occurs.

Figure 3.9 Variation of percentage shear dissipation of total energy dissipation for different boundary speeds

Figure 3.10 Comparison between energy dissipation through inter-particle collisions (a) and energy dissipation involving the boundary (b)

Figure 3.11 Graphical representation of energy dissipation. (a) and (b): 2D image of normal and tangential dissipation, averaged over the third dimension. (c), (d), (e) and (f): comparisons of energy dissipation for different boundary speeds averaged along the vertical (Y) and horizontal (X) axes for the normal and tangential collision components, respectively. CrV is the critical speed $\sqrt{g/r}$.

Figure 3.12: Energy dissipation for a system where the speed is increased in discrete steps.

Figure 3.13: Direct effects of material properties, ρ , e and μ , on the critical speed, N_c

Figure 3.14: Variation of the critical speed with (a) e at three different levels of μ , (b) e at different levels of ρ , and (c) μ at different levels of ρ

Figure 3.15: The variation of the critical speed N_c with the angle of repose, θ . The predicted N_c from Equation 2, and the standard balance of centrifugal and gravitational accelerations are marked, along with the discrete points from the current study.

Figure 4.1: Schematic representation of proposed absorber design.

Figure 4.2: (a) Photograph of experimental setup. (b) Schematic representation of experimental setup with metal strip (1), platform (2), ramp (3), cylinder and particles (4) and bump stop (5) marked.

Figure 4.3: Undamped structure, with critical damping coefficient of 0.01% .

Figure 4.4: Structure with empty cylinder as controller. The double beat indicates energy transfer to the cylinder which is then returned to the structure since there is no damper.

Figure 4.5: Structure with cylinder filled to 1% as controller. Energy dissipation occurs quickly over the first two cycles. Remaining oscillations are due to imperfect tuning of structure and ramp/cylinder frequency.

Figure 4.6: System critical damping plotted against cylinder fill level over the first three cycles. Dark line represents the first six positive peaks, while light line represents the first six negative peaks.

Figure 4.7: Natural frequency changes with ramp configuration. Natural frequencies of structure with larger diameter ramps are similar, while natural frequency for structure with small diameter ramp is clearly higher.

Figure 4.8: Critical damping plotted against cylinder fill level for three ramp configurations over the first three cycles. Solid lines represent the positive peaks while dotted lines represent negative peaks.

Figure 4.9: Comparison of displacement for highest dissipation over three cycles for the three ramps. Solid line represents the tuned ramp, dotted line represents the small diameter ramp while the dashed line ramp represents the large diameter ramp.

Figure 4.10: Performance of absorber given a greater initial displacement. Solid lines represent the positive peaks while dotted lines represent the negative peaks. Lighter colors indicate greater number of cycles.

Figure 4.11: Performance of absorber for different initial displacements with the tuned ramp.

Figure 5.1: Diagram of the rolling cylinder, ramp and the relevant forces. Global coordinates are x,y . Local coordinates are n,t .

Figure 5.2: Motion of cylinder down ramp for specified case (top), dynamic model (middle) and for experiment (bottom).

Figure 5.3: Histories of the container x and y position for the specified and dynamic motion cases.

Figure 5.4: Histories of the container x and y velocity for the specified and dynamic motion cases.

Figure 5.5: History of the container angular speed for the specified and dynamic motion cases.

Figure 5.6: History of the input power to the system due to the particle torque on the container boundary for the dynamic case (red) and the specified case (black).

Figure A1: Schematic representation of a design for proposed granular sloshing absorber.

Figure A2 (a): Ramp 3, with no-slip surface attached. (b): Schematic of Experimental Setup, showing (1) surface, (2) angle between wedge and surface, (3) wedge, (4) container and (5) bump stop. X represents distance travelled by container on surface.

Figure A3: Depiction of 15 particles of each type. (1) lentils; (2) soy beans; (3) broad beans; (4) sand.

Figure A4: Effect of container and ramp. $\text{---}\blacksquare\text{---}$ Container 1, Ramp 1; $\text{---}\blacklozenge\text{---}$ Container 1, Ramp 2; $\text{---}\blacklozenge\text{---}$ Container 2, Ramp 1; $\text{---}\blacktriangle\text{---}$ Container 2, Ramp 2. Vertical axis represents X , the distance travelled by the container. Horizontal axis represents the number of particles in the container, measured as a percentage of the container capacity. All experiments with Particle 2, on glass surface.

Figure A5: Effect of Containers 1, 2 and 3. —◆— Container 1; —▲— Container 2; —■— Container 3. All experiments with Ramp 2, Particle 2 on glass surface. Axes are the same as in Figure A4.

Figure A6: Effect of Particles. —◆— Lentil; —■— Bean; —▲— Broad Bean. All experiments use Container 3, Ramp 2 and glass surface. The axes describe the same quantities as in Figure A4.

Figure A7: Effect of Surface. —■— Hard wood polished floor; —▲— carpet. All experiments with Container 3, Particle 2 and Ramp 4. Axes represent the same dimensions as in Figure A5.

Figure A8: Comparison between perfect slide and perfect roll. —◆— Perfect slide; —■— Perfect roll, long rubber; —▲— Perfect roll, short rubber. The axes represent the same dimensions as previous figures, however X has twice the scale of Figures A4 to A7. All experiments use lentils, and Containers 3 and 4, which are identical. Ramp for perfect roll is Ramp 3.

Figure A9: Potential Energy graph of Figure 8. The added mass of the car shows little change in potential energy. The Incident Energy is approximated to be the Potential Energy of the container when at rest, at the top of the ramp.

Figure A10: Effect of rubber on ramp. —◆— Long rubber; —■— Short rubber; —▲— No rubber. All experiments with Particle 1, Ramp 4 and Container 3. Ramp leads onto polished floor. Axes represent the same quantities as in Figure A4. The scale of X is the same as in Figure A8.

Figure A11: Comparison of particles with rubber covered ramp. —■— Particle 1; —▲— Particle 2; —◆— Particle 4. All experiments with Ramp 4, covered with 50 cm. of rubber, using Container 3, on polished floor boards. Axes represent the same dimensions as Figure A4, however X range is between 0 and 80 cm, which is half the range in Figure A4

Figure A12: Comparison of Incident Energies for Figure 11. $\text{---}\blacksquare\text{---}$ Particle 1; $\text{---}\blacktriangle\text{---}$ Particle 2; $\text{---}\blacklozenge\text{---}$ Particle 4. The Incident Energy is approximated to be the Potential Energy of the container when at rest, at the top of the ramp.

Figure A13 (a): front view of the leading wavefront, (b) side view of the container, including the amplitude of both the leading and trailing wavefronts.

Figure A14 (a): front view of leading wave front at times (t+1), (t+2) and (t+3), (b): side view of both wave fronts at times (t+1), (t+2), (t+3) and (t+5).

Figure A15 (a) amplitude of leading and trailing waves at times (t+2) and (t+7) as well as particle level when at rest. (b) side view of particles in container at times (t+2) and (t+7).

Figure B1: (a) Schematic representation of system to be controlled m_1, k_1 and absorber m_2, k_2 and (b) response amplitude X_1 of m_1 with (---) and without the absorber (- -), as a function of excitation frequency ratio.

Figure B2: (a) Schematic representation of system to be controlled m_1, k_1 and damped absorber m_2, k_2, c_2 and (b) response amplitude of m_1 with damped absorber (----), with undamped absorber (-- --), and without absorber (--.--)

Figure B3: Schematic showing a sloshing absorber attached on a single degree of freedom mechanical oscillator

I, Sergiu Dragomir, declare that the PhD thesis entitled “Granular Sloshing Absorbers for Vibration Control” is no more than 100,000 words in length including quotes and exclusive of tables, figures, appendices, bibliography, references and footnotes. The thesis contains no material that has been submitted previously, in whole or in part, for the award of any other academic degree or diploma. Except where otherwise indicated, this thesis is my own work.

Copyright in all images and text is retained by the Author and reproduction is governed by the *Copyright Act 1968 (Cth)*.

Signature

Date

1 Introduction

Modern tall structures such as buildings, communication towers and suspension bridges are flexible and may require additional damping for structural safety and occupant comfort. In this thesis, a novel vibration damper is introduced that uses a granular material sloshing inside a rotating cylinder as an energy sink. This is a passive damper design that can be tuned to the natural frequency of the structure. The objectives of the research are to prove feasibility of this damper, determine factors affecting level of energy dissipation, prove performance with a laboratory prototype, and show that Discrete Element Method (DEM) can be employed as a viable design tool to represent the granular motion.

In this chapter, a range of different vibration dampers are briefly discussed, then the goals and relevance of each of the following thesis chapters are defined. These following chapters are all self-contained entities, including their relevant literature review. Hence, no particular references are cited here.

Tuned mass dampers (TMD) are a popular choice as controllers for flexible structures. They consist of a secondary oscillator attached to the primary structure to be controlled. Tuning is achieved by selection of the natural frequency of the secondary structure to be the same as a critical frequency of the primary structure. These devices provide excellent control at the critical tuning frequency of the structure. However, they may be ineffective at other frequencies unless damping is included in their design. This damping can be as high as 20% of critical, and requires maintenance by its inherent nature. A more in-depth treatment of the principles of operation for the tuned mass dampers is covered in Appendix B.

Another passive damping technique uses a liquid sloshing to act as absorber. Sloshing absorbers are a lower cost alternative to tuned mass dampers, both in set-up and maintenance. These devices use a liquid, usually water, in an enclosed container. Tuning is achieved through selection of container dimensions and liquid level. A more detailed discussion of tuned liquid dampers and their uses are given in Appendix B.

This thesis proposes a new method of structure control which uses a flowing granular material as a passive vibration absorber. The method requires the attachment of a curved ramp (or track) on the structure to be controlled. On the track is a cylindrical container partially filled with a granular material. As the structure deflects under a dynamic load, the container rotates due to inertial resistance, causing the granular material to experience collisions. Tuning is achieved through ramp and cylinder radius selection, using a pendulum analogy. Absorber efficiency to dissipate harmful energy, can be tuned through granular material properties and the level of fill of its cylindrical container.

The second chapter is a study on the energy dissipation characteristics of granular materials flowing/sloshing in a rotating container. This chapter establishes that the flowing granular material is an efficient energy sink. The effectiveness of energy dissipation through granular flow is primarily determined experimentally. Then a computational model is developed to understand the flow behaviour and dissipation. A promising kinematic match of the particle flow behaviour is demonstrated between the numerical predictions and the experimental observations, and the suitability of the numerical model for predicting energy dissipation in a rotating container is proved.

The third chapter explores the limits to energy dissipation in a rotating granular flow environment. It is found that in this design, the energy dissipation due to particle collisions is proportional to the speed of rotation, up to the centrifuging speed when the dissipation nearly stops. Then steady speed experiments with numerical verification are used to study the accuracy of previous approximations of the centrifuging speed. Predictions are given of energy dissipation based on material properties. The numerical predictions are used to gain an insight into the nature of energy dissipation. Guidelines are offered for the choice of material properties to maximize the energy dissipation. The coefficient of friction between particles is found to have the greatest significance on the centrifuging speed.

The fourth chapter focuses on a scale model laboratory prototype of the suggested absorber. The structure to be controlled is represented by a cantilevered beam, with a circular ramp attached at the top. The absorber is a cylinder freely allowed to roll on the ramp and partially filled with sand. The effectiveness of tuning through matching of the pendulum frequency of the ramp to the natural frequency of the structure is explored. The absorber's peak effectiveness is found at fill levels of the container that are quite low, in the order of 1% to 2 %. The added mass of the container and sand is also in the order of 1%. The best performance of the absorber suggested more than two orders of magnitude improvement of the critical damping level of the structure.

The fifth chapter focuses on expanding the capabilities of the DEM numerical model. The development of a dynamic model is presented where there is 2-way communication between the granular material flow and the container dynamics. Comparisons are made with earlier work from Chapter 2, in which

rotation of the boundary is specified. The new numerical model predicts the behaviour of the granular material closely.

In Chapter six the conclusions of the thesis are summarised and possible future work is suggested. Additionally, in Appendix A, the experimental verification that a granular material in a rotating cylindrical drum is an effective energy sink is explored in more detail. Appendix B looks in more detail at tuned vibration absorbers and compares their method of operation to damped tuned vibrations absorbers and liquid sloshing dampers. This appendix is included for the completeness of the information.

2. Energy Dissipation Characteristics of Particle Sloshing in a Rotating Cylinder

2.1 Introduction

Observations of an exploratory study are presented in this chapter on the energy dissipation characteristics of particles sloshing in a cylindrical container. The objective is to take advantage of the desirable dissipation characteristics of particulate flow for control of excessive structural oscillations. Hence, the proposed configuration bears similarities to tuned vibration absorbers and liquid sloshing absorbers. Furthermore, comparisons to impact dampers which use granular or powdered material as an impact agent are made.

Tuned vibration absorbers are auxiliary systems attached onto some primary system to attenuate its dynamic response. Absorber parameters (spring stiffness and damping coefficient) are chosen so that the absorber intentionally resonates at an intended tuned frequency to provide the desired control effect for the primary system. The tuning frequency usually coincides with the critical frequency of the primary system. Although close to perfect suppression is possible at the tuning frequency, the control performance may deteriorate rapidly at other frequencies of operation. It is possible to extend the range of control frequencies by including dissipative components in the absorber design (Snowdon 1968).

The cost of such inclusion is, however, to lose control performance at the tuning frequency. More importantly, dissipative elements are high maintenance components by their nature. Hence, although a damped tuned

absorber is still a passive controller, inclusion of damping is not desirable from a practical point of view.

Liquid sloshing absorbers use intentionally induced sloshing to provide benefits similar to that of tuned vibration dampers for structural control. Sloshing refers to the low frequency oscillation of the free surface of a liquid in a partially filled container. Liquid sloshing absorbers are low maintenance components (Anderson et al. 2000), as they incorporate energy dissipation through free surface waves rather than mechanical dissipative components. They have found use in flexible structures such as towers (Tamura et al. 1996) and suspension bridges (Chen et al. 2008) under wind and earthquake loading. One of the challenges in the design of sloshing absorbers is to provide rapid energy dissipation which can be achieved with shallow liquid levels to promote travelling surface waves rather than standing waves. Using a granular material as the dissipation agent may overcome this difficulty and provide effective dissipation with simpler design configurations.

Use of a granular material as a control agent has been reported earlier in relation to impact dampers. Impact dampers are passive controllers that employ either single or multiple particles to provide the desired effect. Colliding elements are placed in a cavity which is attached to the primary system whose excessive oscillations are to be suppressed. The primary design effort is to determine the size of the gap around the impactor to tune the timing of impacts to oppose the oscillations of the primary system. Structural control is the result of energy dissipation through plastic collisions between the impact damper and its cavity, and the momentum opposition which results from disorganising natural phase relationships of the primary system – mostly applicable to harmonically excited cases (Papalou and Masri 1996). Enhancing energy dissipation for effective control of transient oscillations or

randomly excited cases may lead to significant impact forces and noise levels. Using multiple impact dampers and granular or powdered materials alleviates these problems to a large extent (Xu et al. 2005). The dissipative forces in such systems are a combination of plastic collisions, friction or shear damping (Panossian 1992, 1992).

Increased complexity of the ‘flow’ mechanics has mostly limited the efforts to experimental observations, with some preliminary recent advances (Wong et al 2009) towards performance prediction. When a granular material is contained in a cylindrical container and allowed to move freely as the cylinder rolls about its axis of symmetry, particles are able to tumble and collide with other particles and with the container boundaries. As a result, they dissipate energy in frictional interactions and in collisions. The focus of this chapter is to show that this system is an effective energy sink, and that the Discrete Element Method accurately describes the granular flow numerically.

The novelty of this research is the use of a rotating cylinder as a structural damper. A series of experiments are presented first which demonstrate that a cylindrical container partially filled with a granular material is a viable energy sink. Following the discussion of the experimental observations, a granular flow simulation using the numerical modelling technique Discrete Element Method (DEM) is described. The modelling is intended here to provide a kinematic comparison with the experimental data. The simulation results are directly compared against experiment, and the energy dissipation characteristics of the system are investigated in the context of the transient flow inside the rolling container.

2.2 Experimental Work

When a cylinder partially filled with grains (such as a vitamin pill container), is rolled on a surface, it rapidly dissipates its kinetic energy and comes to a complete stop. Hence, such a device may have significant potential as a viable energy sink for structural control applications. The objective of the experiments discussed in this section is to investigate the effects of important parameters on energy dissipation. In the following section, the experimental procedure is described briefly. Then a summary of observations from an extensive investigation is presented. Full details of these experiments are reported in (Dragomir et al. 2009) and attached as Appendix A.

2.2.1 Experimental Setup

Experiments were performed to quantify the relative effectiveness of certain design parameters. These involved allowing a cylindrical container partially filled with granular material to freely roll down an inclined ramp (from a known height) onto a flat surface. This setup is shown in Figure 2.1. The design parameters investigated here include the container size, fill level and the type of particles.

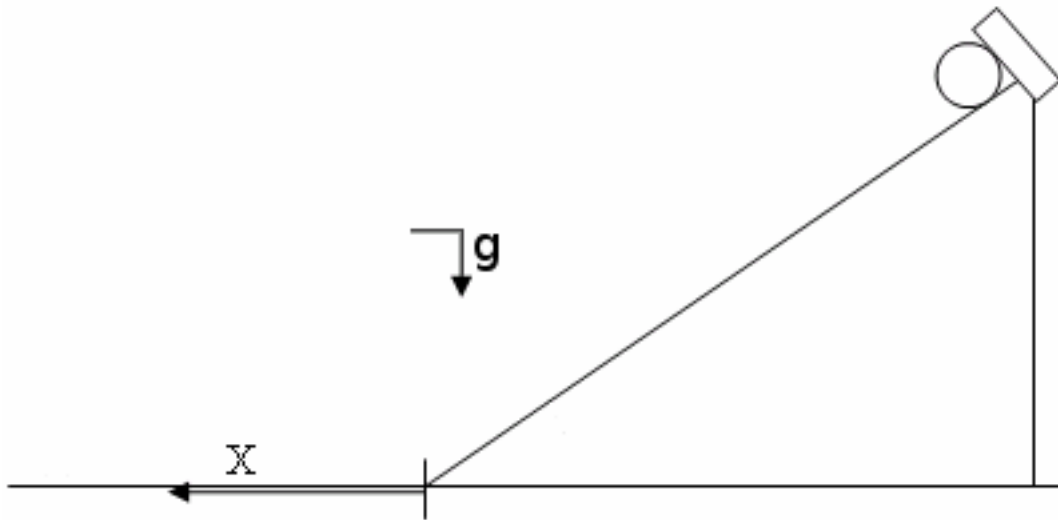


Figure 2.1: Schematic of experimental setup, showing stopping distance X along surface, ramp and bump-stop.

The container was released from a rest position at the top of the ramp. A bump stop was used as a fixed reference point to ensure that different cases started from the same height and thus with the same initial potential energy. As the container travelled down the ramp, it gained kinetic energy. Once the cylinder reached the bottom of the ramp, all of the initial potential energy was either dissipated or converted to kinetic energy. The rolling of the container continued some distance beyond this location, until all kinetic energy in the system was dissipated and the container came to a complete stop. The stopping distance X , is defined as the distance from the bottom of the ramp to the centre of the stopped container. This distance is used here as a simple measure of effectiveness of the granular damper. The flat section where stopping distance is measured is a glass surface to minimise rolling resistance. The dissipation of energy responsible for the halting of the cylinder is the result of collisions between particles and between particles and the enclosure walls.

Relevant parameters of the experiments to determine the effect of different container sizes are given in Table 2.1. In addition, four different particle types were tested. A photograph of these particles is shown in Figure 2.2. Table 2.2 includes the important parameters.

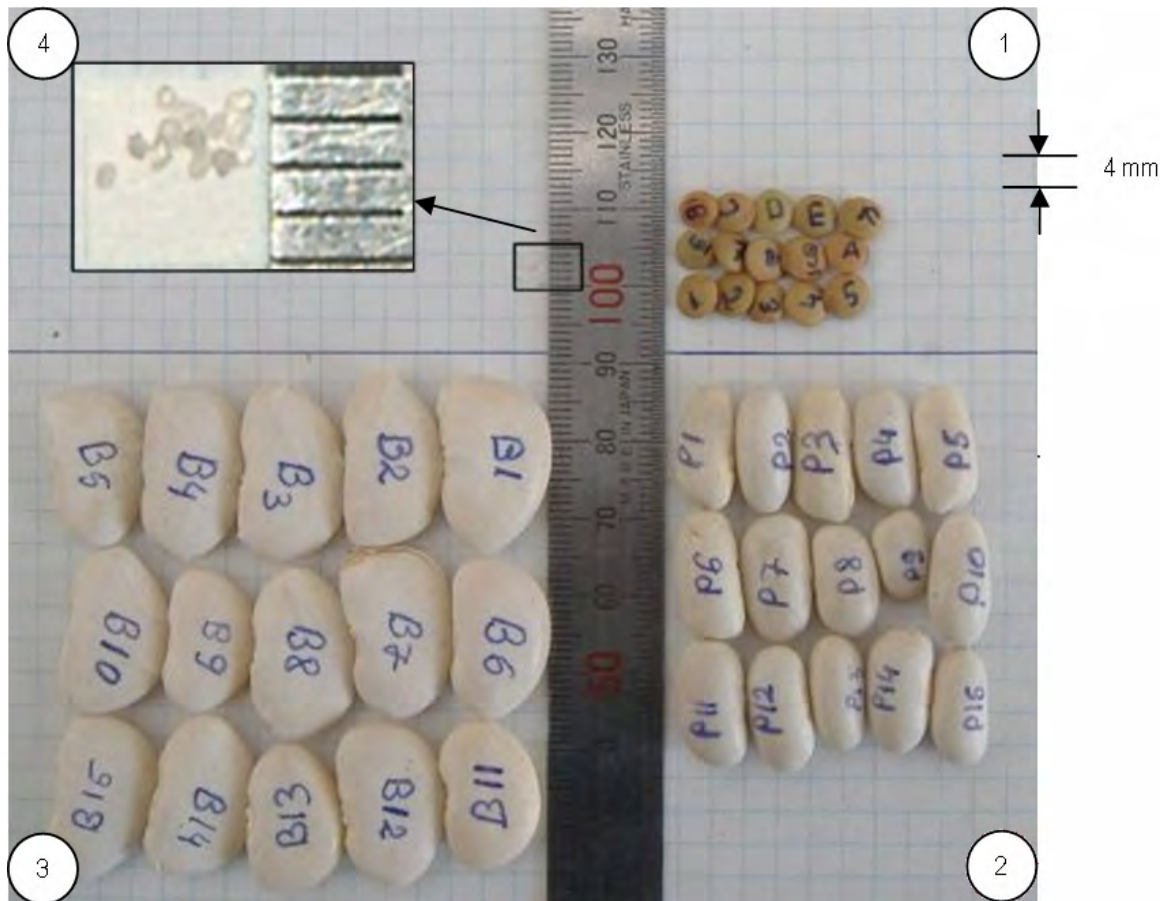


Figure 2.2: Depiction of 15 particles of each type. (1) lentils; (2) soy beans; (3) broad beans; (4) sand. The inset represents a close-up of Particle 4.

Table 2.1: Container properties.

Container	Volume (l)	Height (mm)	Diameter (mm)	Mass (g)
1	1.1	95	130	50
2	0.5	100	60	20
3	0.625	170	65	27

Table 2.2: Particle properties given as ranges and averages of 16 particles. Values for Particle 4, sand, are approximations based on high resolution pictures of the particles used. All other particle measurements have error margins of ± 0.5 mm.

Particle	Freely Settled Bulk Density (kg/m^3)	Height	Width	Length
		(Average) (mm)		
1 (lentil)	0.8	2 – 3.5 (2.7)	5 – 6 (5.6)	5 – 6 (5.6)
2 (soy bean)	0.8	4.5 – 6.5 (6)	7.5 – 9 (8.2)	12 – 17 (16)
3 (broad bean)	0.8	5.5 – 7.6 (6.4)	12 – 15 (13.6)	18 – 23 (22.5)
4 (sand)	1.7	0.3 – 0.5 (0.4)	0.3 – 0.6 (0.4)	0.3 – 0.6 (0.4)

One observation made during the 1st series of experiments was that some sliding occurred at the contact between the container and the inclined ramp surface, in addition to the more prominent rolling motion. Sliding was observed to be more significant for higher fill levels (greater than about 35% - 40%). This observation led to a 2nd series of experiments in which rolling and sliding motion of the container were isolated. These experiments with almost perfect rolling motion were shown to dissipate significantly more energy than the experiments that permitted sliding motion (Dragomir et al. 2009). Hence for the 2nd series of experiments, the ramp was fitted with a hard neoprene sheet to enforce a no-slip motion for the container.

2.2.2 Experimental Observations

2.2.2.1 General Motion

In Figure 2.3, observations are presented which demonstrate the effect of different container dimensions on the stopping distance X . A 35-degree ramp with the container released from an elevation of 0.2 m and Particle 2 (soy beans) were used for these experiments.

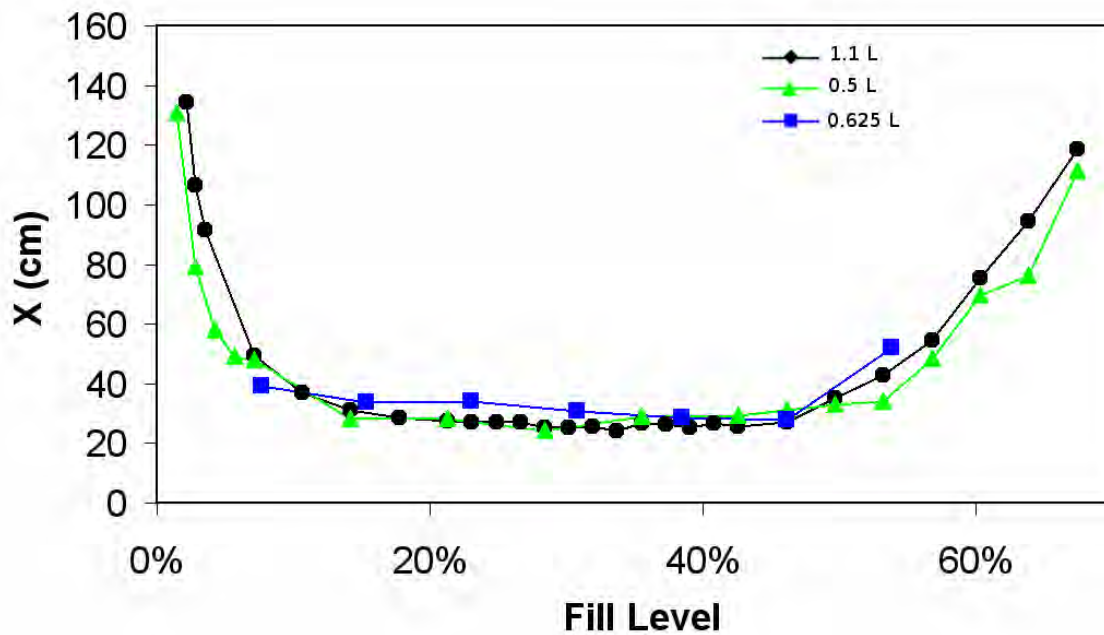


Figure 2.3: Variation of the stopping distance, X , with fill level for containers 1 (1.1L), 2 (0.5L) and 3 (0.625L). All experiments use Ramp 1, Particle 2 on glass surface.

The stopping distance decreases rapidly with increasing fill level, up to about 15% fill. From 15% to about 50%, stopping distance appears largely insensitive to fill level. For fill levels above 50%, the system becomes increasingly less efficient at dissipating the container's kinetic energy up to the point where the container is completely full. It is worth mentioning that the rate of energy dissipation (increase in stopping distance) with fill level, after 50%, is approximately 3-4 times less sensitive than the rate of decrease in stopping distance, up to 15%. The most significant observation from Figure 2.3 is that the dissipation characteristics depend solely on the fill level and that they are completely insensitive to container size over the small range considered here.

In Figure 2.4, the stopping distance for different particle sizes and shapes are compared using the first 3 particle types from Table 2.2 (since they all have

similar mass densities and contact surface properties). The ramp and contact surface are the same as for the previous figure. Stopping distances for all three particle types were similar, but the smallest, Particle 1 (lentils) seems marginally more effective for fill levels up to 50%. On the other hand, at 50% fill, the opposite trend occurs. Lentils have approximately twice the stopping distance of the other particle types. The primary difference between Particle 1 (lentils) and 2 (soy beans) and 3 (broad beans) is its smaller size. Lentils also have an approximate disk-shape as opposed to the bean-shape of the others.

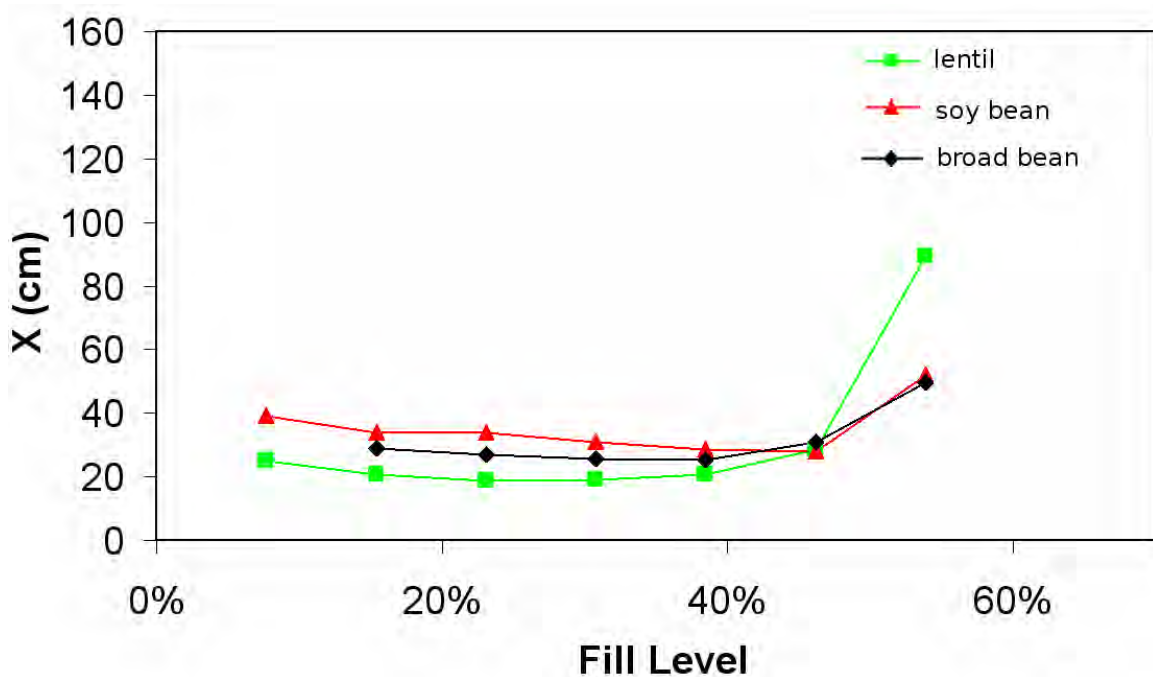


Figure 2.4: Effect of particle size and shape 1 (lentil), 2 (soy bean) and 3 (broad bean). All experiments with Ramp 1 and Container 3 on glass surface.

2.2.2.2 Roll without slip

Results of the 2nd series of experiments, involving almost perfect rolling motion of the container, are presented here. In Figure 2.5, the performance of Particles 1 (lentils), 2 (soy beans) and 4 (sand) are compared for different fill

levels, using Container 2 and with (almost perfect) rolling motion as outlined in the experimental setup. Significant material differences exist between the different particle types, as summarised in Table 2.2. For example, Particle 4 (sand) possesses the highest surface friction due to its random distribution of size, rough contact surface and blocky shape. Also, sand has a mass density more than twice that of lentils and soy beans, and smaller dimensions by at least an order of magnitude.

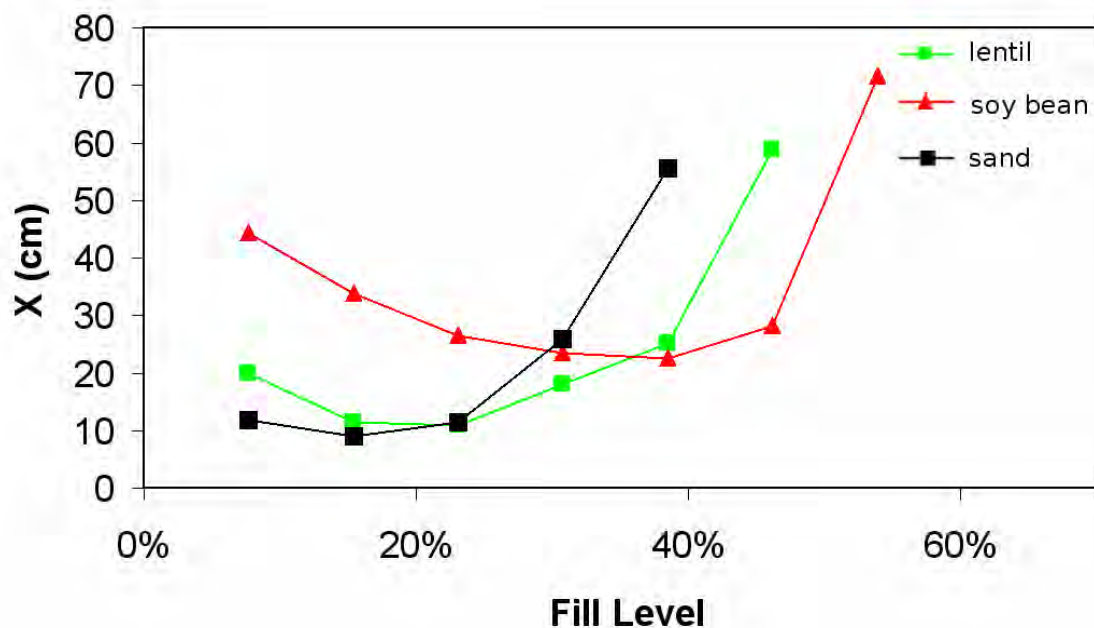


Figure 2.5: Comparison between Particles 1 (lentil); 2(soy bean) and 4(sand) for (almost perfect) roll.

The smaller and denser sand (Particle 4) is clearly a better energy dissipater at low fill levels, up to about 25%. However for higher fill levels, lentils (Particle 1) and soy beans (Particle 2) have lower stopping distances. All three curves in Figure 2.5 have a similar overall shape, but are either displaced or stretched along the horizontal axis. Since the bulk density of sand is significantly larger than that of the other two particles, it has significantly larger initial potential energy when released from the same elevation. Therefore simply comparing

fill level alone is not sufficient for a proper comparison of energy dissipation properties of different materials.

In Figure 2.6, the stopping distance is plotted against initial potential energy for the same experiments reported in Figure 2.5. Smaller and disk-shaped lentil particles appear to be more effective at dissipating energy than soy bean particles. Sand, however, has a notably different distribution of stopping distances for different incident energy. It demonstrates the same best performance as that of lentil particles, of 10 cm stopping distance, at about 0.25 J of initial potential energy. However, unlike lentils, sand is able to maintain this peak performance over a much wider range of initial potential energies (up to 0.60 J). Hence, among the particles tested, sand is the most effective dissipater.

In summary, experimental observations clearly demonstrate that the particle flow in a rotating cylindrical container has promising potential as an energy sink for structural control applications. When the mass density of the particles is comparable, fill level in the container appears to be a meaningful dimensionless ratio for performance, even when significant differences exist in size and shape (lentils, soy and broad beans). However, not surprisingly, fill level is less significant when bulk density and friction parameters change. Such a trend emphasises the importance for inertial and dissipative parameters to be included in more universally applicable groups of non-dimensional parameters. Sand was found to be the most effective dissipative material when filling 15% to 20% of the container.

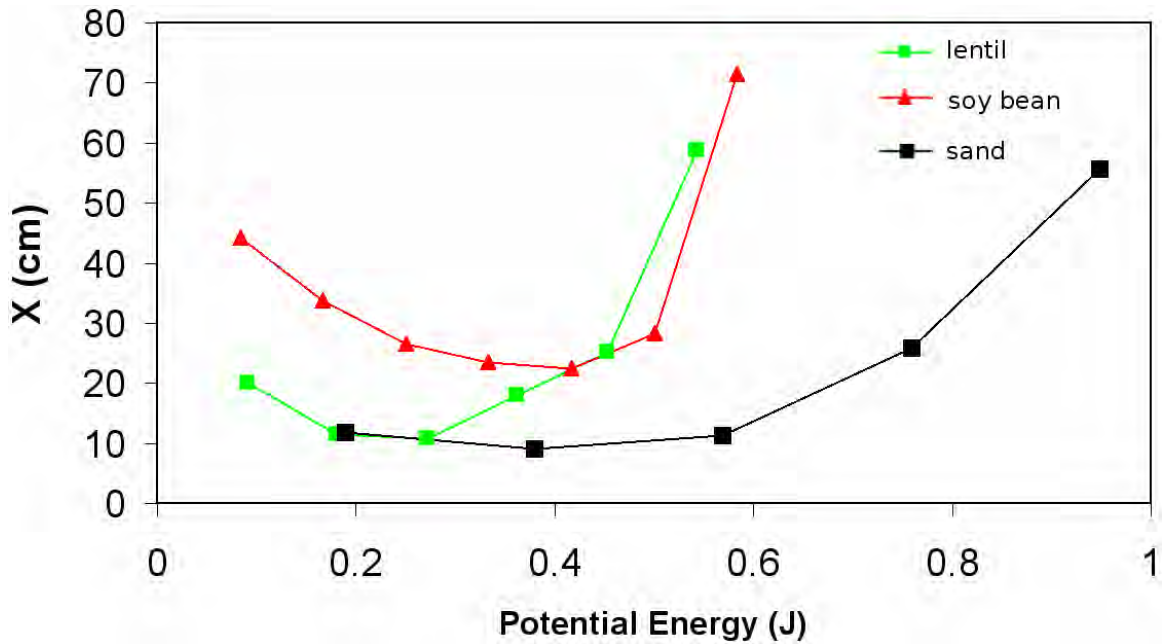


Figure 2.6: Comparison between Particles 1 (lentil); 2(soy bean) and 4(sand) for potential energy.

2.3 Numerical Model

Particle-based numerical models are well suited to model granular flows since they are able to represent each individual contact interaction. The Discrete Element Method (DEM) is a particle-based method which tracks the motion of individual particles and it has been reviewed by (Campbell, 2006), (Barker, 1994) and (Walton, 1992). A DEM granular solver developed by the Commonwealth Scientific and Industrial Research Organisation (CSIRO) is used here. The CSIRO solver has been successfully applied to a wide range of applications from mining to pharmaceuticals (Cleary, 1998, 2001, 2008), (Sinnott et al. 2006). A brief description of the method is given next, for completeness. Then, numerical predictions are discussed.

2.3.1 Discrete Element Method

The DEM solver uses a linear spring-dashpot contact model as shown in Figure 2.7 and described in more detail by (Sinnott et al. 2006). Particles in contact are represented by spherical surfaces on the left and right. The contact forces are represented by linear springs and dashpots in the normal and tangential directions.

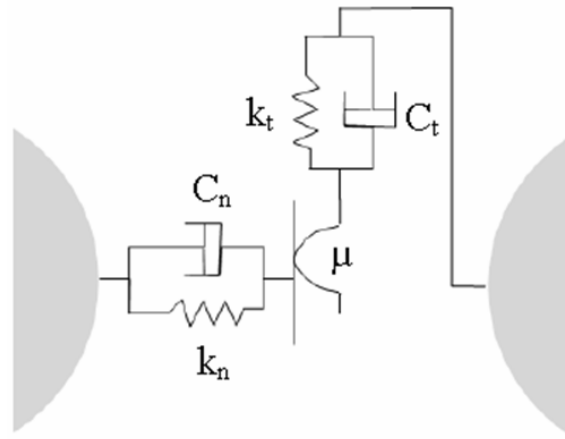


Figure 2.7: Normal and tangential elastic and dissipative elements used to evaluate contact forces.

In the normal direction to the contact, the force F_n is

$$F_n = -k_n \Delta x + C_n v_n \quad (2.1)$$

where k_n and C_n are the contact stiffness and damping coefficients respectively, Δx is the amount of overlap, and v_n is the normal speed. The first term represents the resistance to deformation (the restoring force), whereas the second term is the equivalent viscous damping force, proportional to the normal speed. The spring is a purely repulsive force, to avoid non-physical attractive forces. The amount of overlap is determined by k_n . The desired

average overlap is between 0.1% and 1.0% of the particle size (Cleary et al. 2003). The damping coefficient C_n is dictated by the coefficient of restitution.

In the tangential direction, the contact force F_t is

$$F_t = \min \left[\mu F_n, (k_t \int v_t dt + C_t v_t) \right] \quad (2.2)$$

where μ is the friction coefficient, k_t and C_t are stiffness and damping coefficients respectively, and v_t is the speed in the tangential (shear) direction. The integral term represents the elastic forces due to deformation in the tangential direction. The total force is limited by the Coulomb force (μF_n). When it is reached, sliding of the contact surfaces begins. The boundary of any object interacting with particles can be represented as a triangular mesh. Particles can overlap individual mesh element surfaces and define normal and tangential contact forces using the same linear spring-dashpot model as in Equations (2.1) and (2.2). The friction, stiffness and damping coefficients in Eq. (2.1) and (2.2) came from the normal and tangential coefficients of friction and restitutions between particles and particles and container wall.

Super-quadric shapes are used to model the particles as opposed to more commonly used spheres, as spheres cannot predict the shear resistance and dilation of particle beds accurately (Cleary 2008), (Cleary and Sinnott 2008). The most general form of super-quadrics is (Cleary 2008):

$$\left(\frac{x}{a}\right)^n + \left(\frac{y}{b}\right)^n + \left(\frac{z}{c}\right)^n = 1 \quad (2.3)$$

The fractions b/a and c/a are the aspect ratios in the xy and xz directions respectively. For $a = b = c$ and $n = 2$, the resulting particle is a sphere. As n

increases, the particle shape approaches that of a cube with progressively sharper corners, as shown in Figure 2.8.

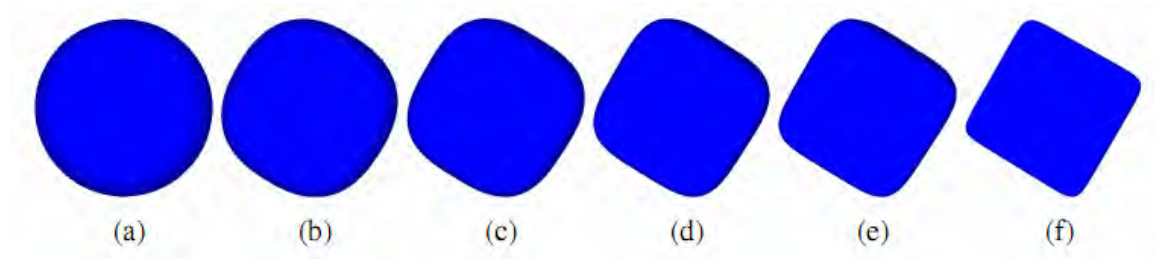


Figure 2.8: Super-quadric shapes for (a) $n = 2$, (b) $n = 2.5$, (c) $n = 3.0$, (d) $n = 4.0$, (e) $n = 5.0$, and (f) $n = 10$.

The typical DEM algorithm tracks all particles and collisions within the system being modelled and collects the resulting forces on the particles and on the boundaries, so as to sufficiently resolve the contact dynamics. Several statistics relevant to energy dissipation are recorded for the purposes of investigating flow related mechanisms responsible for dissipation in the rolling container.

The particles used have size and shape parameters which represent sand as used in the experiments. The particles are super-quadrics with blockiness parameter n randomly distributed with a uniform probability between 2.5 and 5.0. The super-quadric major axis length is distributed between 0.8 and 1.6 mm, and the super-quadric aspect ratios b/a and c/a between 0.8 and 1.0. The bulk material density is 1600 kg/m^3 . The spring stiffness $k = 600 \text{ N/m}$ was chosen to give average particle overlaps less than 0.5% of the particle radius which is reasonable for the DEM method. The coefficient of restitution e was chosen as 0.75, and the coefficient of friction μ as 0.70. The container object is a cylinder with inner radius of 37.5 mm and length of 200 mm. The 20% fill level simulation presented in this chapter, has 50105 particles.

The objective for the simulation presented here is to study the particle motion where the kinematics of the cylinder object are fully specified container velocities directly measured in the experiment. The motion of the container is characterised from a high-speed video of the container. The derived horizontal and vertical velocities, and the spin of the container are then specified at 20 ms intervals for the simulation.

A side-by-side comparison of the container locations during the simulation (above) and experiment (below) are given in Figure 2.9. The images are shown with 160 ms intervals until the motion ceases at 900 ms after the instant of release. Particles are coloured by their speed, with blue representing 0 m/s and red 1.5 m/s.

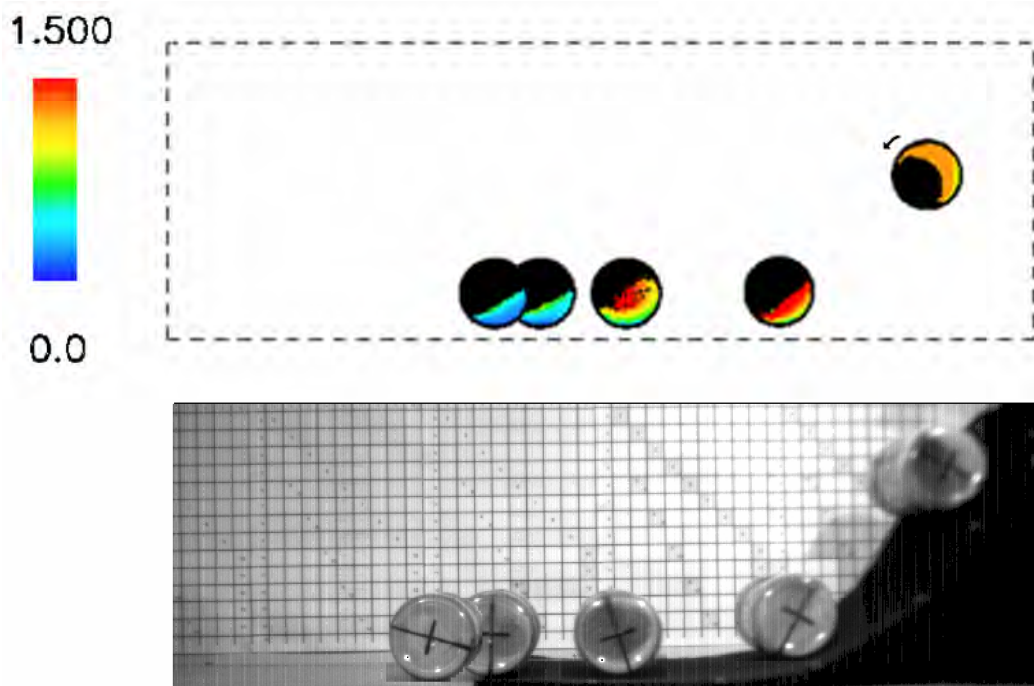
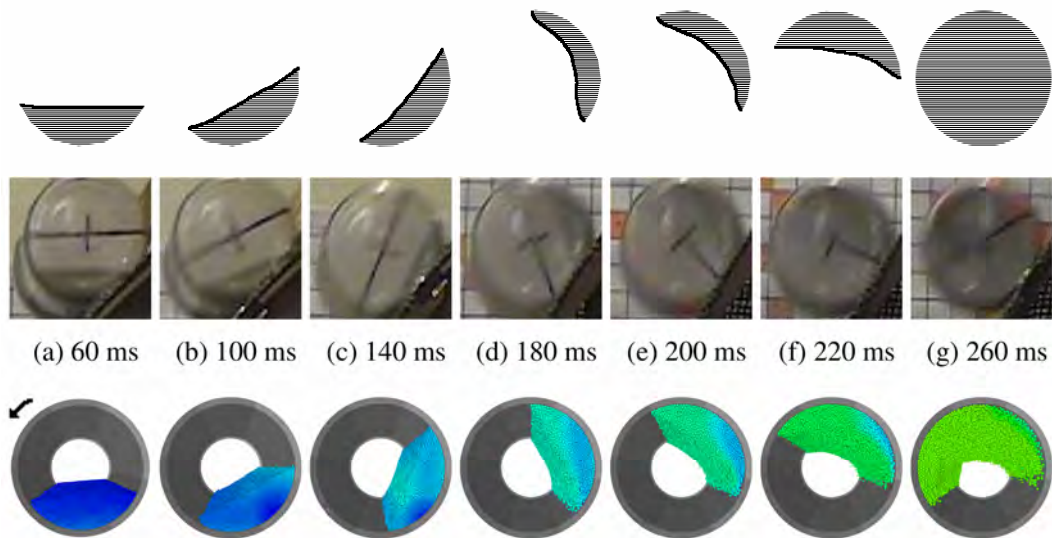


Figure 2.9: Sample container locations for the simulation (above) and experiment (below) at 160-ms intervals. Simulation particles coloured by speed from stationary (blue) to 1.5 m/s (red).

2.3.2 Numerical Predictions

In Figure 2.10, close-up views of the container are presented to show the details of the granular flow field. The images are presented at different times, to highlight specific flow events related to the particle and container motion. Numerical and experimental images are shown in conjunction with schematic illustrations of the particle distribution in the container. Schematic illustrations are in the first row of each group, experiments given in the second rows, and the numerical predictions in the third rows. For the simulation data, a long axis view of the container is given from the front wall where the white circular area in the centre of the container represents the back wall.



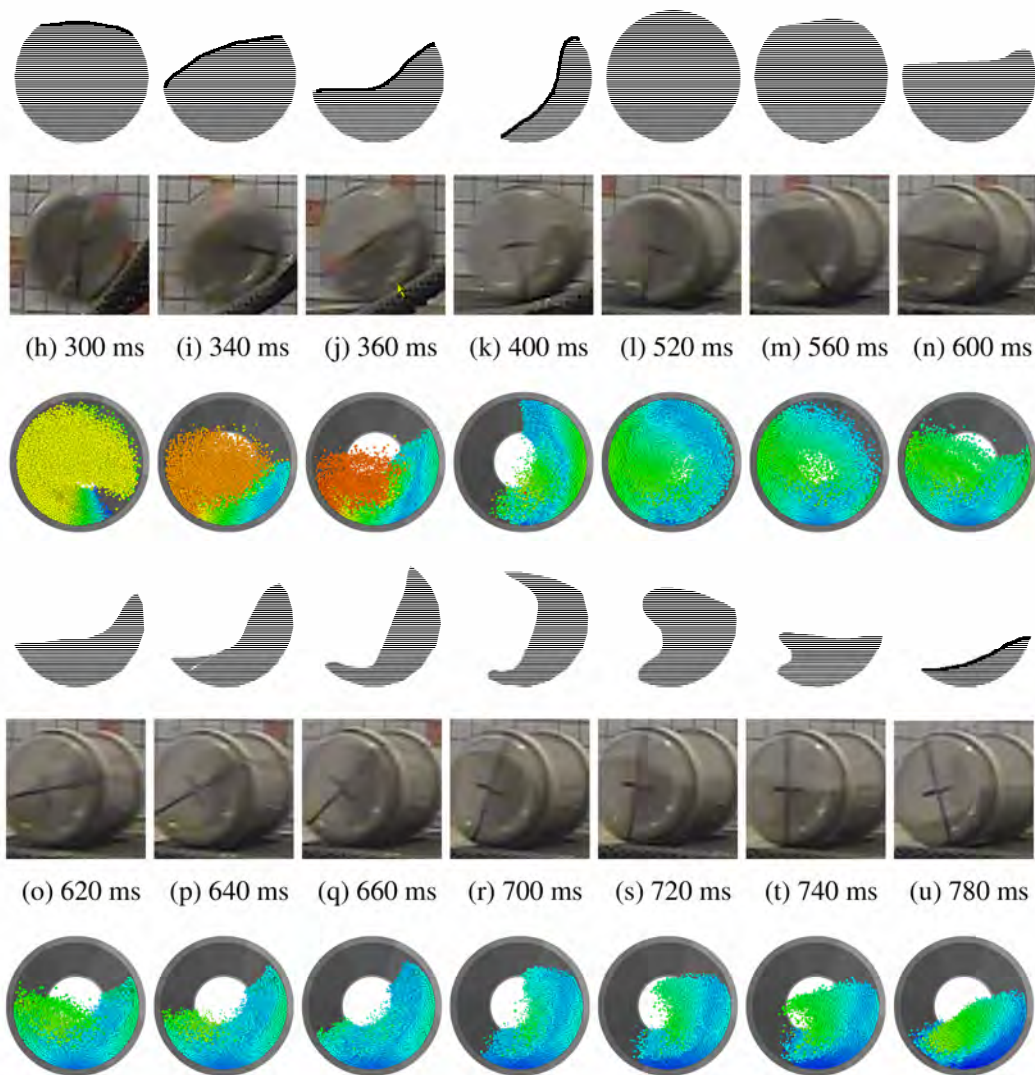


Figure 2.10: Comparison of experimental and numerically predicted surface shapes. The first row of each group is a schematic illustration of the photographs from the experiment shown in the second row. The third row contains the corresponding DEM predictions. The same results are coloured using the same scale as in Figure 2.9.

Three significant flow events are observed. Firstly, two centrifuging events occur where the particles can be seen lining the container wall and which then collapse under gravity. A third event is observed as a cataracting stream where some particles become airborne but have insufficient energy to centrifuge. The particles then come to rest soon after the container reaches the horizontal plane. These three events are discussed next in more detail.

For the first 200 ms, particles move as a solid body. From 200 to 300 ms, the particles centrifuge and line the container walls as it accelerates down the ramp as seen in Figure 2.10 (f-h). Particles near the top of the container collapse under gravity falling to the bottom of the container between 300 and 360 ms as shown in Figure 2.10 (h-j). The experiment and simulation show nearly identical particle motions for the frames. In the simulation, at 300 ms the majority of the particles have a speed of 1.2 m/s. By 340 ms, the remaining airborne particles have increased their speed to 1.4 m/s, while those in contact with the wall average 0.7 m/s.

The particles centrifuge for the second time between 520 and 600 ms just as the container reaches the flat surface. Matching particle bed surface shape in the container for the numerical and experimental observations can be observed between 600 and 620 ms, in Figure 2.10 (n-o). Particle speeds are slower than the previous centrifuge, with average speeds being only 0.8 m/s for both the container wall and the airborne particles.

From 700 ms, Figure 2.10 (r-w), a single cataracting stream is observed in both the experiment and the simulation. The airborne particles approach 0.7 m/s, while the container wall particles travel at 0.2 m/s for this event. Particle motion ceases completely at 900 ms.

For all three events discussed, free surface shapes from experimental observations and numerical predictions match closely. With this confidence in the flow predictions from the DEM simulations the dissipation mechanisms in this system are discussed next.

The total, instantaneous dissipation power plotted against time is shown in Figure 2.11. The three events discussed in relation to Figure 2.10 earlier, are marked in this figure.

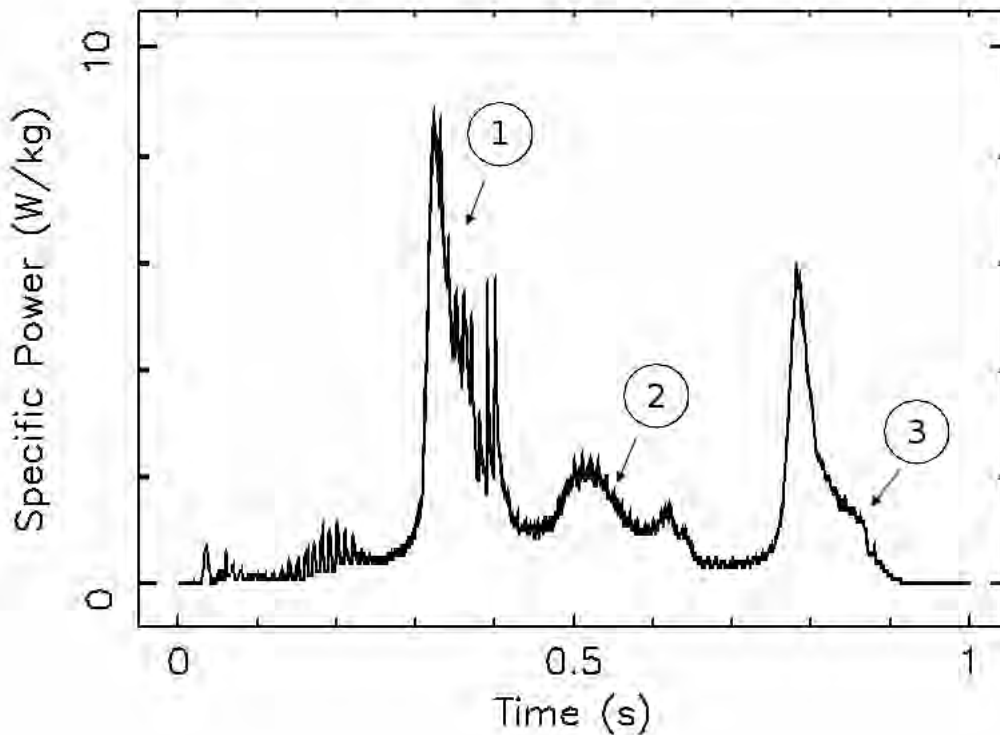


Figure 2.11: History of instantaneous energy dissipation.

The first event is centred around the first centrifuging event particle collapse, with peak dissipation at 340 ms (see Figure 2.10 (i)). The second event is much smaller in magnitude and peaks at 540 ms (see Figure 2.10 (l-m)). The third event occurs after the cataracting stream collides with the container wall, at 790 ms (see Figure 2.10 (u)).

Each collision can be disaggregated into forces. The normal component for the dissipation is due to the dashpot (viscous damping force) $C_n V_n$. The tangential dissipation component $C_t V_t$ is responsible for frictional losses. The

energy dissipated in these dashpots defines the instantaneous dissipation power, shown in Figure 2.11. The normal and tangential components of energy dissipation are shown in Figure 2.12. Four snapshots are shown between 340 ms and 400 ms, which indicate the localised energy dissipation. The particles are coloured according to the sliding scale shown on the right. The scale for the tangential dissipation is twice that for the normal dissipation.

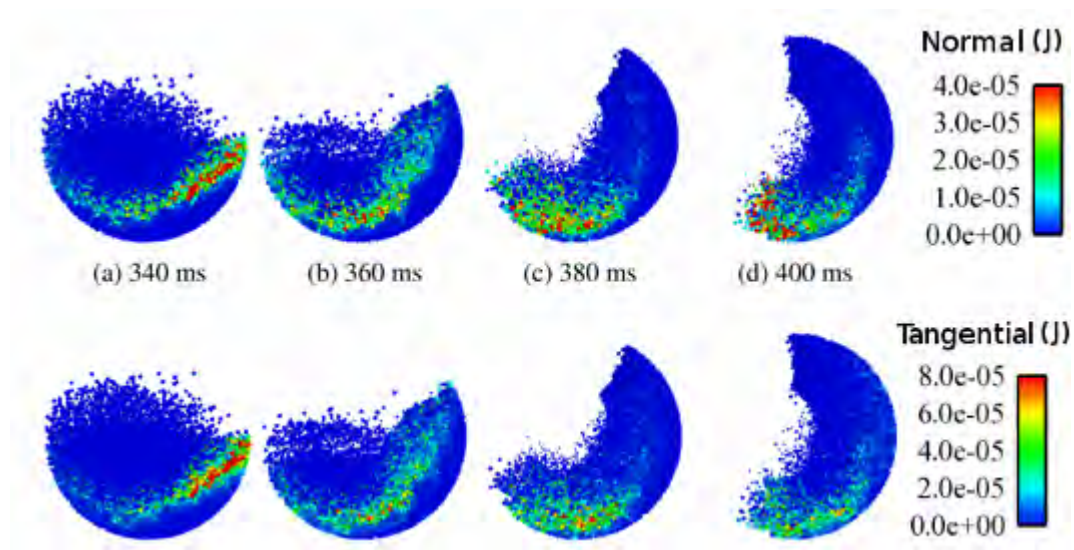


Figure 2.12: Energy dissipation for the first event in Figure 2.11. Top row is for the normal direction, and the bottom row for the tangential direction.

The first large peak around 340 ms in Figure 2.11 corresponds to the collapse of particles after centrifuging. As a result, the top layer of the particle bed experiences collisions at large speeds with airborne particles. Significant amounts of energy are also dissipated through shear in the centre of the particle bed as shown in Figures 2.12 (a) and 2.12 (b).

The energy dissipation during the second centrifuge and collapse of the particles between 500 ms and 600 ms, is given in Figure 2.13 in the same format as Figure 2.12. While there are many airborne particles, only a small number of the total particles are involved in high dissipative losses. Also

airborne particle speeds are slower than the first centrifuge/collapse, thus both total and peak energy dissipation is rather poor.

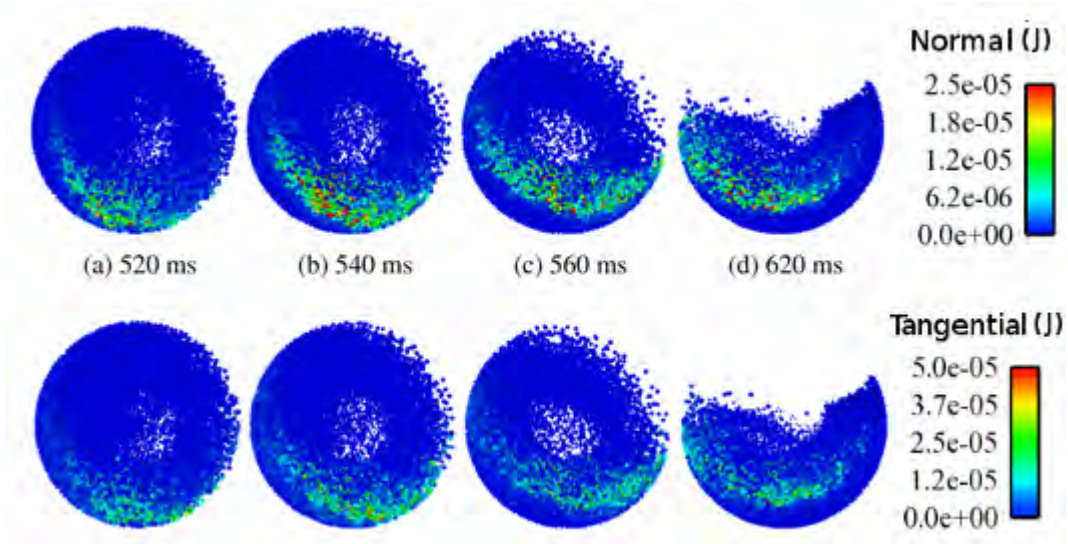


Figure 2.13: Energy dissipation for the second event in Figure 2.11.

Particles coloured by normal and tangential energy dissipation rate for the third event are shown in Figure 2.14, the cataracting stream of particles between 760 and 820 ms. Although the absolute speeds of the cataracting particles are relatively small, 0.1 m/s, there are steep velocity gradients which cause significant shear at the trailing end (far left end) of the bed. It is also noticeable that there is a considerable normal dissipation avalanching surface layer impacting at the wall. It is worth noting that while the airborne speeds of the cataracting particles in event 3 are much smaller than those in event 1, comparable levels of energy dissipation are observed in Figure 2.12. This suggests that shear dissipation from the avalanching surface layer (rather than impacts from cataracting particles) is the dominant energy loss mechanism controlling the stopping distance of the container. Maintaining a steady

avalanching regime through around the same trailing end of the bed due to the cataracting particle stream and the control of the container's angular speed could conceivably provide a controlled level of shear dissipation which would be a desirable property for a granular absorber.

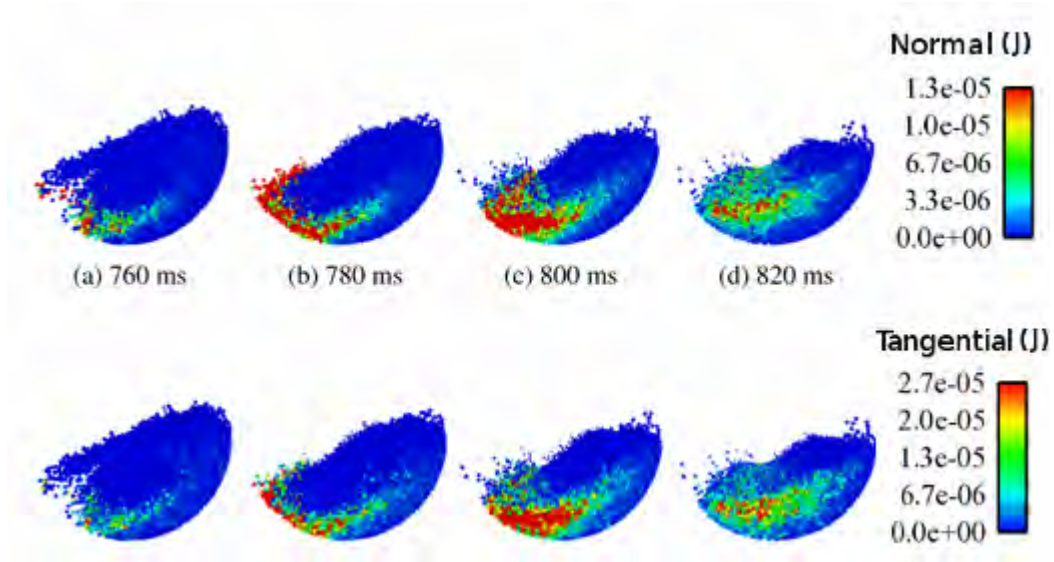


Figure 2.14: Energy dissipation for the third event in Figure 2.11.

In summary, the numerical predictions obtained with the DEM solver closely match the experimentally observed particle motion. Hence, further analysis of the numerical simulations can be used to draw more in-depth conclusions on the nature of the energy dissipation. Such details are not possible to obtain from the experiments alone.

2.4 Conclusions

Observations are reported in this chapter to investigate the energy dissipation through particle flow in a rotating container. The objective is to incorporate such a design as an effective energy sink in a vibration absorber similar to sloshing absorbers.

The first part of this chapter presented a summary of an extensive experimental study to demonstrate that a cylindrical container partially filled with a granular material is a viable energy sink. Fill level is shown to be an important parameter which affects the flow pattern and, as a result, energy dissipation. In addition, some sensitivity to particle type was also observed where the smallest and densest particle (sand) are identified as the best dissipater.

A numerical prediction model of the particle flow in a rotating drum was also presented. Kinematic comparisons of the particle flow between the simulation and the experiment show a close match, when the container motion is imposed using data from the experiment.

The particle flow consisted of three distinct events, which also characterised the energy dissipation of the system. These events are the collapse of a centrifuging particle stream twice, when the system has significant energy and a cataracting stream prior to the system coming to rest.

Two energy dissipation mechanisms were found with the help of numerical simulations: the collisions at the particle bed during the cataracting stream collapse, and shear layers when the particles flow in an avalanching regime. Shear through tangential components of collisions was found to be the primary energy dissipation method, accounting for two thirds of the total.

The idea of using a rolling container partially filled with granular material as a tuned vibration absorber is certainly a viable one. Such an absorber inherently possesses effective energy dissipation. Further study to model particle flow numerically and implement the absorber to structural applications is currently underway.

3 Critical speed and energy dissipation in a rotating cylinder

3.1 Introduction

Tall structures are flexible under dynamic loads such as those from wind and earthquake. For safety and comfort purposes, they often require a damping mechanism to dissipate the excess harmful oscillatory energy.

Traditionally, Tuned Mass Dampers (TMD) are used in structures such as the Taipei 101 Tower (Bekdas et al. 2011). These devices usually have a range of frequencies where they are effective, at and around the natural frequency of the structure, usually below 1 Hz. More recently, Liquid Sloshing Absorbers (LSA) have been introduced, for example in the Comcast Centre, Philadelphia (Fiscoa et al. 2011), as a low maintenance alternative. Liquid Sloshing Absorbers have a smaller mass ratio, and they can be set-up to respond to a larger range of frequencies than TMDs. Another alternative to TMDs uses granular materials either enclosed in (Papalou and Masri, 1996), or attached near the top of the structure (Fischer, 2007). Earlier research of the authors has shown numerically and experimentally that a granular material in a rotating container can be an effective dissipation method (Dragomir et al. 2007, 2010, 2010).

A rotating absorber with granular flow moves in a circular track attached to an existing structure to be controlled. The cylindrical container rotates on the track due to inertial and gravitational forces. The granular material inside the container experiences collisions and shear, and consequently, it dissipates the harmful energy from the structure. A schematic representation of such a setup

is shown in Figure 3.1 where the structure is represented with mass (m), stiffness (k) and damping coefficient (c) of a simple oscillator. The objective for such a configuration is to dissipate the energy rapidly in order to avoid damage to the structure.

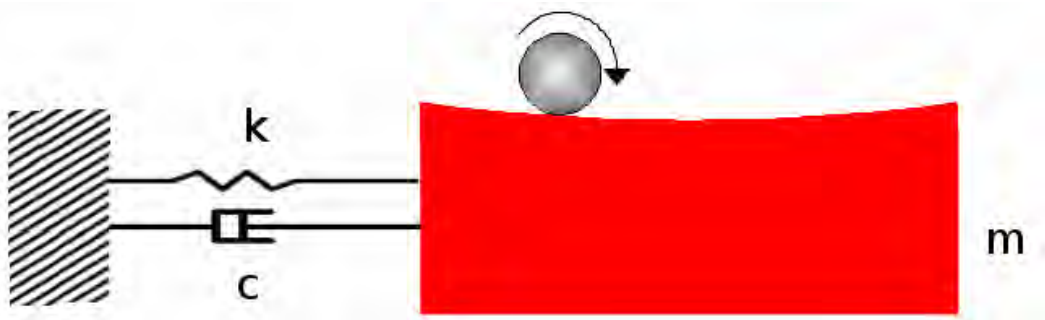


Figure 3.1: Schematic representation of the suggested rotating absorber with granular flow.

Simulations using the Discrete Element Method have suggested that energy dissipation increases with the speed of rotation, before the granular material centrifuges, and then, the energy dissipation stops. The energy dissipation at the centrifuging speed is significantly smaller than the energy dissipation at a speed just prior to centrifuging. As such, it is critical that the centrifuging point is accurately determined as it shows peak dissipation for the absorber, while overestimating it prevents the absorber from functioning correctly.

Rose has been the first to show experimentally that the critical centrifuging speed can be approximated as (Rose et al. 1958)

$$N_c = \sqrt{\frac{g}{R}} \quad (3.1)$$

where g is the gravitational constant and R is the radius of the container. This is the standard pendulum analogy where the gravity force is balanced by the

centrifugal force due to angular motion. Any observed increase in the boundary speed past $(g/R)^{1/2}$ where centrifuging has not yet occurred is attributed to boundary slip. For single particle systems, Rose found the critical speed to be $[2g/(D-2R)]^{1/2}$ where D is particle diameter, accounting for particle size. (Rose et al. 1958)

A recent study by Ottino sets the critical speed as $(g/L)^{1/2}$, where L is a container-derived characteristic length (Ottino et al. 2000). For the 50% fill level, L is equal to the cylinder radius, while for all other cases $L < R$. This indicates that the Froude number $Fr = (\omega^2 R)/g \approx 1$, ω increases as the fill level decreases, where ω is the angular speed. $Fr = 1$ when the centripetal acceleration matches the gravitational acceleration of the rotating cylinder of radius R . However, this formulation does not account for the effect of any of the material properties on centrifuging speed, such as the coefficient of friction, which has been observed by the authors to be important.

A more recent study (Watanabe 1999) improves on results by (Ristow et al. 1997), (Ristow 1998) and (Walton et al. 1993) to include fill level and material properties in the form of angle of repose (θ) and the fractional fill level (α) in a cylindrical container:

$$N_c = \frac{1}{2\pi} \sqrt{\frac{g}{R \sin \theta \sqrt{1-\alpha}}} \quad (3.2)$$

where R is cylinder radius and N_c is the critical speed in Hz.

Watanabe's expression for N_c takes into account both material properties and fill level, and it is the most complete characterization found in the literature. This expression implies that low fill levels and low angles of repose lead to higher centrifuging speeds, which is desirable for an efficient design.

The implication in this approach is that the coefficient of restitution and the mass density of the particles do not contribute to N_c , whereas the friction coefficient is accounted implicitly through the angle of repose. This assertion is verified through a parametric study in this paper and the additional importance of the material density to energy dissipation is found.

The majority of the existing research concludes that $(g/R)^{1/2}$ is a sufficient approximation for the determination of the speed of centrifuging for a partially filled rotating container. While refinements exist, they are not widely acknowledged or used. Since, for the purpose of energy dissipation, centrifuging speed is critical, the existing body of work needs to be examined critically. Hence, this work focuses on experimentally and numerically identifying the centrifuging speed for a partially filled container. The objective is to identify the mechanisms of energy dissipation and then to investigate material properties which maximize the energy dissipation.

In the following section, the experiments are described. In Section 3.3 the numerical model and method of simulations are described in detail. In Section 3.4, a comparison of the numerical model predictions is given which shows that the experimental and numerical results are in close agreement. Subsequently, the numerical predictions are analyzed further to show what the significant mechanism of energy dissipation is, and where the dissipation occurs within the granular material. Finally, a parametric study is presented to investigate the relative importance of material properties to delay the onset of centrifuging and yield the most efficient design.

3.2 Experiments

An experiment is designed to check the validity of the numerical tool to accurately predict the centrifuging speed for a partially filled container with a granular material. This validation is required as experimental work alone would not give the level of detail possible numerically, for determining the mechanism of the energy dissipation in the container.

The experiment is designed to determine the speed of centrifuging in a glass container. The experimental observations for different fill levels are then compared to numerical observations. Fill level is defined as the percentage of the particle volume as part of the container volume.

The experimental setup consists of a glass cylinder with a diameter of 75 mm and length of 140 mm. The cylinder is fixed through a bearing at either end. This system allows the viewing of the system from any angle with minimal obstruction. The cylinder is rotated by an electric motor through a belt system. The motor's output is regulated by means of a variable voltage power supply. Cross markings on the container's end wall are used to determine the speed of rotation from the video recordings of the experiment. A light source placed at the side is used to clarify the image of the particles. The experimental setup is shown in Figure 3.2.

The granular material used in the experiment is medium sand. Its average size is about 0.6 mm, with a particle density of 2645 kg/m³ and a dry bulk density of 1600 kg/m³. Experiments were conducted for three fill levels of the cylinder: 15%, 22% and 28%, by volume.

Experimental procedure consists of the following steps. The electric motor speed is set using the power supply. A variable resistor connected in series provides fine control over the voltage drop and the motor's speed. The motor's speed is slowly increased over a period of time. Once the material inside the container centrifuges the experiment is stopped. Video recordings of the experiment are examined to determine the average speed at which the material centrifuges. Average speed is defined as the average within 0.5 seconds (25 frames) prior to the material centrifuging and 0.5 seconds after the frame where centrifuging first occurs.

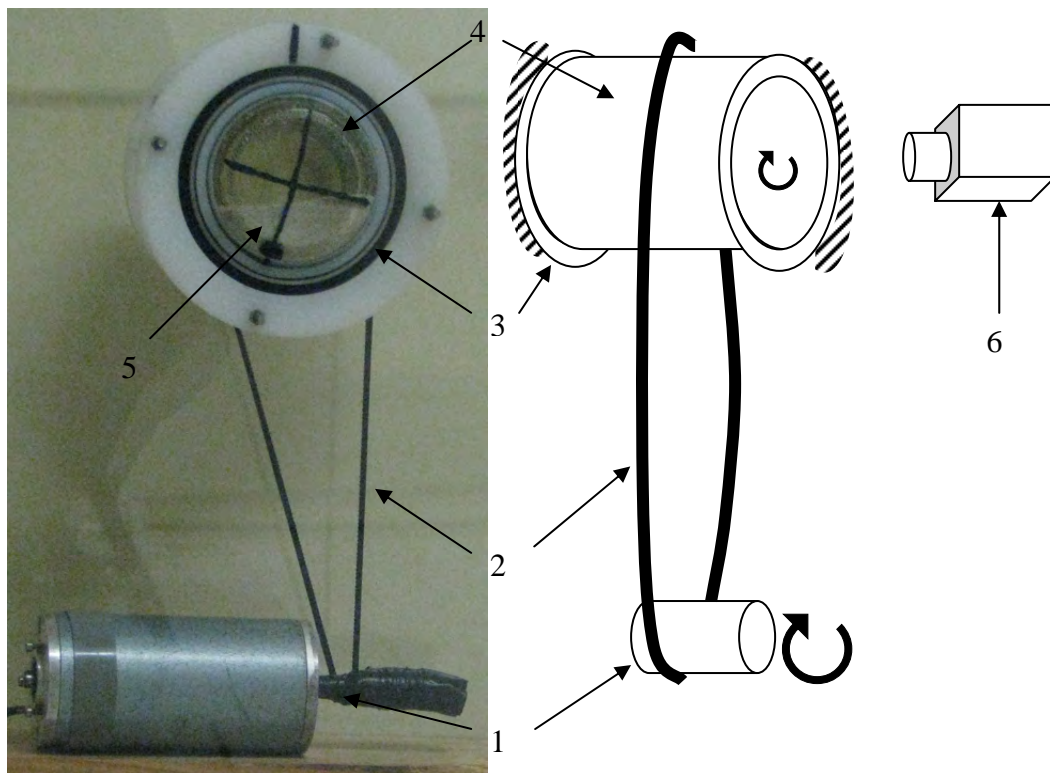


Figure 3.2: Photograph of the experimental setup on the left and its schematic representation on the right, with the electric motor (1), belt (2), bearings (3), container (4), granular material (5) and camera (6).

In Figure 3.3 (a), a sample frame at a speed where the particles do not centrifuge is shown. The markings are clearly visible. In Figure 3.3 (b), a

sample frame is given where the material centrifuges. The light source is blocked as the centrifuging particles line the side wall of the container and do not allow the light inside. A small margin of error is induced by the blur in determining container speed which is estimated to be ± 0.1 rad/s.

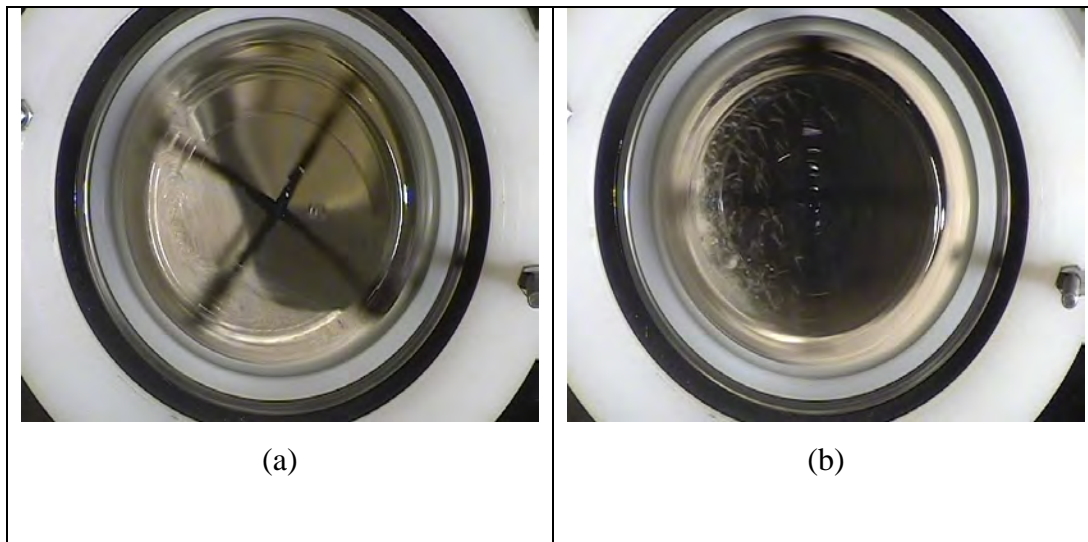


Figure 3.3 (a) Frame from experimental video recording, where the light background and container markings are shown. Slight skew due to high speed container rotation is also apparent. (b) Frame from experimental video recording, where the dark background denotes that the material has centrifuged.

3.3 Numerical model

The use of a numerical prediction tool gives insight in the energy dissipation characteristics of the system. It can also identify the locations where the energy dissipation occurs, what the method of energy dissipation is. In addition, the use of a parametric study enables the identification of how material properties affect energy dissipation and centrifuging speed.

The DEM (Discrete Element Method) solver is the one described in Chapter 2.3 of this Thesis. Its underlying principles have already been established and are omitted for brevity.

The particles used have size and shape parameters which are representative of sand particles, as in the experiments. As in Chapter 2.2, the particles are super-quadric with blockiness parameter n randomly distributed with a uniform probability between 2.5 and 5.0. The super-quadric major axis length is distributed between 0.8 and 1.6 mm, and the super-quadric aspect ratios b/a and c/a between 0.8 and 1.0. The bulk material density is 1600 kg/m³. A stiffness of 600 N/m helps maintain average particle overlaps to be smaller than 0.5% of the particle size. The coefficient of restitution e and the coefficient of friction μ for the sand are 0.75 and 0.70 as determined with simple experiments. The experiments are derived from, but not identical to the one used by [Shinoj Subramanian, R. Viswanathan, Bulk density and friction coefficients of selected minor millet grains and flours *Journal of Food Engineering*, Volume 81, Issue 1, 2007,]. The container is a cylinder with inner radius of 37.5 mm and length of 140 mm, as in the experiments.

Numerically, centrifuging is considered to occur when there is a layer of particles in continuous contact with the boundary. In Figure 3.4 (a), the particles are cataracting. In Figure 3.4 (b), the particles are very close to, but not yet centrifuging, whereas in Figure 3.4 (c), they are centrifuging as all container walls have particles in contact. At that speed, the remaining particles will eventually distribute themselves along the boundary, given sufficient time. Centrifuging is accompanied by a sharp rise in the average number of near neighbor particles, a DEM variable, as shown in Figure 3.4 (d). This variable tracks the particles which are within a certain distance of each particle. The distance is dependant on the spring constant and the time step.

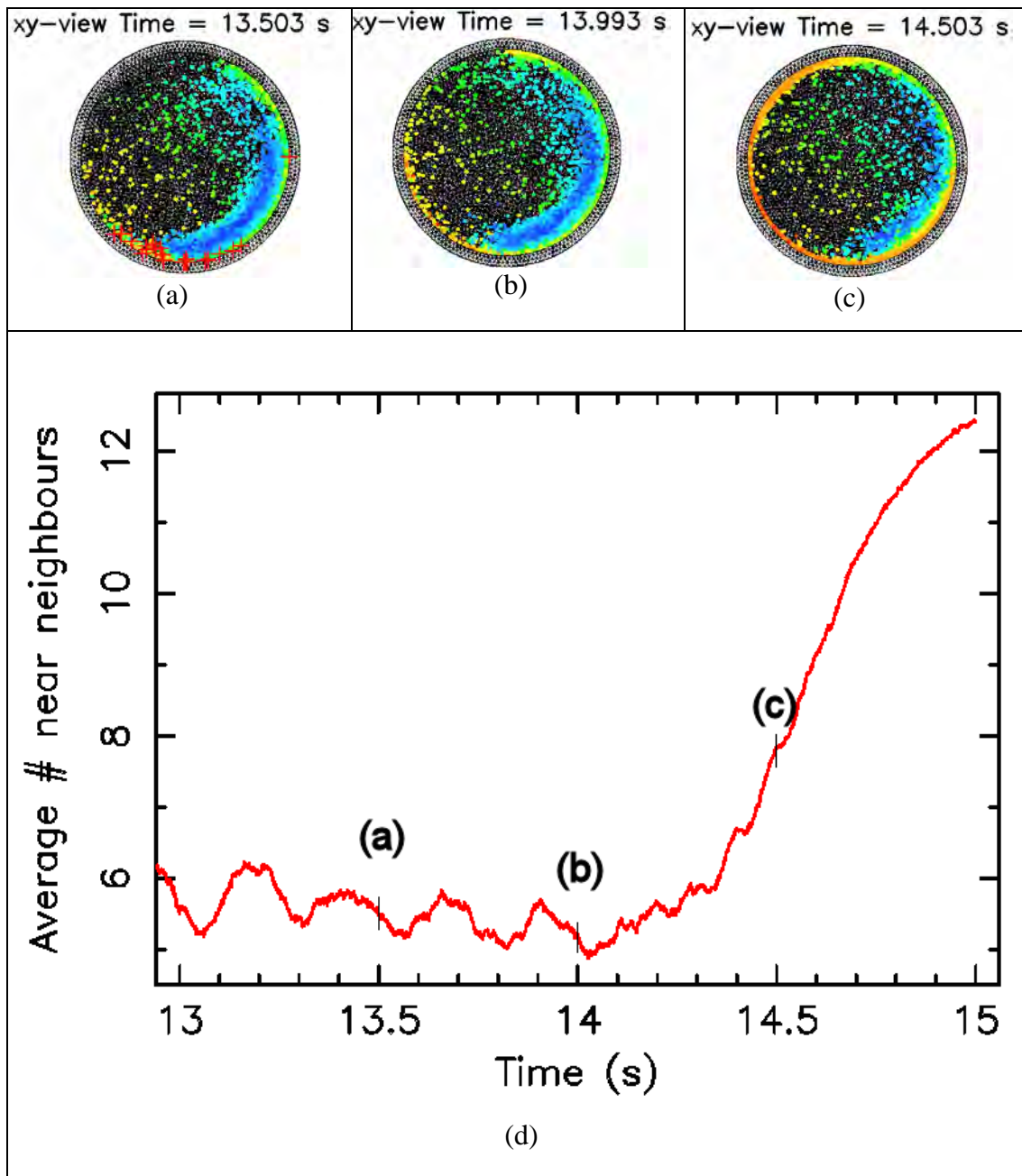


Figure 3.4: Numerical determination of the centrifuging speed. (a), (b) and (c) Granular material flow just prior to and immediately after centrifuging occurs. (d) Average number of near neighbors, a DEM variable, increases considerably when centrifuging occurs in a rotating container.

For all simulations, the container is at first half-filled with particles. Afterwards, the top layers of particles are removed until the required fill level is achieved.

For the simulations where steady flow is required, the container rotational speed is raised quickly to the final speed in discrete steps over 1 second. The simulation is run for ten seconds. Any results presented apply only to the last four seconds of the simulation, where the flow is established.

Simulations using DEM have suggested that energy dissipation increases with the speed of rotation, before the granular material centrifuges, and then, the energy dissipation stops. A set of sample results is presented in Figure 3.5 from the numerical model. In Figure 3.5 (a), the energy dissipation for a granular material is plotted against the tangential speed of the container boundary. The final data point denotes where the granular material centrifuges. The energy dissipation at the centrifuging speed is significantly smaller than the energy dissipation at a speed just prior to centrifuging.

In Figures 3.5 (b) and 3.5 (c) two instances with the highest energy dissipation are shown. The increased red area at the centre of the container and the darker contours at the boundary of Figure 3.5 (c) (for a boundary speed just over 1 m/s), when compared to Figure 3.5 (b) (or a boundary speed of 1 m/s), are indicative of greater boundary speed which leads to greater energy dissipation. Finally, as the boundary speed is too high, the particles are in continuous contact with each other and the boundary, with little relative motion in the container, as shown in Figure 3.5 (d). For an absorber which uses a granular material in a rotating cylinder, maximum energy dissipation occurs just prior to the particle mass centrifuging. Therefore, it is critical to know in advance the speed where such a system centrifuges, to avoid it.

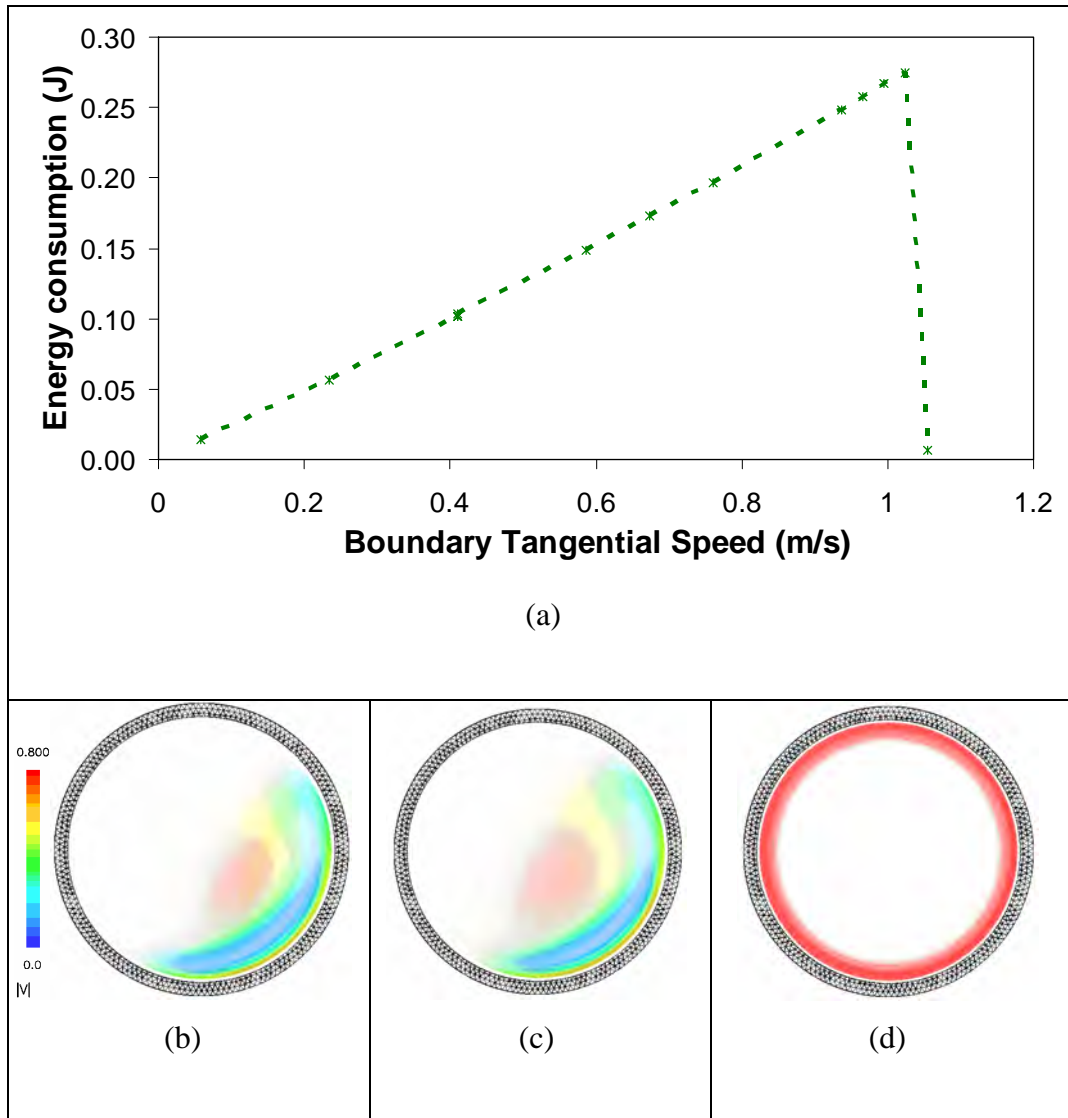


Figure 3.5: (a) Variation of energy dissipation with tangential speed of the container boundary, and velocity contours for just before (b) and (c) and immediately after centrifuge (d).

3.4 Comparison of the predicted and observed critical speeds

To check the validity of the numerical predictions, two approaches were used. Firstly, the critical speeds obtained numerically were compared with the observations. Secondly, flow visualization comparisons were made of the particle distributions obtained numerically with those observed in the experiments.

The numerically obtained critical speeds are compared to the experimental ones for different fill levels in Figure 3.6. The vertical axis is normalized with the simple critical speed expression in Equation 3.1, $(g/R)^{1/2}$. While experimental observations were not possible at the lowest speed levels (because the required rotational speeds were too high for the experimental apparatus) both experiments and simulations predict an increase in the centrifuging speed N_c at the lower fill levels. The numerical tool consistently over predicts the speed of centrifuging by about 10%, at the fill levels tested.

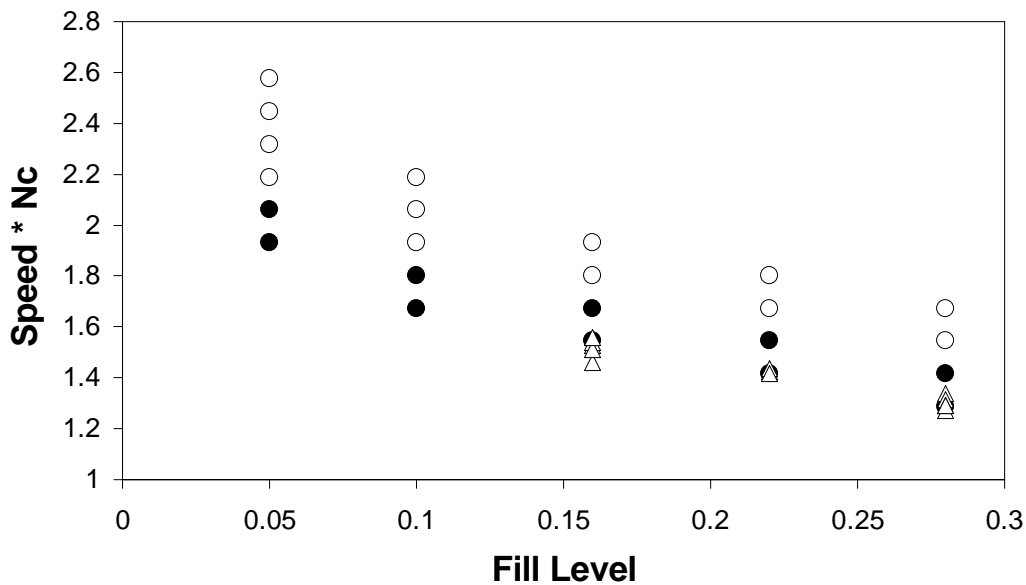


Figure 3.6: Variation of normalized critical speed with fill level. Triangles represent experiments with centrifuging particles, circles indicate numerical results with centrifuging particles and filled circles numerical results where particles do not centrifuge.

This result is important, in showing numerically and experimentally that centrifuging does not occur at $\sqrt{\frac{g}{r}}$, the theoretical critical point. Furthermore, there is an evident inverse relationship between fill level and centrifuging speed.

3.5 Comparison of the predicted and observed particle distribution

Image processing techniques are also used to determine particle distribution over 2 seconds of the simulations and experiments. Each experimental frame is composed of 410000 pixels and each simulation frame of 480000 pixels. Each pixel has an individual value for Red, Green and Blue (RGB) between 0 and 255. If all values are 0, the pixel is defined black, while if they are 255, the pixel is white (Dragomir, 2012). Each pixel's RGB value is separately averaged over 200 frames, and the output is shown in Figures 3.7 (a) and 3.7 (b). For the simulations, each frame is colored using the same fixed scale as shown in Figure 3.7 (a). The resulting image is a true color representation of the average motion in the particular pixel over the time-averaged duration. A lighter tone indicates that the particular pixel (or area) does not always contain particles. In Figure 3.7 (b), the experimental results for a 16% fill level at 20 rad/s are shown. While they both show similar particle distribution, the experiment has a wider range of particle distribution, and thus, the contours are less clear.

The simulations are shown to exaggerate the speed of centrifuging by a small but consistent amount. The numerical results indicate that while energy dissipation increases with the added mass, this increase is not linear for the added mass. In fact, lower fill levels are more efficient dissipaters than higher fill levels, because centrifuging occurs at higher speeds. For low fill levels, boundary interactions account for a greater percentage of dissipation than for high fill levels. In all systems, shear accounts for the majority of energy dissipation.

Material coefficient of friction and density appear to be important to total energy dissipation.

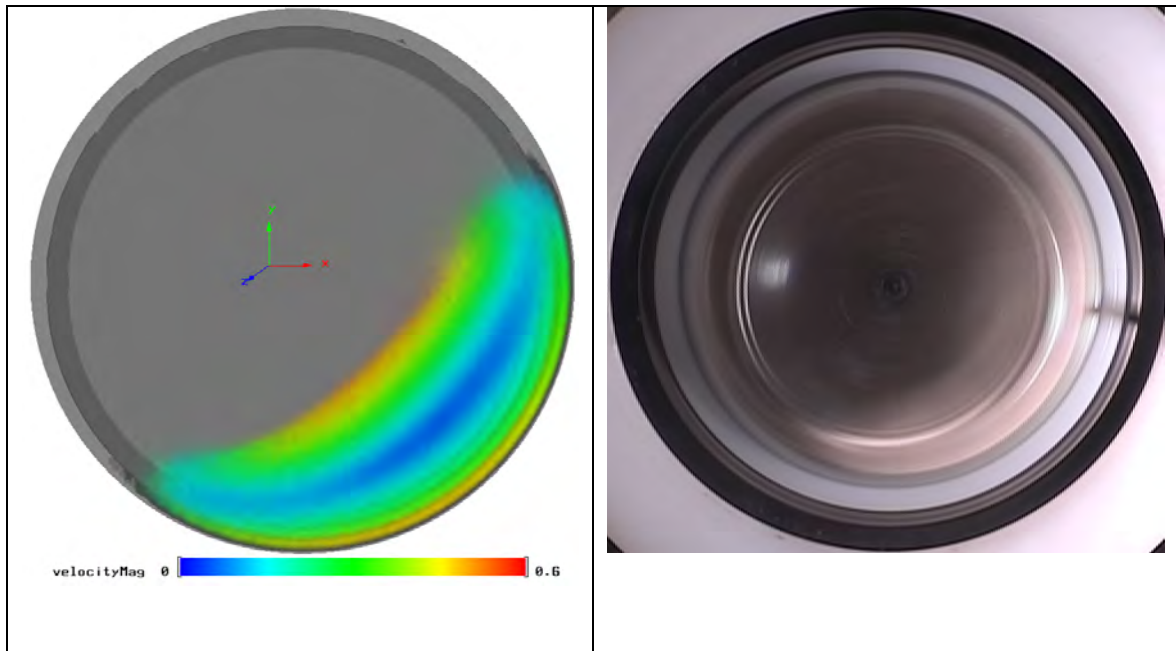


Figure 3.7: Comparison between the time-averaged granular flow from the DEM numerical simulations colored by particle speed (left) and experiment recordings (right) for the 16% fill level at 20 rad/s

3.6 Further flow details from numerical simulations

Since the numerical trends are in agreement with the experimental ones, the numerical results are used here to make further observations which can not be obtained from the experiments. These observations indicate the ideal fill level for maximum dissipation efficiency, the type of particle interactions which account for most of the energy dissipation, the fill levels to minimize the possible wear on the container boundaries, and the coordinates where most of the energy dissipation occurs. This information may then be used to determine particle parameters which most influence the overall dissipation, such that design recommendations can be made for an absorber.

The mass-normalized energy dissipation for different steady boundary tangential speeds are presented in Figure 3.8 for the 5%, 10%, 15% and 20%

fill levels. For any given case, for all speeds lower than the critical speed, the results follow a straight line with an almost constant slope. Hence, the absolute amount of energy dissipation increases linearly with the fill level. However, since the higher fill levels centrifuge at lower speeds, the lower fill levels may be more efficient dissipaters, if higher rotational speeds are feasible.

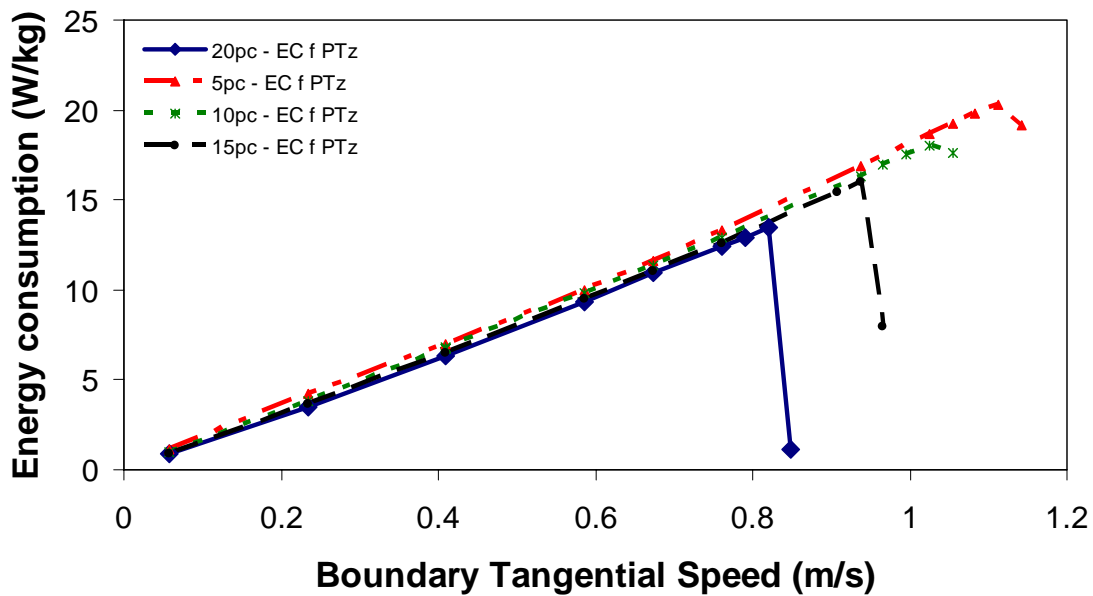


Figure 3.8: Variation of energy dissipation with boundary speed for 5%, 10%, 15% and 20% fill levels. Final data point denotes a simulation where centrifuging occurs.

All interactions in DEM have a normal component and a tangential component. For all the steady speed simulations and the parameter ranges used, it has been found that shear accounts for over 70% of the total energy dissipation in the system. In Figure 3.9, the percentage of energy dissipation is plotted for the boundary speed. While higher rotational speeds lead to more energy dissipation through head-on collisions due to airborne particles, the predominant form of dissipation remains to be shear. It is interesting to note that the results are rank-ordered, with the lower fill levels having a greater overall percentage of energy dissipation through head-on collisions. This

result is not surprising since more energetic particle motion is expected at low fill levels.

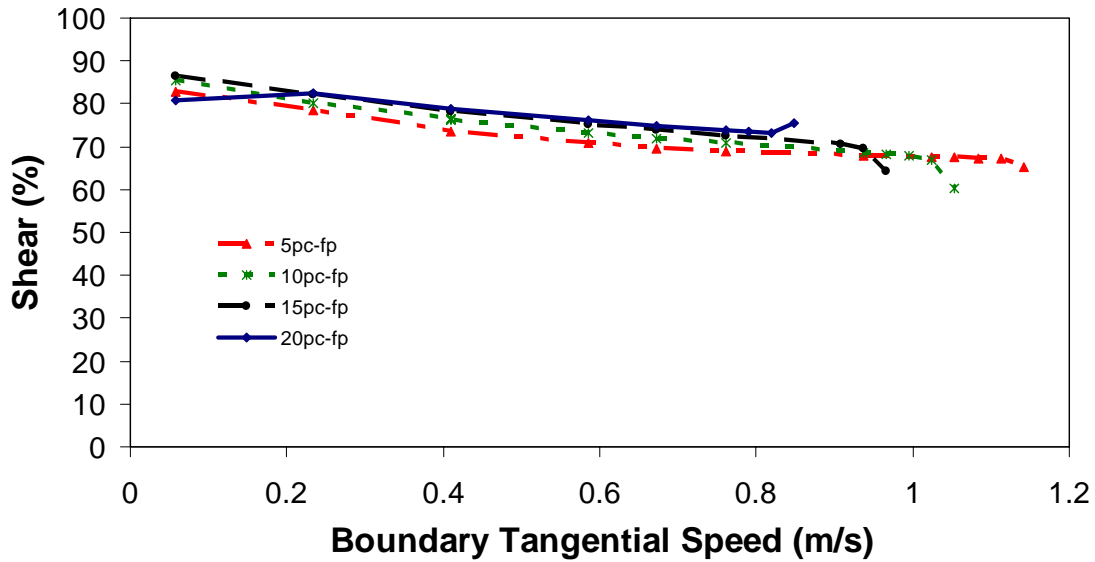
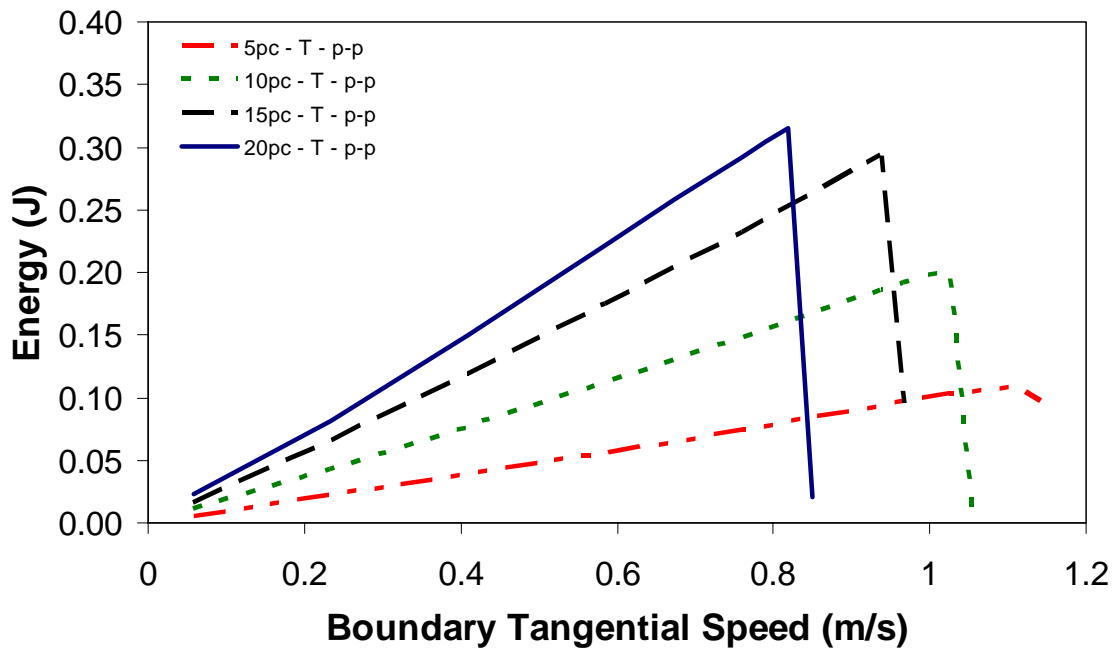
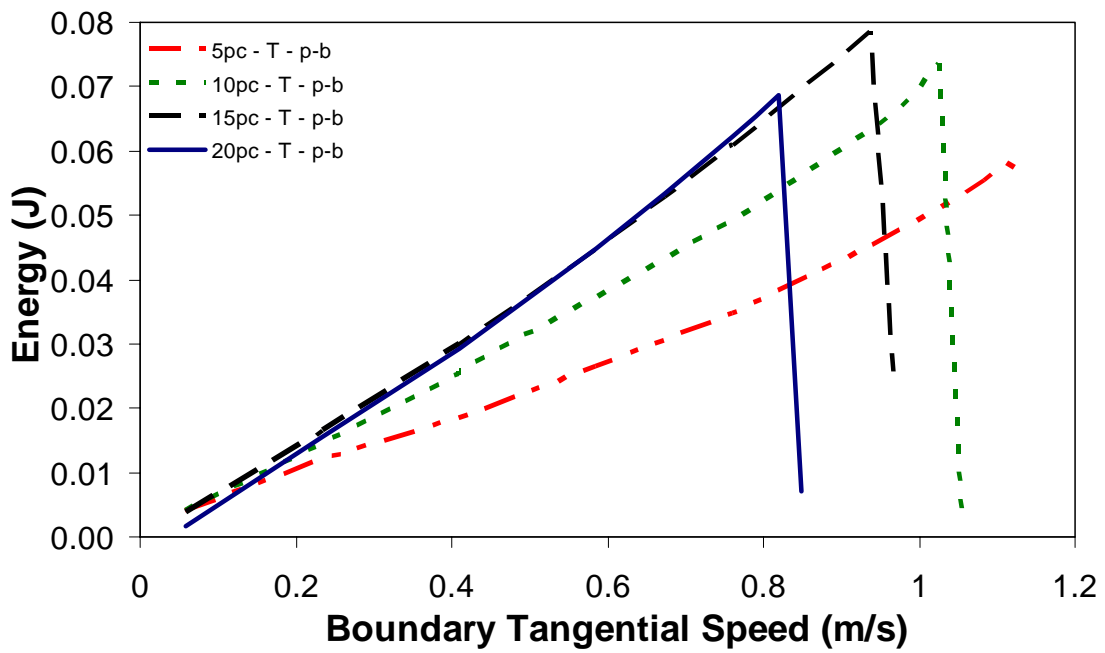


Figure 3.9 Variation of percentage shear dissipation of total energy dissipation for different boundary speeds

Energy dissipation can also be classified based on whether the dissipation occurs in collisions with the boundary or collisions among particles. Collisions involving only particles-particle interaction are plotted in Figure 3.10 (a), while collisions with the boundary are plotted in Figure 3.10 (b). The vertical axis represents the energy dissipation while the horizontal axis represents the boundary tangential speed. The scale for Figure 3.10 (b) (boundary) on the vertical axis is 20 times larger than that for Figure 3.10 (a) (particle collisions). For inter-particle collisions the energy dissipation increases almost linearly with fill level between 5% and 15%. However, there are diminishing returns past 15%. For collisions involving the boundary, the 20% fill level dissipates comparable energy at the boundary as that of the 15% fill level.



(a)



(b)

Figure 3.10 Comparison between energy dissipation through inter-particle collisions (a) and energy dissipation involving the boundary (b)

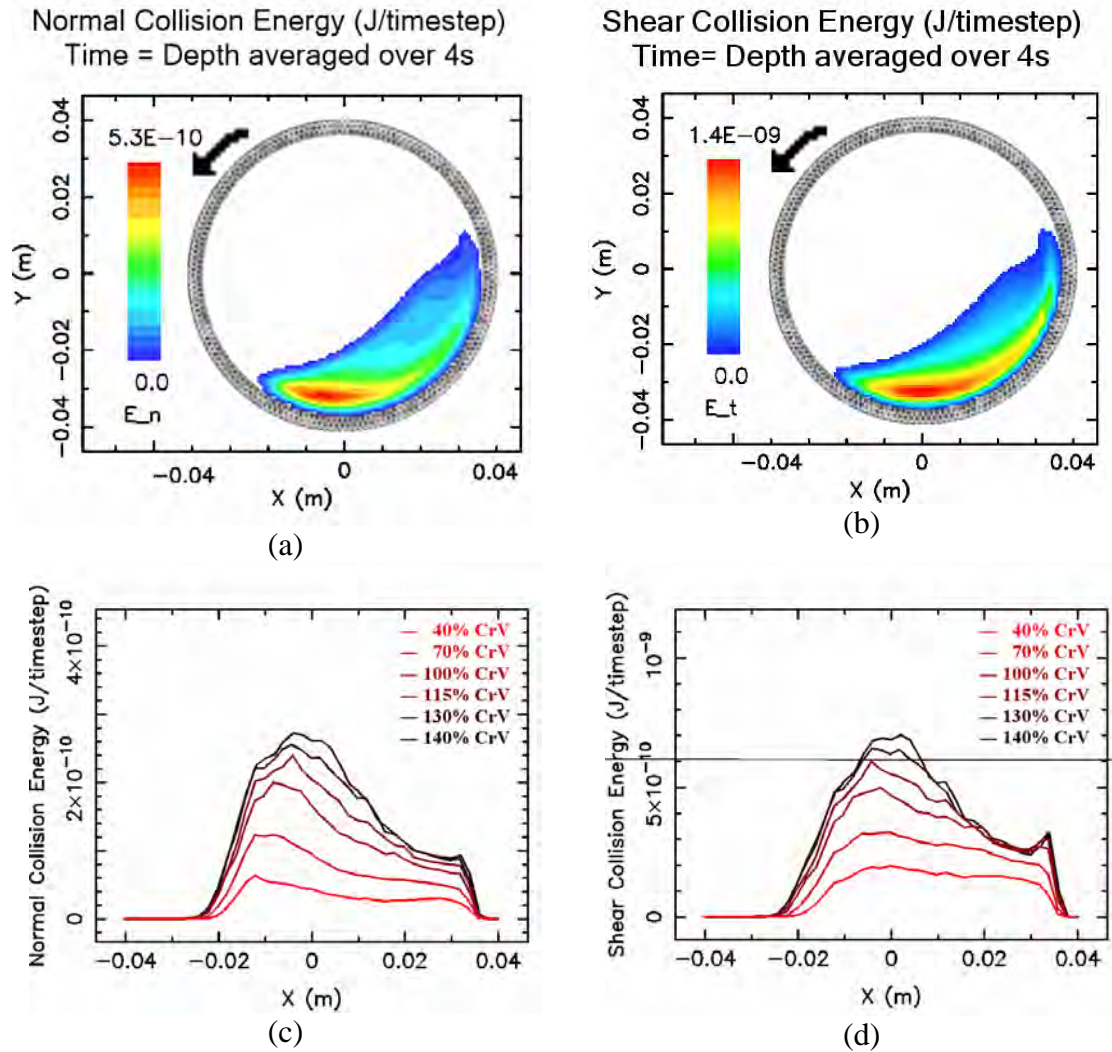
For the 5% fill level, the boundary collisions just before centrifuging (0.058 J) account for 37.5% of the overall dissipation (0.166). For the 10% fill level, they account for 25%; while for the 15% fill level, boundary collisions account for only 21% of the dissipation. These results indicate that any absorber design would need to consider boundary wear, especially for the lower fill levels, where a significant amount of the energy dissipation is due to collisions with the boundary.

Finally, the location where the energy dissipation occurs in the particle bed is important such that suitable materials or container designs can be used for the absorber. For this purpose a 3-dimensional grid is set over the volume of the container. For each grid element, normal and shear collision energies are averaged over 4 seconds. The resulting smoothed data for the 20% fill level and 0.4 m/s boundary speed is presented in Figures 3.11 (a) and 3.11 (b) for the normal and shear energy dissipation, respectively. The energy dissipated during each time step is averaged over 4 seconds, for each grid element.

In the 2D view shown, the events along the cylinder axis are averaged. The scale for the shear dissipation in Figure 3.11 (b) is approximately 3 times larger than that for the normal dissipation. Red indicates regions of highest dissipation, while blue denotes regions of lowest dissipation. The red areas of the two pictures are similar, with a peak at the bottom /centre of the container and a tail following the boundary. Other fill levels show similar behavior and are omitted for brevity.

In order to better compare the areas where energy dissipation occurs between simulations, both the normal and shear data are averaged along the vertical and horizontal axes, resulting in Figures 3.11 (c), 3.11 (d), 3.11 (e) and 3.11 (f). In Figures 3.11 (c) and 3.11 (d) respectively, the normal and shear collision

dissipation is given along the X-axis. Similarly in Figures 3.11 (e) and 3.11 (f), normal and shear dissipation is given along the Y-axis. The scale for the shear dissipation is approximately 4 times larger than that for the normal dissipation. The different color lines are the tangential speeds, with the red line being the lowest speed and the black line the highest.



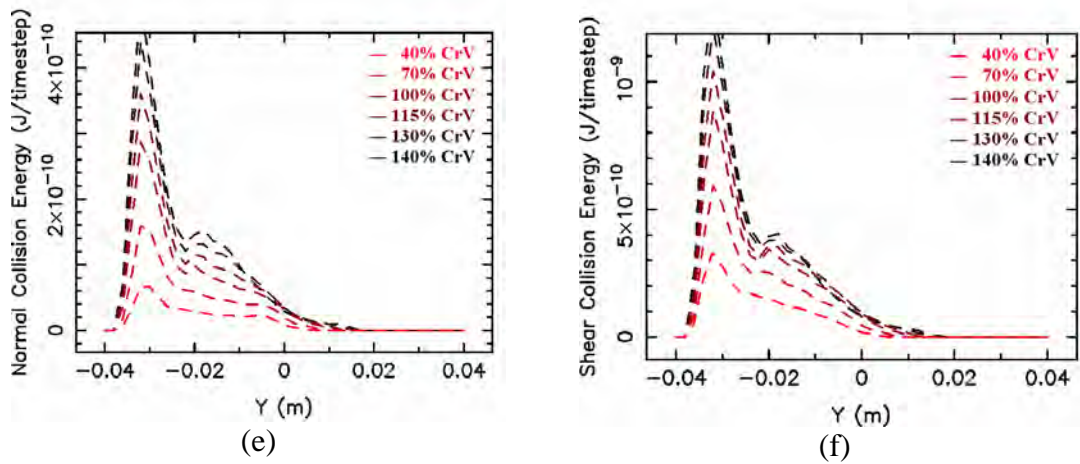


Figure 3.11 Graphical representation of energy dissipation. (a) and (b): 2D image of normal and tangential dissipation, averaged over the third dimension. (c), (d), (e) and (f): comparisons of energy dissipation for different boundary speeds averaged along the vertical (Y) and horizontal (X) axes for the normal and tangential collision components, respectively. CrV is the critical speed $\sqrt{g/r}$.

The location of the peak dissipation does not appear to change in either the X or Y direction for either the shear or normal dissipation component. The dissipation occurs mostly in the area centered around (0,-0.03). This area is elongated in the horizontal direction, but quite small in the vertical similar to the red area shown in Figures 3.11 (a) and 3.11 (b). Higher boundary speeds increase the energy dissipation magnitude, but do not increase the area of dissipation. A possible explanation for this pattern is that the dissipation is driven by gravitational forces acting on the material at the direction where their motion changes directions.

From these observations a number of conclusions can be drawn on what drives the energy dissipation in the system, such that the effect of material properties can also be investigated. Since more than 70% of the energy dissipation is due to shear, the coefficient of friction for the material used should have a significant effect on the outcome of the energy dissipation. As

the gravitational forces are shown to be important in the dissipation, the density of the material should also affect the energy dissipation in the system. Finally, the coefficient of restitution is responsible for the amount of the incident energy dissipated in a collision and the speed a particle carries after a collision. Therefore, a higher coefficient of restitution should lead to a greater number of collisions and thus higher rate of energy dissipation. These assertions are examined in the parametric study presented next.

3.7 Parametric Study

The objective of this section is to demonstrate the relative importance of the three seemingly significant design parameters on the critical centrifuging speed. These parameters are the coefficients of friction (to determine dissipation in tangential interactions) and restitution (to determine relative amount of kinetic energy dissipation in normal interactions) and the mass density (to determine the amount of kinetic energy available for dissipation) of the particles for a given shape, as discussed earlier. The three parameters and the three different levels at which they are considered are listed in Table 3.1. The middle level of each parameter is the nominal one used in the preceding discussion. The volume fraction of particle fill is maintained at 20%.

Table 3.1. Levels of the three design parameters.

Parameter	Low level	Medium level	High level
friction coeff., μ	0.5	0.7	0.9
rest. coeff., e	0.6	0.75	0.9
density, ρ (kg/m^3)	1232	2465	4930

The procedure of investigation is the same as that is used in complex manufacturing processes, to determine the effect of design parameters on the desired outcome through experimentation, as shown by (Lochner and Matar, 1990). Hence, the experiments involve 27 distinct combinations of three design parameters at three levels. The objective is to maximize the value of the critical speed which causes the particles to centrifuge. The numerical procedure to establish the value of the critical speed is presented next.

Determining the critical speed would ideally require a simulation run at an estimated constant speed, and incrementing it up and down until the centrifuge is established. Hence, each parameter combination may involve up to 10 trial simulation runs. Considering the 27 distinct parameter combinations, this procedure would require significant computational effort. A faster procedure was implemented to approximate the value of the required speed.

The compromise procedure involves incrementing the speed of rotation until centrifuge in one simulation run. After each speed increment of 1 rad/s, a one second duration is allowed as a “settling time”. If the last incremented speed has reached the critical speed, the particles centrifuge during the settling time, and the current speed is recorded as the critical speed. The history of rate of energy dissipation for one such run is shown in Figure 3.12. In this figure, the blue line is the dissipation data, whereas the speed of rotation is represented by the red line. First, the speed is rapidly increased to 20 rad/s over 2 s. After 2s, the speed is incremented by 1 rad/s at every second until centrifuging occurs at 14 seconds (31 rad/s).

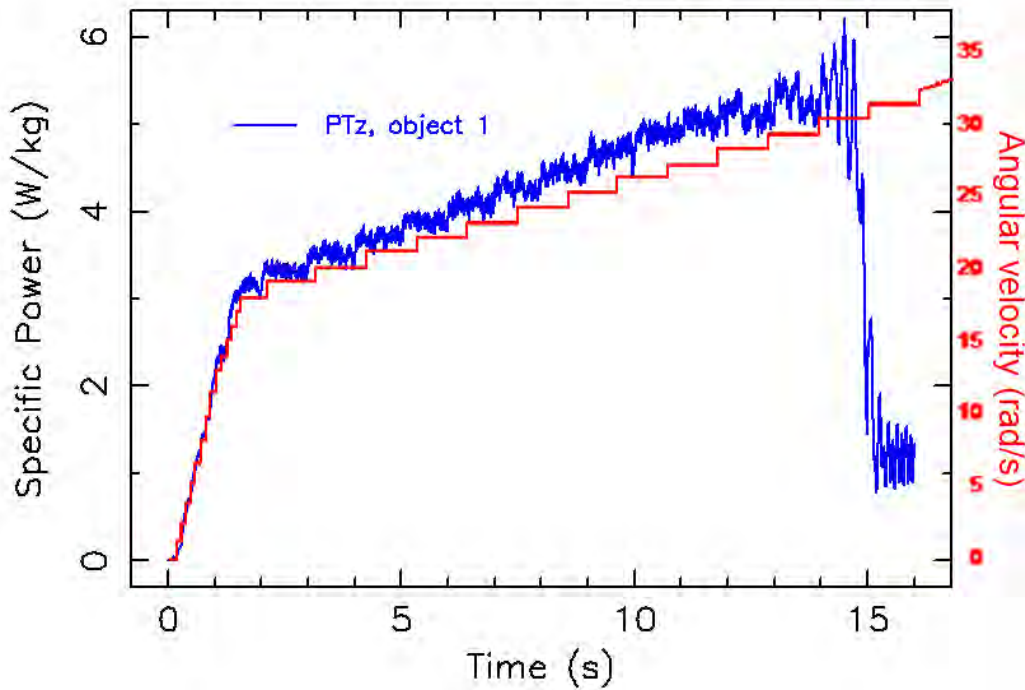


Figure 3.12: Energy dissipation for a system where the speed is increased in discrete steps.

The critical speed in Figure 3.12 corresponds to the same value when compared with constant speed of rotation. The same abrupt drop in the dissipation can be observed as the granular material centrifuges. In addition, no sudden change in behavior could be observed as the speed of rotation is incremented. None of the cases reported in this section, centrifuged immediately after a speed increment, but required some settling time which led to the assumption that the suggested approximation procedure was sufficiently accurate. Numerically, a centrifuge was established using the number of near neighbors as an indication, as discussed earlier in relation to Figure 3.5 (a).

A summary of the 27 cases is given in Table 3.2, in the format of a Response Table [Lochner and Matar, 1990]. In Table 3.2, first column indicates the standard order of each case, as also marked in the shaded columns on the right part of the table. For instance, the standard Case Number 1 (where N_c is

marked as 40 rad/s in the second column), corresponds to the simulation run for μ_1 (0.5), e_1 (0.6) and ρ_1 (1232 kg/m³). Case 2, maintains μ_1 and e_1 , but increments to ρ_2 , and so on.

The critical area of Table 3.2 is its last row where the average critical speed is marked for each level of the three parameters. These values correspond to averages of 9 cases each, since each of the three levels exist equally as 1/3rd of the total number of 27 cases. For instance, the average critical speed of 38.3 rad/s for μ_1 is obtained by averaging the critical speeds of the first 9 cases where the friction coefficient is set at μ_1 , regardless of the values of e and ρ . For e_1 , 33.7 rad/s corresponds to the average of Cases 1-3 and 10-12 and 19-21. For ρ_1 , 33.2 rad/s is the average of Cases 1, 4, 7, 10, 13, 16, 19, 22 and 25. The information in Table 3.2 will be discussed first to indicate the direct effect and the relative importance of the design parameters. Then the possible interactions among these parameters are examined at their respective levels.

Direct effect of the three design parameters are marked in Figure 3.13 where the vertical axis indicates the averages from Table 3.2. The mean critical speed of 33.2 rad/s is marked by the horizontal line. The average critical speed changes minimally from 33 rad/s and 33.2 rad/s for the 4-fold change in the mass density ρ . For the coefficient of restitution, the change is somewhat more significant, from 32.1 rad/s to 33.7 rad/s, the larger value corresponding to the smaller two coefficients of 0.6 and 0.75. The most dramatic change corresponds to the friction coefficient. Smallest friction coefficient of 0.5, resulting in the largest critical speed of 38.3 rad/s, the largest friction coefficient of 0.9, giving 29.5 rad/s. Hence, the friction coefficient is by far the most important parameter in determining the value of the critical speed. The coefficient of restitution is significantly less important than friction. Effect of the mass density is negligible.

Table 3.2. Standard Response Table of the three design parameters on the critical speed.

Standard Order	Speed (rad/s)	μ			e			ρ (kg/m ³)			
		0.5	0.7	0.9	0.6	0.75	0.9	1232	2465	4930	
		1	2	3	1	2	3	1	2	3	
1	40	μ_1			e1			ρ_1			
2	40	μ_1			e1				ρ_2		
3	39	μ_1			e1					ρ_3	
4	39	μ_1				e2		ρ_1			
5	39	μ_1				e2			ρ_2		
6	39	μ_1				e2				ρ_3	
7	37	μ_1					e3	ρ_1			
8	36	μ_1					e3		ρ_2		
9	36	μ_1					e3			ρ_3	
10	32		μ_2		e1			ρ_1			
11	32		μ_2		e1				ρ_2		
12	32		μ_2		e1					ρ_3	
13	32		μ_2			e2		ρ_1			
14	32		μ_2			e2			ρ_2		
15	32		μ_2			e2				ρ_3	
16	31		μ_2				e3	ρ_1			
17	31		μ_2				e3		ρ_2		
18	31		μ_2				e3			ρ_3	
19	29			μ_3	e1			ρ_1			
20	30			μ_3	e1				ρ_2		
21	29			μ_3	e1					ρ_3	
22	30			μ_3		e2		ρ_1			
23	30			μ_3		e2			ρ_2		
24	30			μ_3		e2				ρ_3	
25	29			μ_3			e3	ρ_1			
26	29			μ_3			e3		ρ_2		
27	29			μ_3			e3			ρ_3	
Average	33.15										
			38.3	31.7	29.4	33.7	33.7	32.1	33.2	33.2	33

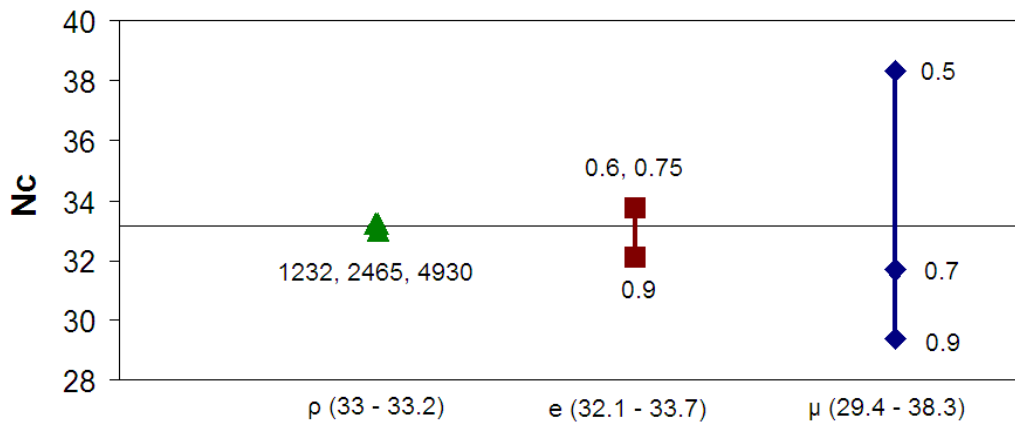


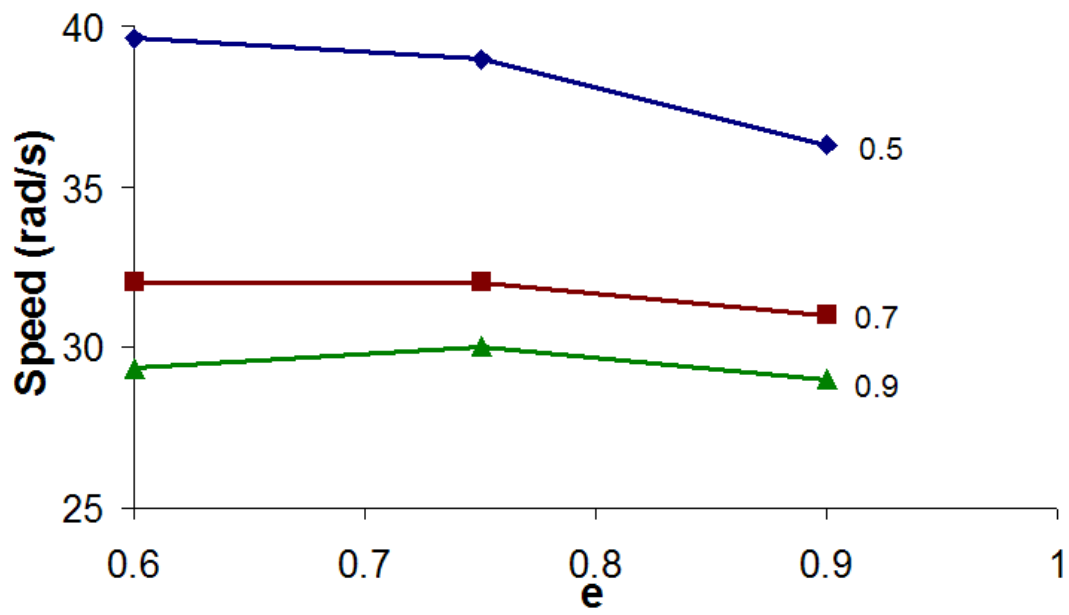
Figure 3.13: Direct effects of material properties, ρ , e and μ , on the critical speed, N_c

Having established a rank order of importance of the three design parameters, the possible interactions among these parameters are examined next, with the information presented in Figure 3.14. In Figure 3.14 (a), variation of the critical speed is given with the coefficient of restitution at the three levels of the friction coefficient. For the top line where $\mu = 0.5(\blacklozenge)$, for instance, the left-most point (of $\mu = 0.5$ and $e = 0.6$), is the average of Cases 1, 2 and 3 for the three values of the mass density. The next point (of $\mu = 0.5$ and $e = 0.75$) is the average of Cases 4, 5 and 6, whereas the last point (of $\mu = 0.5$ and $e = 0.9$), is the average of Cases 7, 8 and 9. This averaging isolates the variation of only two parameters at a time.

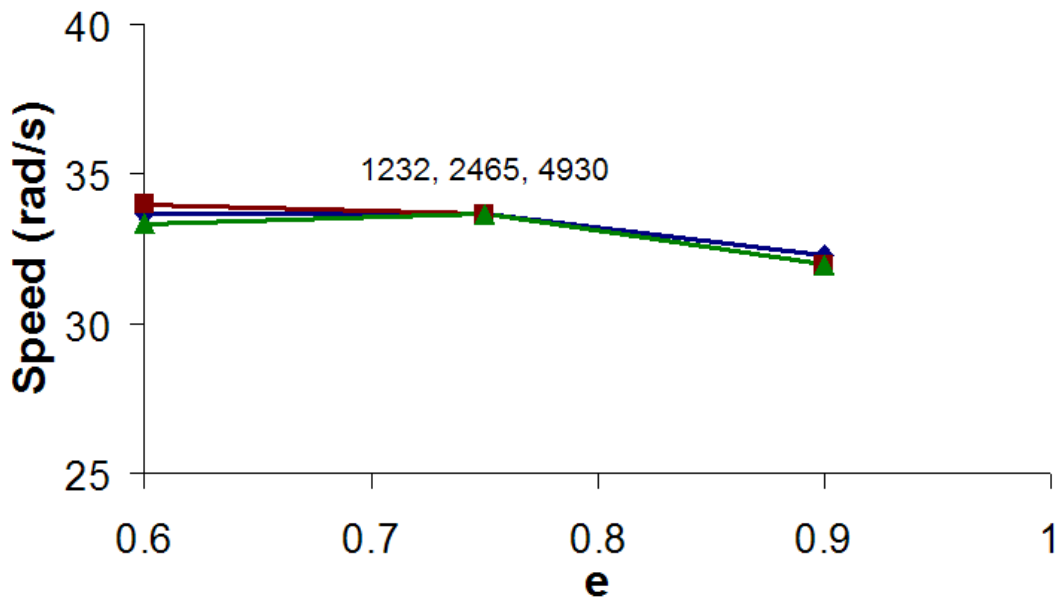
In Figure 3.14 (a), effect of varying the coefficient of restitution from 0.6 to 0.9 is negligible for the two larger friction coefficients of 0.7(\blacksquare) and 0.9(\blacktriangle). For the smallest friction coefficient of 0.5(\blacklozenge), on the other hand, there is a clear trend of deteriorating critical speed with increasing coefficients of restitution. The highest critical speed corresponds to the smallest values of $e = 0.6$ and $\mu = 0.5$. No strong interaction is present between μ and e , with all three lines approximately parallel to each other.

In Figure 3.14 (b), effect of varying the coefficient of restitution is negligible for all values of the mass density. Similarly, the same is true for the variation of the friction coefficient for different mass densities, as shown in Figure 3.14 (c). In this figure, the strong dependence of the critical speed on the friction coefficient is reinforced clearly with the downward trend for increasing friction coefficient. Neither of the two trends in Figures 3.14 (b) and 3.14 (c) represent any significant interaction between e and ρ , and μ and ρ .

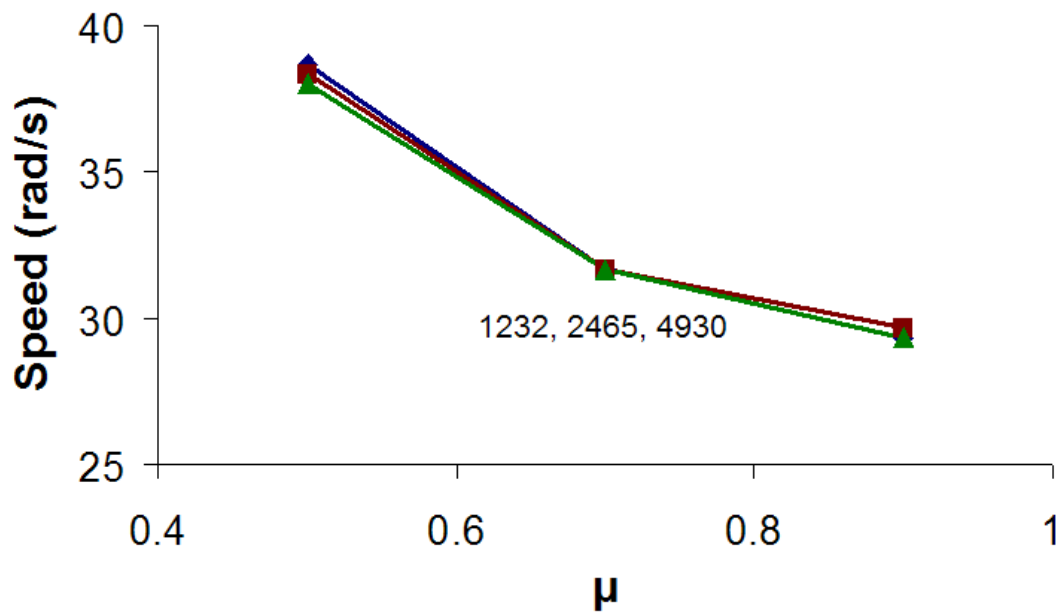
The numerically observed critical speeds for the parametric study in this section, are compared with the two predictions discussed earlier in relation to Equations 3.1 (Rose et al. 1958) and 3.2 (Watanabe 1999). Briefly, the first one is the standard approach which balances the gravitational acceleration with the centrifugal acceleration, discounting the interactions of particles. The second one is a significant improvement involving the fill level, and the angle of repose of the particles. Figure 3.15 includes the prediction of the critical speed for different angles of repose, from Equation 3.1, Equation 3.2, and the new values as scatter points. Angle of repose of the new values is obtained numerically by simulating a pour on a flat surface, with an estimated accuracy of ± 0.5 degrees through visual inspection. The critical values have an uncertainty of ± 0.5 rad/s, since 1 rad/s speed increments were used for their determination



(a)



(b)



(c)

Figure 3.14: Variation of the critical speed with (a) e at three different levels of μ , (b) e at different levels of ρ , and (c) μ at different levels of ρ

Not surprisingly, the standard approach marked as a dashed horizontal line in Figure 3.15, clearly underestimates the critical speed by up to 100%. The modified approach, on the other hand, does quite well, predicting 21 out of 27 cases well within 10%. Since the predictions reported in this section indicate the friction coefficient to be the only parameter of significance, and since the friction coefficient directly affects the angle of repose, this close comparison should not be a surprise. The outlying data points all represent numerical results with the coefficient of friction at the low level, and either the material density or coefficient of restitution also at a low level. Since they do not represent realistic materials they could indicate a breakdown of the model at such extremes. This indicates that care needs to be exercised when working with numerical models and that experimental validation is normally required.

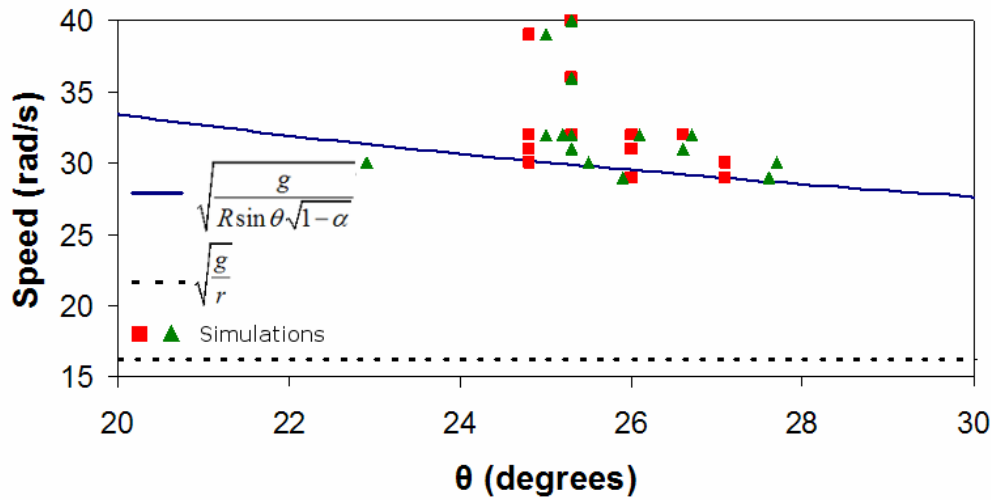


Figure 3.15: The variation of the critical speed N_c with the angle of repose, θ . The predicted N_c from Equation 2, and the standard balance of centrifugal and gravitational accelerations are marked, along with the discrete points from the current study.

3.8. Conclusions

A rotating cylinder partially filled with a granular material attached to a structure, can be used as an energy sink. The energy dissipation increases linearly with the speed of rotation up to a critical speed, when the particle charge centrifuges, and the energy dissipation drops abruptly. Experimental and numerical results have shown that for fill levels under 20%, the standard model with $N_c = (g/R)^{1/2}$ grossly underestimates centrifuging speed.

Overall energy dissipation increases linearly between 5% and 15% fill level at a given speed of rotation. However, diminishing returns are found thereafter. The mass-normalized dissipation is steady across fill levels for low speeds, but at high speeds where the higher fill levels centrifuge, lower fill levels do not, thus becoming more effective dissipaters. On the other hand, because there are more boundary collisions which account for a greater percentage of the

energy dissipation, an absorber where the fill level is too low (less than 10%) will require high maintenance, as illustrated in Section 3.6.

Parameters which are likely to have an effect on energy dissipation are considered in a parametric study to maximize the critical speed.

Additional insight is gained through the use of a validated DEM numerical solver through the variation of material properties leads to a better understanding of into the dissipation mechanism. Critical speed is affected by fill level, angle of repose, coefficient of friction, and to a smaller extent, coefficient of restitution:

- a higher fill level implies a lower N_c ,
- a higher angle of repose implies a lower N_c ,
- a higher coefficient of friction corresponds to a lower N_c , and
- a higher coefficient of restitution corresponds to a lower N_c at times.

The highest critical speed reached numerically is for a low coefficient of restitution and friction, and a low density material. However, the material density does not make a significant contribution to the critical speed. The coefficient of friction has a higher effect on the critical speed determination than the other parameters. A material with a low coefficient of friction allows much higher rotational speeds of the container before centrifuging occurs. To further verify the numerical tool, the parameters used for the parametric study are utilized to calculate the angle of repose with which critical speeds are calculated. The values compare favorably with the empirical expression available from the literature.

In an application where maximizing energy dissipation in a rotating cylinder is important, once the material mass is normalized, the speed at which material centrifuges is the critical remaining factor. To this end, a material with a low coefficient of friction is needed.

The DEM solver used for the sensitivity to material properties study mildly over-estimates the centrifuging speed when compared to the experiments as well as existing expressions from the literature. This solver has shown to be a useful tool for the design of a granular sloshing absorber.

4 Experiments to control structural vibrations with granular flow damper

4.1 Introduction

Tall, flexible structures are susceptible to wind or earthquake induced vibrations. These vibrations, usually at low frequencies –at or below 1 Hz, can be detrimental to structural safety and people comfort. Tuned mass dampers (TMD) have been traditionally used to suppress excessive vibrations of the structures, as they can be effectively tuned at the natural frequency of the structure onto which they are attached. The tuning ensures effective transfer of harmful energy from the structure to the controller. However, a damping element is required in the controller, in order to prevent the return of the energy to the structure. This returned energy causes a beating envelope of oscillations, representing instances where most of the harmful energy resides, in the structure or in the controller.

Presence of damping should avoid the undesirable beat, dissipating the received energy in the controller, without giving it an opportunity to return back the structure. The required level of effective damping in the controller is in the order of 20% of critical damping (Liu et al. 2005). Hence, although the tuned mass dampers are a proven remedy, the requirement of such high levels of damping introduces practical problems of maintenance in dissipative elements. Other damper designs may prove to be more practical than TMDs.

Of particular interest are dampers which use a granular material to dissipate the harmful energy. An earlier approach reported in (Papalou and Masri 1992) uses a cavity partially filled with a granular material which is built into the structure to be controlled. As the structure vibrates, the granular material is

energised and dissipates energy through collisions and shear among the particles and with the cavity's boundary (Papalou and Masri 1992). An alternative approach uses a single large sphere which interacts with its slightly larger spherical enclosure. The enclosure is placed near the top of the structure and moves out of phase with the structure similar to a TMD. Out of phase motion is assured by tuning the pendulum frequency of the controller sphere in its cavity. The energy dissipation is primarily due to the surface friction between the particle and the enclosure (Fischer, 2007).

For all these controllers, the amount of mass added to the structure for the purpose of dissipating harmful energy is a significant consideration. Considering the effective mass of a tall building, in the order of hundreds to thousands of tons, the mass of the controller has to be minimised to avoid the penalty of excessive added mass. Therefore, a small mass ratio of damper to that of the structure, say in the order of 1%, is highly desirable. Typically, TMDs can only achieve such a small mass ratio when they are employed as part of an active control strategy. Active control requires sensing-computing-implementing the control action. Therefore it is expensive, and it needs constant monitoring and maintenance.

An alternative design is proposed here which uses a cylindrical container, partially filled with a granular material. The container is allowed to roll on a curved ramp that is part of the structure, and the granular material acts as the energy sink. A schematic representation of the design is shown in Figure 4.1 where the structural mass, viscous damping coefficient and stiffness are represented by m , c and k .

As the structure oscillates, the cylinder rolls due to inertial and gravitational forces. The radius L through which the centre of the cylinder moves can,

therefore, be designed to achieve any desired the frequency of the cylinder, using the pendulum analogy

$$f = \frac{1}{2\pi} \sqrt{\frac{g}{L}}$$

where g is the gravitation acceleration and f is the frequency in Hz. Although several enhancements have been suggested to this expression (Kraig and Johnson, 2005), the simplest form appears to produce close estimates of the frequency.

Tuning is achieved by matching the pendulum frequency of the damper to the natural frequency of the structure. The energy sink is provided by the collisions of the granular material and by friction. The advantage of this design over the conventional tuned mass damper is its ability to produce significant levels of dissipation with mass ratios in the order of 1%. In addition, it is a passive device, maintaining simplicity and low cost.

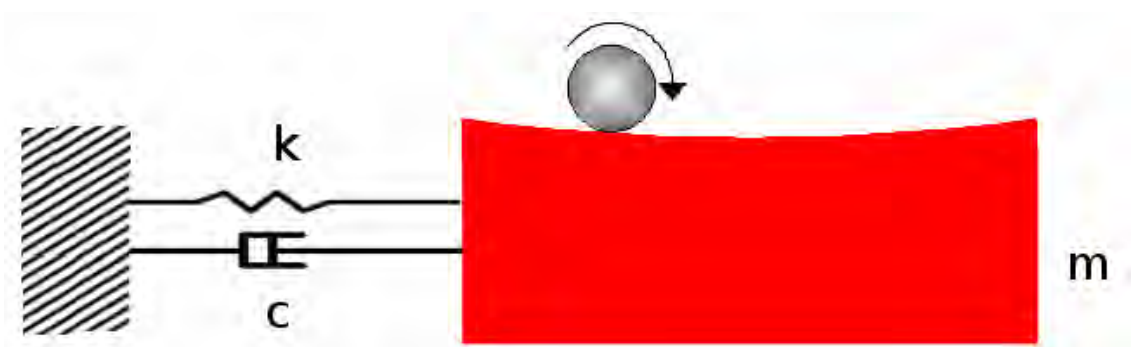


Figure 4.1: Schematic representation of the proposed absorber design.

In this chapter, the experimental observations are presented to demonstrate the effectiveness of the suggested design. The importance of tuning is

discussed and sensitivity of the performance to different levels of external disturbance is presented.

4.2 Experimental Setup

A simple experiment is designed to demonstrate the capability of the suggested control using granular flow. As shown in Figure 4.2, a cantilevered strip of mild steel (Item 1) is representative of a tall, lightly damped building. The strip is clamped to a stand. A curved ramp is attached to a platform (2) at the top of the structure. The ramp (3) is made from Perspex and its curvature is adjusted using turn screws and turn-and-buckles on either side. There are 5 holding points which give an approximately circular shape to the ramp. A plastic hollow cylinder (4) partially filled with a granular material (sand) provides the energy sink. In Figure 4.2 (a) a photograph of the curved track and support structure are given, and in Figure 4.2 (b) a schematic representation of the same is shown. The parameters for the structure and cylinder are listed in Table 4.1

The experiment consisted of giving the structure an initial displacement in the horizontal direction, using the bump stop in Figure 4.2 (5) and then allowing it to come to rest. Video recordings of the motion of the ramp and cylinder are then digitized and displacement histories for the horizontal direction are obtained. The measurements have an error margin of ± 0.65 mm (± 0.5 pixel). Recording speed of the camera is 50 frames/s.

Table 4.1: List of relevant experimental parameters. Estimated uncertainty in the reported length and mass values are ± 1 mm and ± 1 g, respectively.

Length of strip	: 780 mm
Depth of strip	: 3 m
Width of strip	: 50 m
Equivalent mass of structure	: 9.68 - 11.1 kg (calculated) $m_{eq} = \frac{(2\pi f_n)^2}{k_{eq}}$
Equivalent spring stiffness of structure	: 142 N/m (calculated) as $k_{eq} = \frac{3EI}{l^2}$
Natural frequency of structure	: 0.57Hz – 0.61 Hz (measured) (changes with ramp configuration)
Structure equivalent viscous critical damping ratio	: 0.001 (measured) ± 0.0001
Volume of container	: 950 cc
Radius of container	: 40 mm
Depth of container	: 200 mm
Mass of container	: 100 g
Mass of sand (1% fill level)	: 7 g

Aside from the tuned case with 0.7 m radius, two other ramp radii are considered, one with a radius of 0.5 m and another with a radius of 0.9 m. The natural frequency of the structure changes slightly with the ramp radius due to the distribution of mass at the top of the structure.

The initial displacement is managed through the use of a bump stop. Initial displacement is considered to be centimetres away from rest position of the centre of the ramp in the horizontal plane. The initial displacements used in the experiments are 65 and 80 mm.

The structure experiences a mostly horizontal motion until it comes to rest. The vertical displacement due to the bending of the metal strip was measured to be up to 1.5 mm for an 65 mm initial displacement.

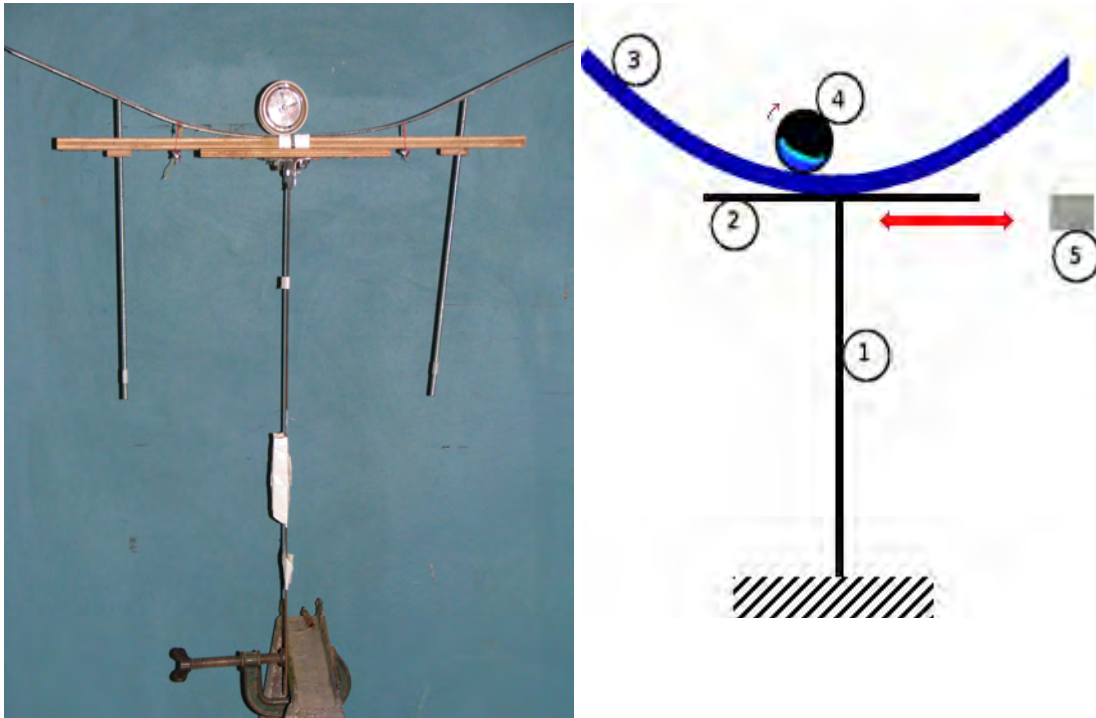


Figure 4.2: Showing (a) a photograph of experimental setup and (b) its schematic representation with cantilevered metal strip (1), platform (2), ramp (3), cylinder with particles (4) and bump stop (5).

4.3 Structural damping

The experimental critical damping ratio of the structure is estimated using the standard logarithmic decrement expression

$$2\pi\zeta = \frac{\ln\left(\frac{x_i}{x_{i+n}}\right)}{n}$$

where x_i and x_{i+n} are the first and last peak values, and n is the number of cycles and ζ is the resulting viscous critical damping ratio, assuming linear behaviour.

For an initial displacement of 6.5 cm the displacement history of the uncontrolled structure is shown in Figure 4.3. The uncontrolled structure has a natural frequency of 0.57 Hz and a very light critical damping ratio of $\zeta=0.001$.

The addition of the empty cylinder to the ramp, introduces a beat to the displacement history of the structure as shown in Figure 4.4. The beat indicates that the energy of the structure is transferred to the cylinder effectively. However, since there is no granular damping, the cylinder returns most of the energy and the structure retains its lightly damped characteristics. Naturally, the structure experiences greater damping with the presence of the cylinder, since the introduction of the cylinder dissipates energy in the form of contact friction.

The best results have been achieved at a fill level of just 1% of the volume of the cylinder. The structure's displacement history is shown in Figure 4.5 for this case. This configuration indicates 45% critical damping over 2 cycles (approximately 4 s). Although the validity of the logarithmic decrement expression is of question at such a high value of damping, it may still be meaningful as an indicator of performance. In Figure 4.5, the leftover oscillations, after about 4 s, are due to the imperfect tuning. At this point, the granular dissipation is so effective that the cylinder stops and simply acts as an added mass, rather than rolling and dissipating energy.

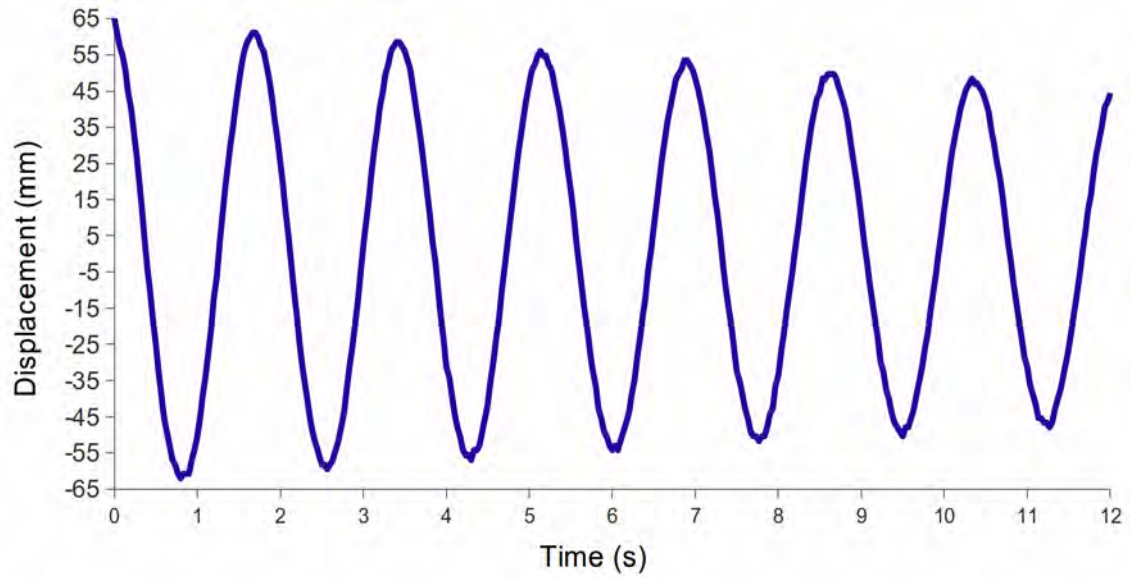


Figure 4.3: Displacement history of the uncontrolled damped structure, with an equivalent critical damping ratio of 0.1% . Initial displacement is 65 mm.

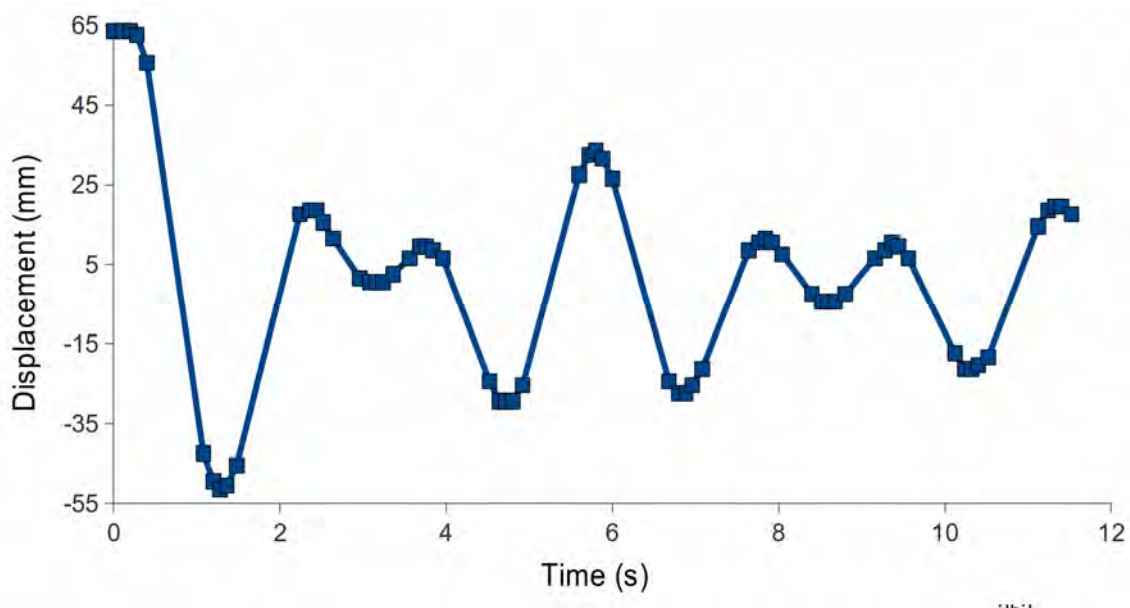


Figure 4.4: Displacement history of the structure with empty cylinder. The beat envelope indicates energy transfer to the cylinder which is then returned to the structure since there is no granular damper.

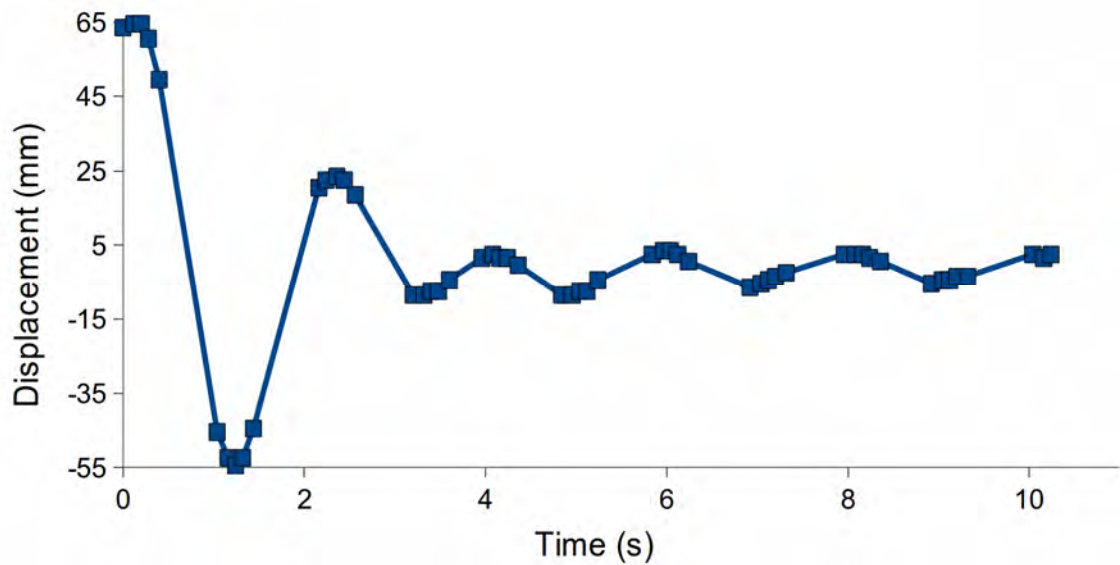


Figure 4.5: Displacement history of the structure with cylinder filled to 1% of its volume with sand as controller. Energy dissipation occurs quickly over the first two cycles. Remaining oscillations are due to imperfect tuning of structure and ramp/cylinder frequency.

A summary of the experimentally observed critical damping ratio for different fill levels is given in Figure 4.6. Fill levels below 1% also experience the beat shown in Figure 4.4 for the empty container. Hence, critical damping is reported for cases where the beat is not observed.

There are two lines in Figure 4.6, indicating the value of ζ when calculated from the positive (■) and the negative (◆) peaks of the structure's displacement histories. An additional data point was also tested which not shown in this figure. It corresponds to 4.8% fill, achieving about 10% critical damping, thus confirming the downward trend for critical damping with increasing fill level.

The 1% fill level is the smallest fill level where the beat is eliminated, producing the largest damping ratio of about 40% to 45%, depending upon

using either the positive or negative displacement peaks are used in logarithmic damping. As compared to the 0.1% critical damping of the uncontrolled structure, these values represent better than two orders of magnitude increase. Performance slowly deteriorates to about 25% damping when the fill level is doubled to 2%.

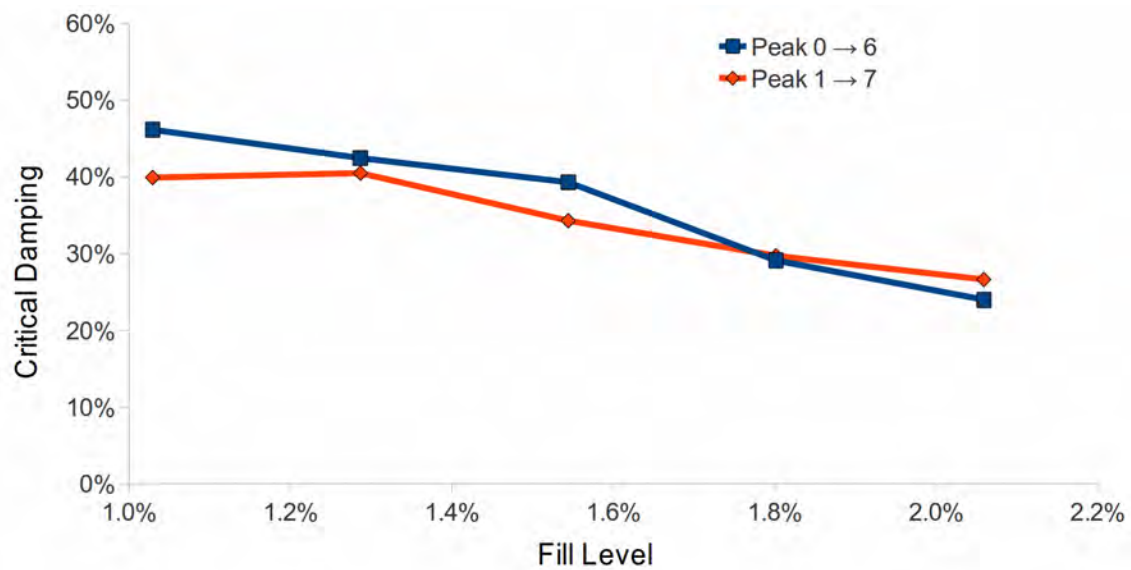


Figure 4.6: Variation of the critical damping ratio with fill level, over the first three cycles. Dark line represents the first six positive peaks, while light line represents the first six negative peaks.

There are two challenges to increasing the efficiency of the damper. The first is to transfer the energy from the structure to the cylinder - result of tuning. The second is to dissipate the energy in the shortest possible time - result of granular motion. In theory, if both of these can be maintained at all times, the controller can dissipate the harmful input energy completely. In practice, however, the effectiveness of the energy dissipation works against the overall control action. The granular material dissipates the energy presented to it too quickly, and prevents the rolling of the cylinder. Once the cylinder stops

rolling, structure reverts to its poor inherent damping with the added mass of the controller. Naturally, there is an upper limit to the maximum dissipation deliverable by the rotating container, which is dependent on the fill level, granular material and speed of rotation (as per Chapter 3 of this thesis).

4.4 Effect of tuning – change in radius of the ramp

In this section, observations are presented for different pendulum frequencies of the ramp. Three ramp configurations were tested, with three different radii. They were the tuned ramp (0.7 m radius), a smaller radius (0.5 m), and one with a larger radius (0.9 m). The radius of the ramp marginally affected the natural frequency of the structure, as shown in Figure 4.7. This is caused by the difference in the mass distributions at the top platform of the flexible structure. The smaller radius ramp (compact mass) coincided with a higher natural frequency.

As shown in Figure 4.8, the small-radius ramp (orange) and the tuned-ramp (blue) have similar critical damping values. Both have peak critical damping ratio of over 40%. The peak dissipation for the small-radius ramp occurs at a higher fill level (1.3%) than the tuned ramp (1%). This trend also carries over for the large diameter ramp where peak damping occurs at 1.8% fill level. Large-radius ramp has its best damping ratio of about 20% of the critical. However, this design is forgiving, allowing similar critical damping percentage over a large range of fill levels.

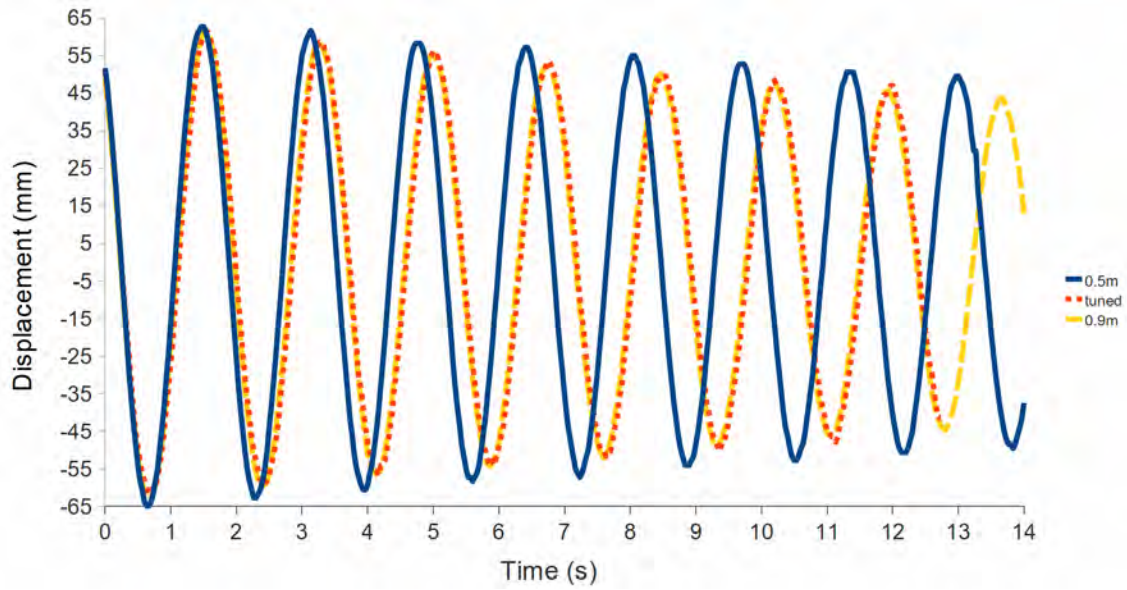


Figure 4.7: Natural frequency changes with ramp configuration. Natural frequencies of structure with larger diameter ramps are similar, while natural frequency for structure with small diameter ramp is clearly higher.

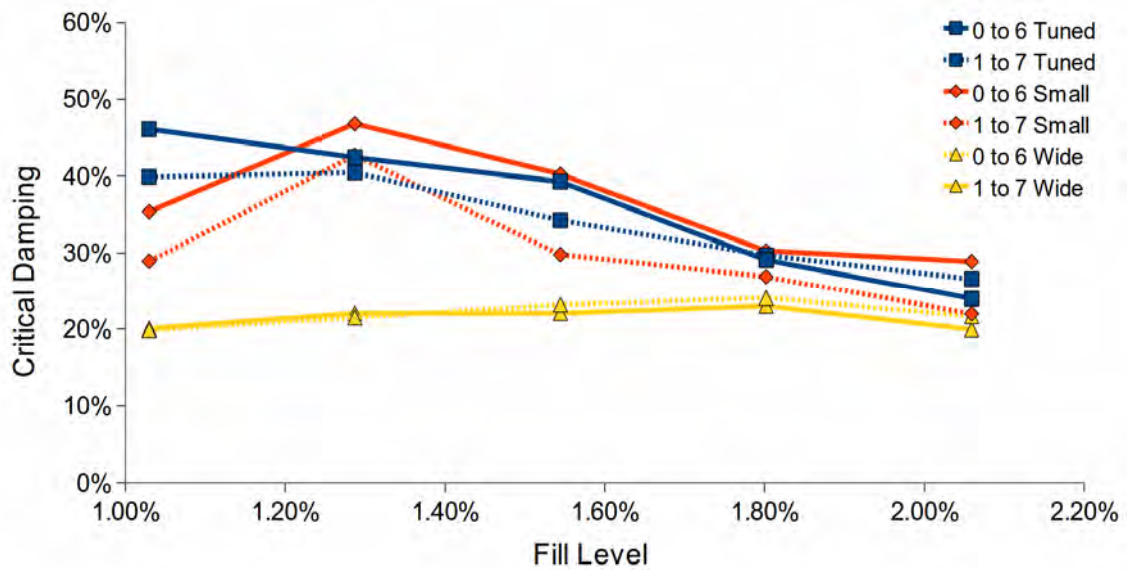


Figure 4.8: Critical damping plotted against cylinder fill level for three ramp configurations over the first three cycles. Solid lines represent the positive peaks while dotted lines represent negative peaks.

A closer look at the structure's displacement histories for the 1% (Figure 4.9 (a)) and 1.3% (Figure 4.9 (b)) fill levels, suggests that the tuned ramp is still the best dissipater in absolute sense. This is because once the granular damper is introduced, the period of oscillations for the tuned-ramp is shorter than that for the small-radius ramp. Hence, although the critical damping values are comparable, the tuned case stops over a shorter time, as shown in Figure 4.9 (b). A comparison for the highest critical damping, shown in Figure 4.9 (c) shows that the tuned ramp is clearly the best dissipater, effectively stopping the structure in 4 seconds compared to the 5 seconds for the 1.3% fill level of the smaller-radius ramp. In Figure 4.9, only the peak values were recorded from the videos, in order to save time. Such a presentation is valid, since the argument only relates the change in peak displacements.

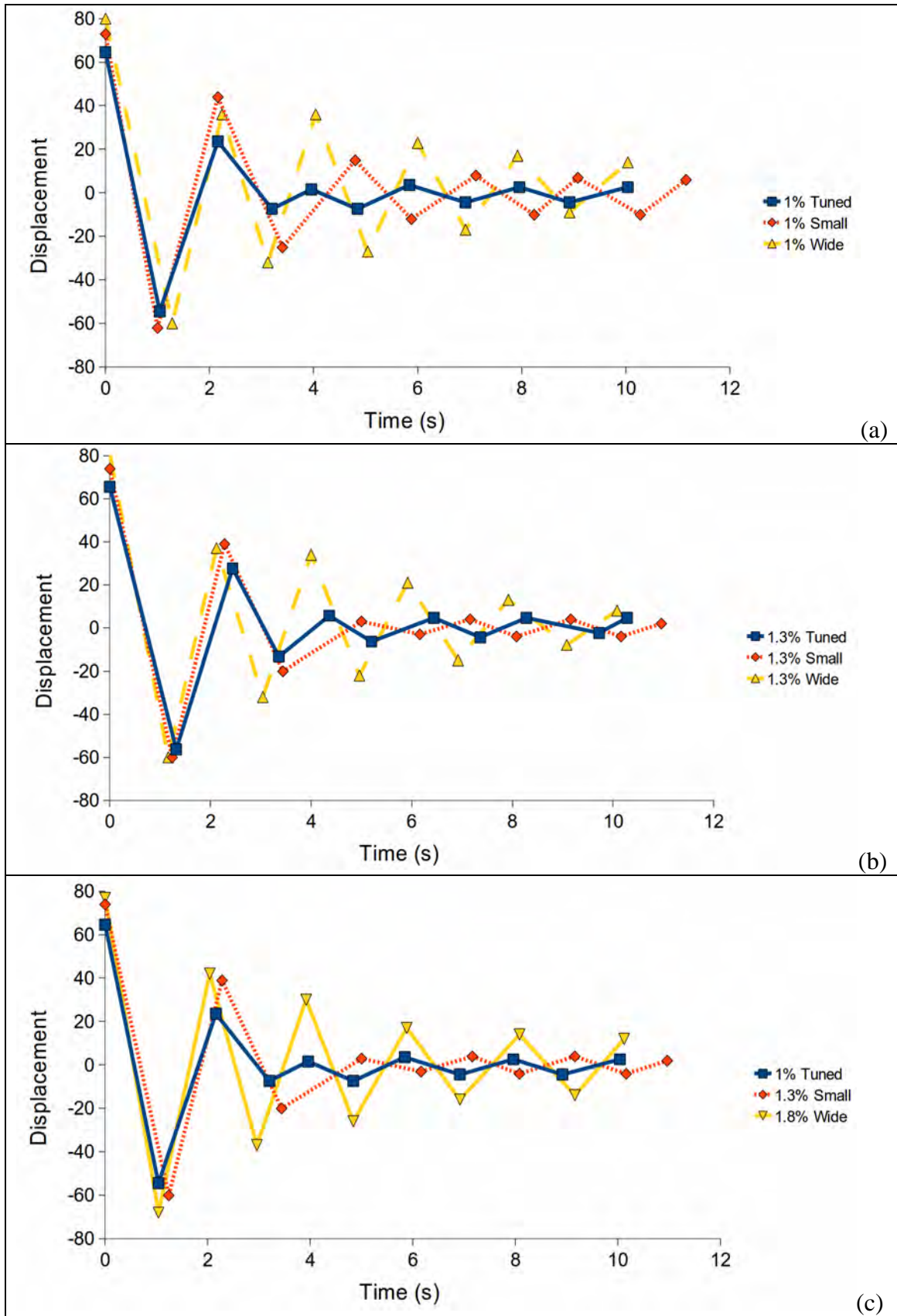


Figure 4.9: Displacement histories for (a) 1 % fill level, (b) 1.3 % fill level and (c) best tuned level for each case.

4.5 Effect of initial displacement

In the experiments, the initial displacement of the structure represents the input potential energy which needs to be dissipated. Therefore, in order to observe the robustness of the design to input energy above the design parameters, an initial displacement of 8cm is also tested. Larger initial displacements were not possible due to limitations of the experimental setup.

For this case, the absorber performance is plotted against fill level in Figure 4.10 over the first (blue), second (red) and third (yellow) cycles. Similar to the 6.5cm displacement case, the beat disappears at fill levels above 1%. The highest dissipation, 46% critical damping over three cycles, occurs at 2.2%.

For some of the cycles there is a fluctuating behaviour that increases with fill level. This is due to increase in the underlying beat that occurs for these fill levels. The beat is the effect of the imperfect tuning of the natural frequency of the structure to the ramp.

The overall behaviour for different fill levels is quite different than the earlier observations for 6.5 cm initial displacement which was a slow deterioration for higher fill levels. The damping ratio seems to improve until 1.8% fill level, followed by a consistent drop at 2.1 %, and a recovery afterwards. However, the performance of the controller is quite comparable to earlier experiments at this higher initial displacement, as shown in Figure 4.11. In this figure, the best dissipation cases are compared for the 6.5cm and the 8cm cases. While they do not occur at the same fill level, they dissipate most of the energy over three cycles (6 to 7 seconds). It is interesting to note that the tuning is not affected by the increase in initial energy, and there are practically no remaining oscillations for both cases.

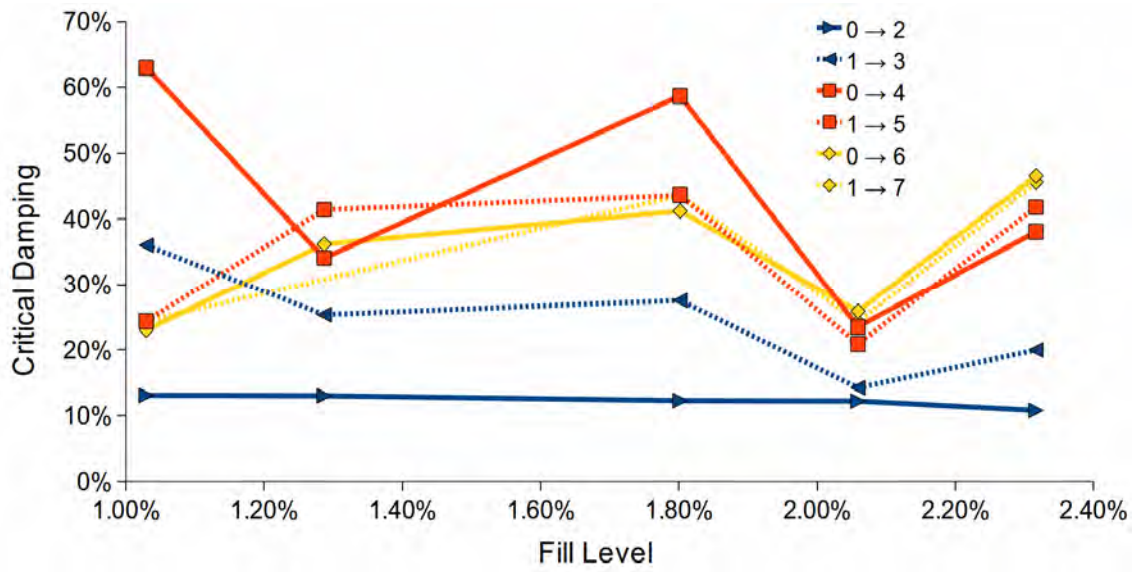


Figure 4.10: Variation of the critical damping ratio with fill level, calculated over one, two and three cycles. Solid lines represent the positive peaks while dotted lines represent the negative peaks. Lighter colors indicate greater number of cycles.

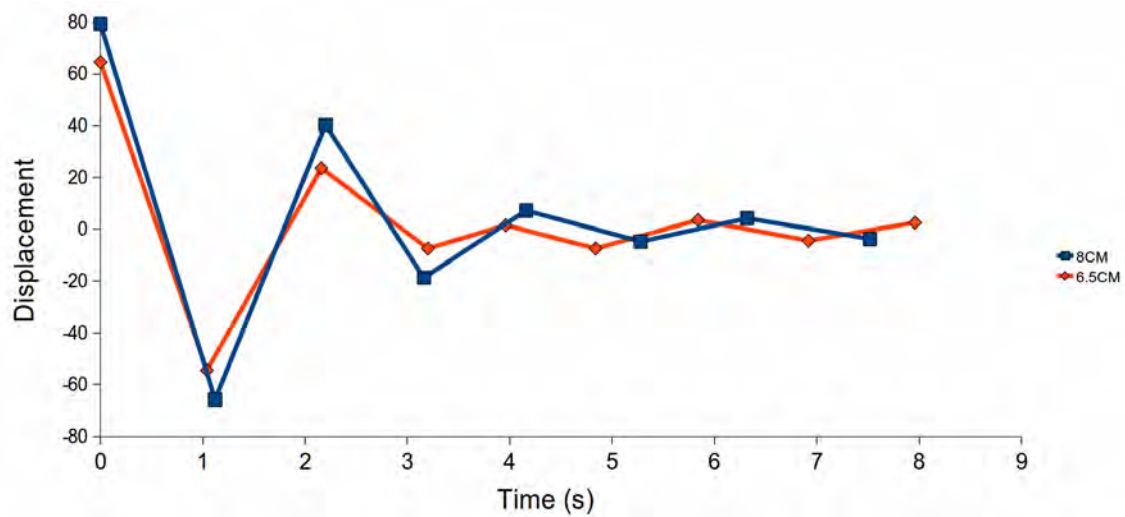


Figure 4.11: Displacement histories for the 6.5 cm and 8 cm initial displacements. Fill level is 2.3% for 8cm and 1.3% for 6.5cm.

4.6 Conclusions

Tall, flexible structures can suffer excessive oscillations when they are under wind, earthquake or shock loading. An experiment which replicates such a load has shown that a granular sloshing absorber is a suitable vibration damper for this kind of building. The importance of tuning the ramp diameter to the structure's natural frequency in order to completely stop the motion has also been shown.

The absorber has high efficiency, in the order of 40 to 50% critical damping despite a small added mass of around 1%. This occurs at very low fill levels of the cylinder of between 1% and 2%. Higher fill levels quickly lose efficiency, and mostly act as an added mass to the structure.

Tuning, by matching the natural frequency of the structure to the pendulum frequency of the absorber, is essential to the transfer of the harmful energy from the structure to the container, and to limiting remaining oscillations. A ramp radius larger than the tuned case (by about 30%) has lower efficiency, but shows a wider range of effective fill levels.

For the tuned case, the design is shown to remain effective even when the energy input is increased over the design parameters. However, peak efficiency is then achieved at higher fill levels than the optimum case.

The absorber is a very promising design for a structural damper. The design has shown to be effective at absorbing harmful energy away from a structure at an experimental scale. It was shown to be very effective with a very low added mass, easy to tune for the structure to be controller and quite forgiving when input energy is greater than design energy. As such, large scale structure

modelling should be done using a numerical tool to check that the design works when attached to a real structure.

5 Energy dissipation characteristics of a granular flow damper

5.1 Introduction

Tall structures require protection from transient forces such as those due to wind and earthquakes, for both structural safety and the comfort of the inhabitants. A variety of tuned mass dampers (TMD) are used to attenuate the excessive oscillations of such buildings. TMDs consist of a mechanism to transfer energy away from the structure (ensured by a tuning process) and dissipative elements. One such design of the authors uses a cylindrical container partially filled with a granular material which interacts with the structure through a circular track, as shown in Figure 2.1 from Chapter 2.

The efficiency of this design has been shown experimentally in Chapters 2 through 4 and numerically in Chapters 2 and 3. The motion of the structure causes the cylinder to roll leading to energy transfer between the structure and container. The granular material inside the container experiences collisions with the boundary of the container and among its particles, resulting in energy dissipation.

Particle-based numerical models are well suited to granular-flow devices since they are able to track the motion of each individual particle and its interactions. The Discrete Element Method (DEM) is a particle-based method which has been thoroughly reviewed (Campbell 2006), (Barker 1994) and (Walton 1992). A DEM granular solver developed by CSIRO is used here which has been successfully applied earlier to a wide range of applications

from mining to pharmaceuticals, see (Cleary 1998, 2001) and (Sinnott et al. 2006) for examples.

The use of a dynamic model enables the simulation of granular sloshing absorbers without the need for experiments to define the motion of the device. A dynamic model allows the particle flow to modify the cylinder's motion and more physically predict the particle flow field, forces, and mechanisms of effective energy dissipation. Such predictions are essential to enhance the effectiveness of structure control and for implementing such devices on practical problem structures.

This chapter deals with a fully dynamic model of the cylinder rolling down a ramp with a no-slip condition at the ramp-cylinder interface. The basis of comparison is the specified motion case which yielded a good match of particle kinematics between the experiment and simulations (Dragomir et al. 2009). This chapter also lays the groundwork for the changes required to the DEM solver which would allow the prediction of a fully dynamic system where the damper and a structure interact, and the damper dissipates the system's energy.

5.2 Discrete Element Method – dynamic object

The standard DEM solver presented in Chapter 2 forms the basis of the numerical solver. This model is extended in order to allow the motion of a cylinder on a ramp. The capabilities are as follows:

- Motion is possible up or down an inclined ramp; the ramp need not be linear

- Motion accounts for gravitational forces acting on cylinder and particles
- Motion accounts for moments of inertia acting on the cylinder and particles

For the simulations presented here, there is no contact detection between different boundary objects such as the cylinder and the ramp. Thus the cylinder's path is constrained to follow the ramp, with one point of the cylinder always being in contact with one point of the ramp. This is achieved by discretising the curved ramp into a piecewise linear representation which then becomes an assembly of linear segments that are input into the DEM solver as a sequence of horizontal positions and ramp angles. The ramp profile used is a 6th-order polynomial curve of best fit through measured coordinates on the real ramp. The cylinder object is constrained to follow the path of the ramp surface with a no-slip condition. At each time step the forces on the cylinder are calculated as the sum of the forces acting on the cylinder due to external and internal forces. The external forces are due to gravity for the current angle of the ramp, θ . The internal forces are due to particles acting on the internal cylinder boundary, represented by F_x , F_y and T_z . The total acceleration acting on the cylinder at each position in a direction parallel to the ramp at that position is given by:

$$ROTACC = \frac{1}{2}g \sin \theta + \frac{1}{2}F_x \frac{\cos \theta}{m} + \frac{1}{2}F_y \frac{\sin \theta}{m} + \frac{1}{2} \frac{T_z}{mr} \quad (5.1)$$

where m is the cylinder mass, r is the cylinder radius, F_x , F_y and T_z are the forces and the torque due to the particles acting on the cylinder. The forces and their directions are shown in Figure 5.1.

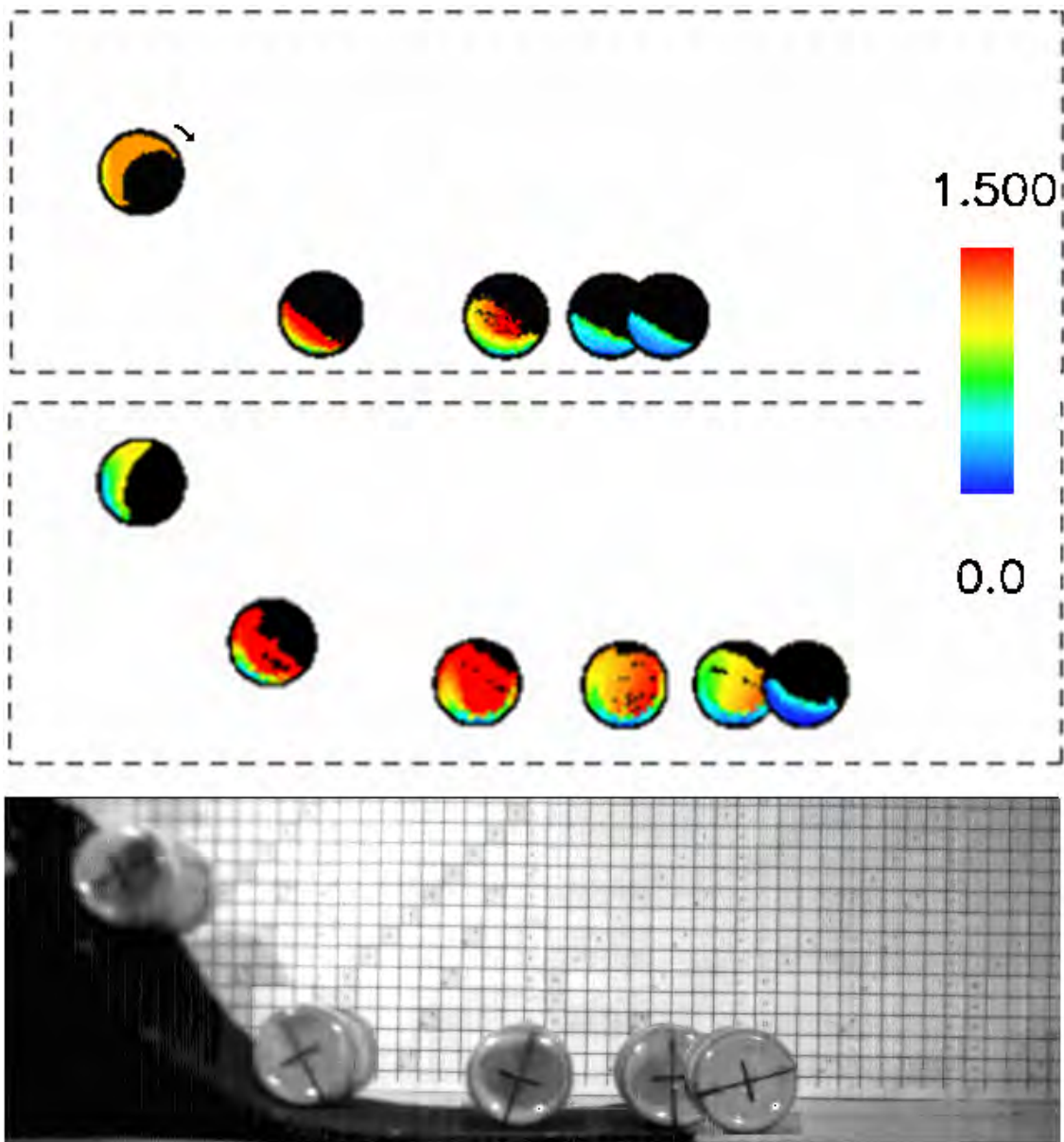


Figure 5.2: Motion of cylinder down ramp for specified case (top), dynamic model (middle) and for experiment (bottom).

The stopping distance for the container is completely defined in the specified motion case describing the position on the level plane of the ramp where the container in the experiments came to a complete stop. This distance is a measure of the total energy dissipated in the system. The stopping distance is dynamically predicted in the dynamic motion case, as a result of how much energy is dissipated in the container due to particle flow.

The container positions in both the horizontal and vertical directions are shown in Figure 5.3 for the dynamic and specified motion simulations. From this, we can see that the stopping distance in the dynamic motion prediction is over-estimated from the experiments by about 7%. The total distance travelled along the vertical axis differs by 2 cm, which corresponds to a ramp error of approximately 8%. This discrepancy may be attributable to one of three potential sources of error: 1) measurement error in the process of measuring and digitising the ramp profile; 2) incorrect material specification for the particles (we have not yet investigated the sensitivity of the coupled particle-container motion to material properties and it is quite possible that these are not correct); and 3) potential slip between the container and ramp in the experiments.

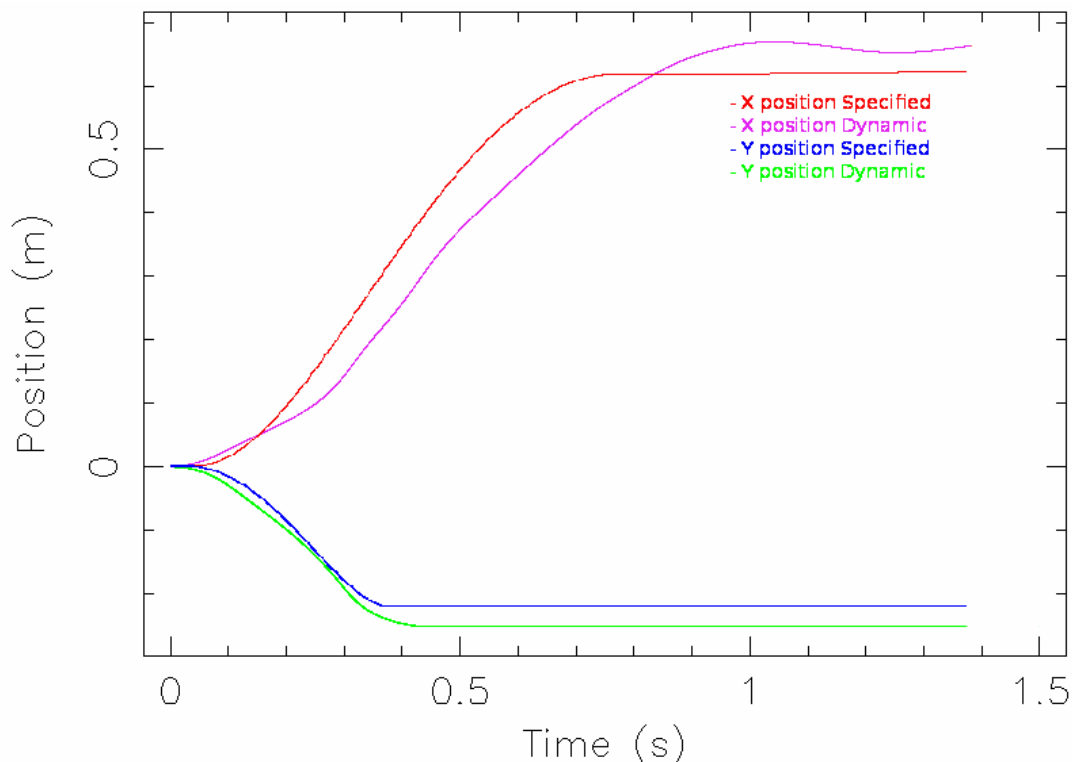


Figure 5.3: Histories of the container x and y position for the specified and dynamic motion cases.

Despite the errors, the predictions from the dynamic motion case are in very good agreement with that determined from experiment and imposed in the specified case.

The container speed is tracked by the solver for the specified and dynamic motion cases as shown in Figure 5.4. Here, the step-wise discontinuous history corresponds to the specified motion measured at regular intervals throughout the experiment. The overall shape of the motion of the dynamic model and the specified motion model, is quite similar.

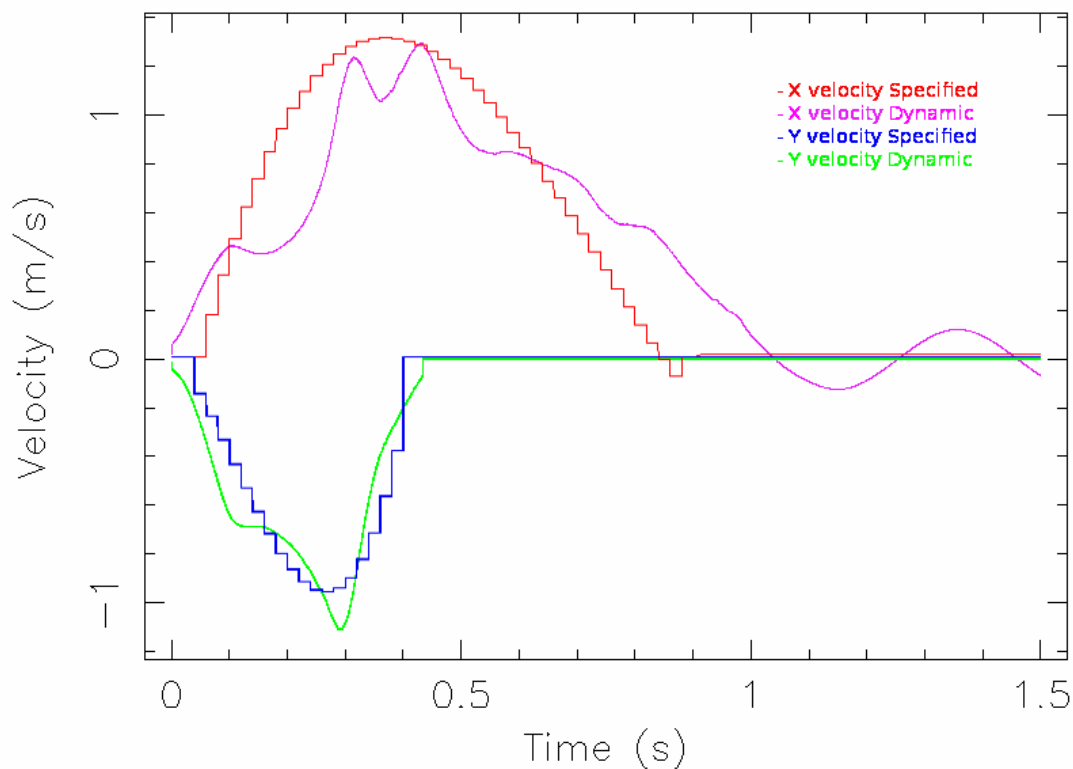


Figure 5.4: Histories of the container x and y velocity for the specified and dynamic motion cases.

There are, however, fluctuations in the dynamic model case which are discussed in the following section. Finally, the angular speed of the rolling container is shown in Figure 5.5. The trends closely follow those in Figure 5.4 since the linear and angular motions are fully coupled due to the no-slip condition in the dynamic motion case.

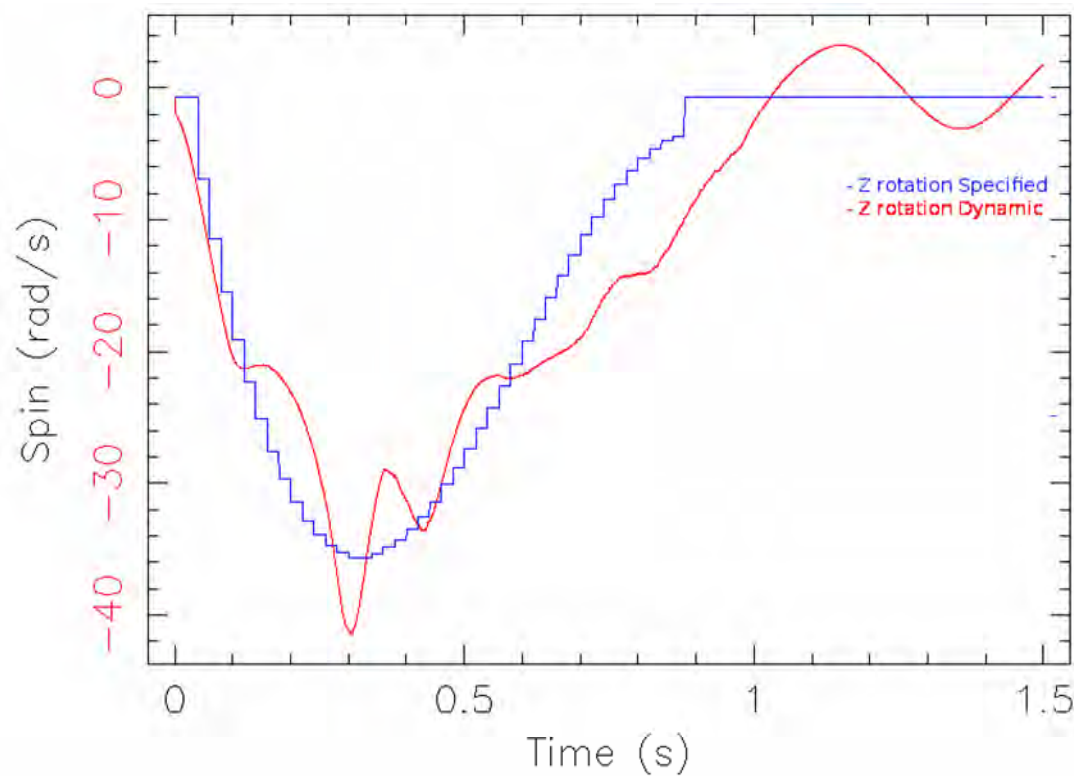


Figure 5.5: History of the container angular speed for the specified and dynamic motion cases.

5.4 Energy Dissipation Events

It has been noted earlier that three distinct events, associated with cataracting particle flow, can be identified for the case given in Figure 5.2 (Dragomir et al. 2009). These are marked as (1), (2) and (3) in Figure 5.6 which shows the input power to the container due to torque exerted on the container by the particles. The black line corresponds to the specified motion case, while the

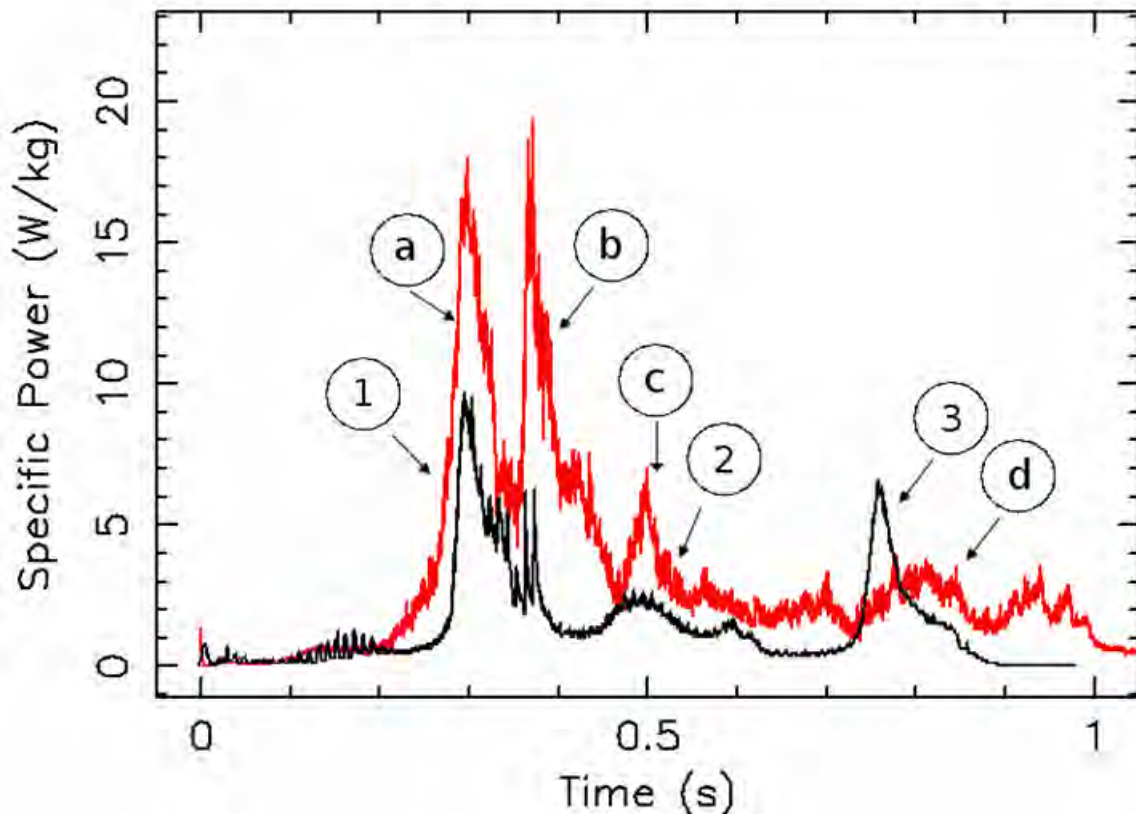


Figure 5.6: History of the input power to the system due to the particle torque on the container boundary for the dynamic case (red) and the specified case (black).

red line corresponds to the dynamic motion case in this figure. There is substantial difference in the power between the 2 cases. The dynamic case appears to experience greater torque on the boundary which indicates that the behaviour of the particle flow and the forces exerted onto the container are different for the specified and dynamic motion cases. The dynamic case predicts four dissipative (high power) events, marked as (a), (b), (c) and (d), and these occur at roughly the same times as in the specified simulation.

Event (3) for the specified case has a much higher magnitude than the corresponding event (d) for the dynamic case. This is due to abruptly stopping the container in the specified case.

The dynamic case requires a longer stopping time as the particles have to dissipate the residual energy through collisions, after the level portion is reached. This difference in the residual energy can be attributed to the surface on which the experiment was performed which could not be guaranteed to be non-slip, dissipating some energy at the contact point between the container and the ramp surface.

The fluctuating motion experienced by the container in the dynamic model seen in Figure 5.4 and 5.5 is clearly the effect of the 2-way communication between the particles and the cylinder. For the case of the vertical motion, there is an increase in speed as the container descends the ramp. The effect of the particle motion on the container is easily observed for the dynamic case. Events (a) and (b) in Figure 5.6 describe sloshing events with the container accelerating, decelerating and then accelerating again (see Figure 5.4) in response to the internal flow. For the specified case, there is only a single event (1) as the cylinder does not move in response to this flow and therefore damps out the sloshing motion. These events dissipate energy and there is a clear relationship between the power peaks and the structure of the velocity profiles in Figure 5.4 and 5.5.

During the development of the dynamic model, one very important factor on stopping distance, particle kinematics and overall energy in the system has become obvious. It is very important that the ramp geometry is accurately represented as the boundary condition for the rolling container. Some of the unexplained differences in the particle kinematics will be due to the inability to best measure and represent the real ramp by a polynomial curve. This point is currently under development to avoid such difficulties.

5.5 Conclusions

This chapter shows that, while a specified-motion simulation can accurately predict the particle kinematics, a dynamic model can offer additional insight into the workings of the flow for a cylindrical rotating container partially filled with a granular material. The dynamic case describes aspects of the container motion not easily observable from the experiment. These have been shown to be related to structure in the input power (and internal dissipation) in this system. The dynamic model thus offers a better tool for understanding the dissipation mechanisms of this complex system.

Presented work should be interpreted as a qualitative assessment of the numerical prediction tool. A relatively close prediction of the true stopping distance is an encouraging result and indicates the potential of the model as a powerful design tool for practical implementation.

6 Conclusion

The objective of the work presented in this thesis is to investigate the design of a new vibration damper for structural control. The damper is composed of a ramp rigidly attached to the structure, a cylinder and some granular material. The radius of the ramp and that of the cylinder provide a tuning option which can be adjusted to the structure's natural frequency. The granular material provides the energy sink, through the particle collisions and friction with each other and with the cylinder walls.

The feasibility of using particle flows as an energy sink is investigated in Chapter 2 through simple experiments. Sand is found to be an effective material for this purpose since individual grains are quite dense. The particle fill level is found to be very important to efficiency of energy dissipation. A numerical model using the Discrete Element Method is shown to provide a good kinematic match for the particle motion in the experiment. From the numerical model there are three distinct dissipation events which coincide with flow events. The model also shows that the primary means of energy dissipation in the system are the shearing layers when the particles flow in an avalanching regime. The cataracting stream collapse also accounts for a significant amount of energy dissipation.

The granular material properties which affect maximum dissipation for a rotating cylinder are investigated in Chapter 3. It is found that energy dissipation increases linearly with the speed of rotation, until the material centrifuges, when all dissipation virtually stops. The energy dissipation is also found to increase almost linearly with fill level for levels between 5 and 15%. For fill levels under 20%, the

existing standard model grossly underestimates the speed at which centrifuging occurs. Hence, alternative models are found and extended upon. The DEM solver is tested against the empirical results and is found to marginally over-estimate centrifuging speeds.

With the help of the numerical tool, the effect of material properties such as density, coefficients of friction and restitutions on centrifuging speeds is checked. Higher coefficient of friction leads to lower centrifuging speed. Meanwhile, material density and coefficient of restitution are found not to affect centrifuging speed at all.

The conclusions drawn from the Chapters 2 and 3 are tested at a lab scale in Chapter 4. The structure is represented by a metal strip clamped to a stand, with a circular ramp attached. The absorber shows very high efficiency of about 50% critical damping over three cycles of the structure. The added mass of the cylinder and granular material is low (less than 1%), and the fill level is also very low (between 1 and 2%). Tuning is found to be critical to completely removing all oscillations from the structure. These results are very promising and should be followed up with real life scale numerical simulations in order to test a variety of design options.

The conclusions about the best dissipater in Chapter 4 appears to stand at odds with findings from Chapter 2, where the peak dissipation efficiency was found to occur at between 5 and 15% volumetric fill level. However, this discrepancy can be explained through the input energy. In Chapter 4, there is limited energy input, set by the initial displacement of the experimental apparatus, while in Chapter 2, the energy input is driven by an electric motor and limited only by the

duration of the experiment. Furthermore, the particle flow in Chapter 2 is fully developed, and energy dissipation is driven by shear, while in Chapter 4 there is limited particle flow due to the lack of additional energy input after the experiment has started, and dissipation is driven by surface friction between the container and the ramp.

The numerical model is expanded in Chapter 5, in order to allow a two-way communication between the material and the container. This allows free roll of the container down a ramp similar to what was used in Chapter 2, where the sand actually dissipates the potential energy of the system and stops the container. Stopping distances are found to be nearly identical for the experiment and the numerical simulations. Energy dissipation events are similar to the results obtained in Chapter 2, where the motion of the container was specified.

Further work on the numerical model are underway and focused on obtaining two-way communication between the container and the ramp, as well as the structure on which the ramp is attached. This would allow the researchers to test the granular sloshing absorber performance against real earthquakes acting on real structures. A further benefit of a reliable numerical model would be to study the issue of scaling the control performance.

1. Introduction

Sloshing refers to the low frequency oscillation of the free surface of a liquid in a partially full container. Intentionally induced sloshing is employed in tuned sloshing absorbers which can provide benefits similar to that of a tuned vibration absorber for structural vibration control. A brief treatment of such devices is included in Appendix B, for completeness.

Liquid sloshing absorbers are low maintenance components. They have found use in flexible structures, such as towers and suspension bridges under wind and earthquake loading. One of the challenges in the design of sloshing absorbers is to provide fast energy dissipation, once a strong interaction is established between the sloshing liquid and the structure to be controlled. This report details an experimental investigation in which granulated solids are used, instead of liquid, in a sloshing absorber.

A schematic representation of such an absorber is given in Figure A1. In this figure, the curved surface is attached to the structure to be controller. The round dissipative element contains granular particles which are free to move and dissipate energy. The current experimental work has been to characterize the mechanism of energy dissipation. The idea here is similar to that of a damped tuned vibration absorber described in Appendix B.

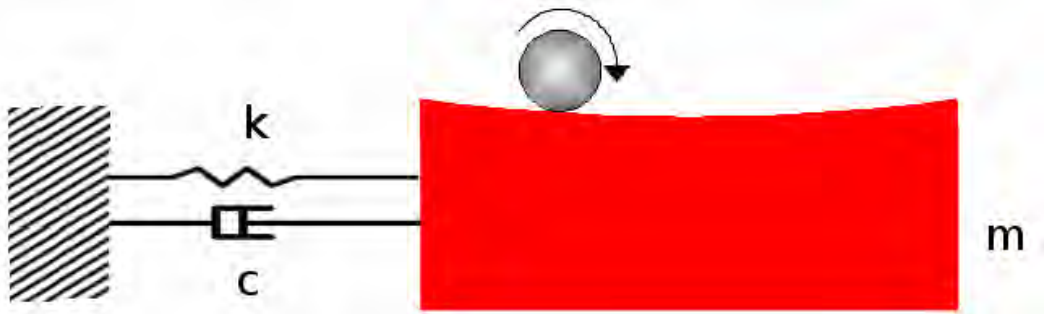


Figure A1. Schematic representation of a design for proposed granular sloshing absorber.

Dampers using granular materials exist in the literature in the form of impact dampers. Impact dampers are mass dampers which use plastic collisions and momentum transfer between the damper, a loose mass, and its boundaries which are attached to a primary vibrating system to be controlled (Papalou et al 1996). Because significant impact forces are employed in absorbing vibrations, rapid deterioration of materials may occur. Papalou and Masri propose the use of a damper with multiple particles, to reduce such maintenance problems. The concept of particle damping involves the use of powders or particles of small diameter inside enclosures that are part of a vibrating structure (Xu et al 2000). The dissipative forces are a combination of collision, friction and shear damping (Panossian 1991, 1992).

Numerical models for granular particle interactions can be classified in two groups (Yoon et al 1999): those based on Lagrangian methods, such as Smoothed Particle Hydrodynamics (SPH) (Monaghan 1988, Benz 1989, Iglesias et al 2006), Discrete Element Method (DEM) (Mao et al 2004), attraction repulsion (Greenspan 2005), Moving-Particle Semi-implicit (MPS) (Yoon et al 1999, Koshizuka et al 1995, 1997), and those based on Eulerian methods such as Navier Stokes solution algorithms (Batina 1993) and element free Galerkin (EFG) (Panossian, 1991). Some of these, particularly

the Discrete Element Method, have merit to closely approximate the dynamics of interacting discrete particles.

While there are dampers which utilise granular particles, their methods of utilization are different from what is proposed in this document. No other research exists in the literature which utilises a sloshing absorber using granular materials in place of a liquid. The preliminary investigations show clearly that with a damper which uses sloshing particles in a container, it is possible to achieve effective energy dissipation.

Granular materials flow, like a liquid, when their container experiences an excitation. The objective of this research is to investigate an effective measure to suppress excessive vibrations of resonant structures. To this end, a modified sloshing absorber using granular materials is introduced, whose design characteristics define the scope of this research. In the following, experimental details are discussed first. Subsequently, the experimental observations together with their interpretation are presented. Appendix A includes brief descriptions of damped and undamped tuned vibration absorbers and tuned liquid dampers, for completeness.

2. Experimental Setup

Experiments consisted of freely allowing a cylindrical container to roll down a ramp from a known height onto a surface. The enclosure contained different numbers of particles for each experimental run. The effect of various variables has been explored, namely, container dimensions, particle dimensions, particle roughness (coefficient of friction per unit area), roughness of surface, enforcement of perfect roll on the ramp, ramp height, ramp inclination angle.

Experiments consisted of dissipating a known potential energy given to a cylindrical container through the induced relative motion of granular solids in the container. The particles have geometries ranging from irregular (beans and sand) to 3D discs (lentils). Releasing a container from a pre-determined height ensures consistent starting incident potential energy, whereas the distance the container stops rolling away from the release point is an indication of effective energy dissipation. The most effective dissipater stops the container motion over the shortest distance from release. This setup is described in Figures A2 (a) and A2 (b) in which the rolling surface, angle between surface and ramp, ramp, container and bump stop are shown. X represents the distance travelled. The dissipation of energy is the result of the ‘flow’ of granules, frictional dissipation due to the relative motion of granules, and collisions between particles and particles or enclosure’s walls. Although dissipation is frictional in nature, it may also be considered as ‘viscous dissipation’ in equivalent sense.

The motion of the container started from a complete rest at the point of release. As it lost altitude, it gained kinetic energy down the inclined ramp, both translating and rolling about its own centre. The bottom of the ramp represented the point where all the starting potential energy has been converted to kinetic energy. The rolling of the container continued some distance away from this location until its energy is dissipated by the flow of the granular material inside the container. At this point, the container came to a complete stop. The following paragraphs discuss the varying experimental parameters including the size of the container, amount and type of granular material and different inclined ramps.

The exploratory nature of the experiments led to the identification of important parameters and the subsequent comparison among their effects.

These parameters are container dimensions, particle dimensions, coefficient of friction of surface, coefficient of friction on the ramp surface and coefficient of friction amongst particles. For this reason, there are differences in experimental setup, equipment and procedures between the experiments. These differences are described in detail below.

2.1. The ramps

During this experiment, two ramps were used, in four different configurations, in order to determine the effect the ramp has on the experiments. The ramp length and height were measured with a standard measuring tape. The length of the ramp is the distance that the container can travel on the ramp. The angle between the ramp and the wedge was determined using trigonometry. The ramp drop is defined as the distance between the bottom of the ramp and the surface which the ramp leads to. The ramp properties are listed in Table A1.

Table A1 Ramp Properties

Ramp	Angle °	Height (m)	Drop (m)
1	18°	0.11	0.09
2	35°	0.2	0
3	15°	0.15	0
4	41°	0.23	0

Length measurements have an error margin of ± 0.5 cm. Consequently, angles determined have a margin of error of ± 1 °.

The first, second and fourth ramps have a stop at the start of the ramp as illustrated in Figure A2 (b) (item 5). Due to this restriction, the location at which the container touches the ramp surface is at a point 31.0 ± 1 cm from the bottom of the ramp.

2.2. The containers

In order to show that there is no dependence of the results on the container size, four different containers have been used during the experiments, with volumes ranging from 500 ml through to 1100 ml. The containers are translucent, cylindrical, and can be securely closed in a manner which does not affect their rotation. The container properties are presented in Table A2. During this experiment, Containers 3 and 4 are considered to be identical. Further, Container 1 has a support beam going through its centre, and the effect of this has not been fully investigated.

Table A2 Container Properties

Container	Name	Volume (l)	Height (m)	Width (m)	Mass (kg)
1	CD Holder	1.1	0.095	0.13	
2	Cable Tie holder	0.5	0.1	0.06	0.002
3	Water bottle	0.625	0.17	0.065	0.027
4	Water bottle	0.625	0.17	0.065	0.027

Experiment 1 was designed to determine the effect of container dimensions on the results. With this experiment, the effect of different ramps was also investigated. Particles are added to Container 1 in increments of 10 particles, up to 50 particles. Then, particles are added in increments of 50 particles. For each increment, the container is released from the ramp's bump stop, and allowed to roll until it comes to a complete stop. The distance travelled is measured, from the bottom of the ramp, to the point where the container touches the surface. This is considered one experimental run. The same procedure is repeated for the four combinations of the two variables, the ramp and container.

2.3. The Particles

The effect of particle size has been explored through the use of four particles. The effect of particle surface friction has been partially explored. The particle sizes have been measured with a ruler, and are listed in Table A3. A photograph to show visually what these figures mean is given in Figure A3.

Table A3 Particle properties

Particle	Density (kg/l)	Height (mm)	Width (mm)	Length (mm)
1 (lentil)	0.8	2.73	5.6	5.6
2 (soy bean)	0.75	6	8.23	16.03
3 (broad bean)	0.75	6.36	13.63	22.56
4 (sand)	1.65			

In Experiment 2, the effect of the particle size is explored. In order to show repeatability of the results, for each particle increment, Container 3 is released four times off Ramp 2, and all distances are recorded. Particles are added in Container 3 in increments of 50 ml. Particles 1, 2 and 3 are used for this experiment.

2.4. The Surfaces

The experiments were conducted on two surfaces, in order to investigate the effect of the friction force acting on the rolling container. The first surface used was carpet, which has a high coefficient of friction. The second surface used was hard wood polished floor. The procedure is identical to that in Experiment 2. Ramp 4 was used during the runs. Container 4 was filled with Particle 2, and rolled on two surfaces: polished floorboards and carpet, which were identified as readily available extremes of coefficients of friction per unit area.

2.5. Perfect roll and perfect slide

In Experiment 4, perfect sliding motion and perfect rolling motion are compared to determine their suitability as an energy sink. The first part of the experiment, 4a, was to investigate the effect of perfect sliding motion on the ramp and surface. This was approximated by attaching Container 3 to a toy car, with a mass of 12g. Ramp 3 was specifically designed to accommodate for the ground clearance constraints imposed by the vehicle. As the height of the ramp was different to the other experimental runs, the results for this experiment are shown through incident energy, which is approximated as the initial potential energy, mgh .

Perfect rolling motion was investigated in Experiment 4b, through the addition of a rubber mat to Ramp 4. Two lengths of mat were used in two sets of experiments, in order to determine the effect of the increased coefficient of friction. Ramp 4 was used in Experiment 4b, in conjunction with Particle 2. Both Experiments 4a and 4b were run on the same surface, the polished floor board.

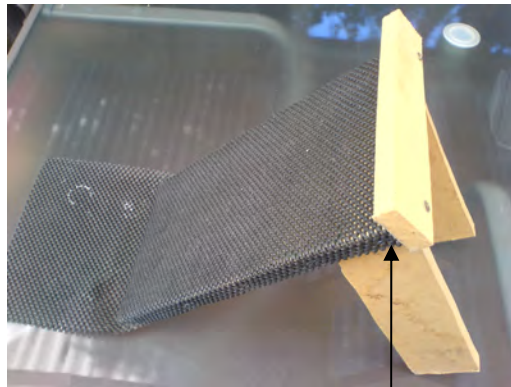
2.6. Increased internal friction

In Experiment 5, investigation of the effect of friction on the ramp has led to the investigation of the effect of increased friction inside the container, by using sand as a particle. However, sand has a much higher density compared to all other particles used during experiments and therefore, the results cannot be directly compared.

As a summary of this section, all experiments are listed in Table A4.

Table A4: Summary of experiments

Experiment	Purpose
1	Effect of container dimensions and ramp parameters on distance travelled.
2	Particle size influence on distance travelled.
3	Effect of surface friction on energy dissipation efficiency.
4	Comparison between perfect roll and perfect slide in energy dissipation.
5	Sand as a more efficient dissipater.



(1)Stop

Figure A2 (a). Ramp 3, with no-slip surface attached.

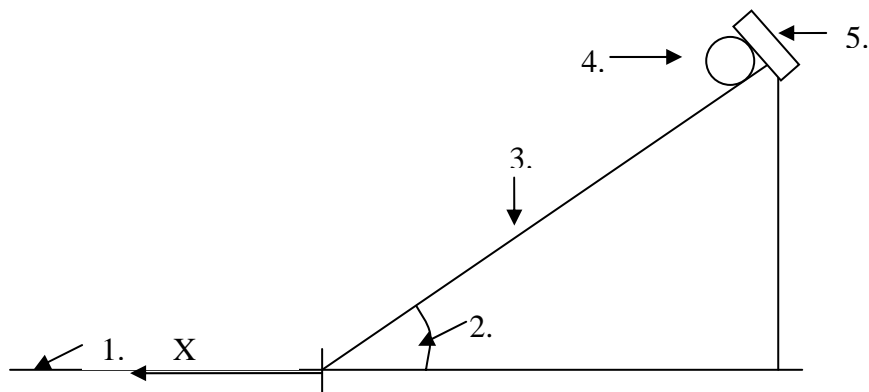


Figure A2 (b) Schematic of Experimental Setup. , showing (1) surface, (2) angle between wedge and surface, (3) wedge, (4) container and (5) bump stop. X represents distance travelled by container on surface.

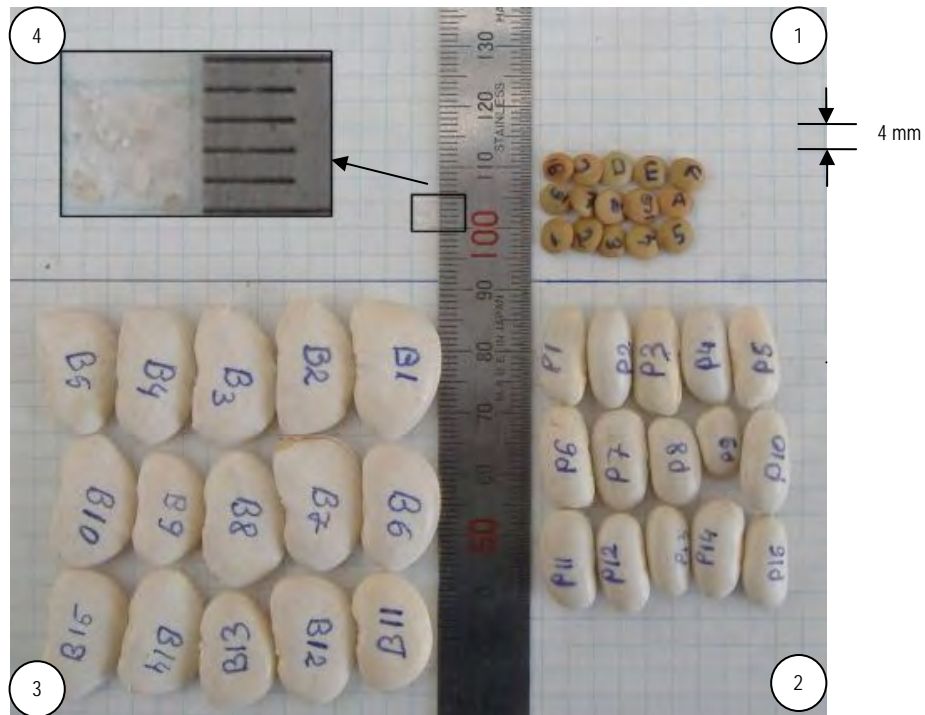


Figure A3. Depiction of 15 particles of each type. (1) lentils; (2) soy beans; (3) broad beans; (4) sand.

3. Experimental Observations

The experimental results are presented in this section in a chronological order.

In Figure A4 the results of Experiment 1 are given, where Containers 1 and 2 were rolled off Ramps 1 and 2. In this experiment the effect of container dimensions and the presence of a drop in the ramp were investigated. In Figure A4, \blacksquare denotes the combination ‘Container 1, Ramp 1’; \blacklozenge ‘Container 1, Ramp 2’; \blacklozenge ‘Container 2, Ramp 1’; and \blacktriangle ‘Container 2, Ramp 2’. In this figure, the vertical axis represents X, the distance travelled by the container from the bottom of the ramp until it came to a complete

rest, whereas 'Volume Fraction' is given on the horizontal axis indicating the fraction of the container being filled with particles.

Up to a 15% volume fraction, the distance decreases with increased number of particles. A relatively flat section follows the initial decreasing trend, until about 60%. A rapid increase in the distance travelled follows, up to the point where the container is completely full. This behaviour is observed for both containers, and both ramps. A simple observation from the trends is that, for Particle 2 (soy bean), the distance X is dependent on the volume fraction alone, regardless of container size, or the presence of ramp drop. By using Volume Fraction on the horizontal axis, the data points of different experiments with different numbers of particles are collapsed onto one line.

Observations with identical ramp setup, particles and surfaces are compared in Figure A5 for Containers 1, 2 and 3 (CD Holder, Cable Tie Holder and Water Bottle in order). The axes of Figure A5 are identical to those in Figure A4. By having the container size as the variable, it can be observed that container dimensions have no significant effect on the results, when the independent variable is chosen to be the non-dimensional volume fraction.

In Figure A6 the results of Experiment 2, are presented to show the effect of varying particle size. In the graph,  represents Lentil;  represents Bean; and  represents Broad Bean. The same axes representations are employed as in the previous figures. An approximately flat section is observed until the container is 50% full, after which a drastic increase in distance travelled occurs. The smallest particles have the shortest stopping distance while the vessel is less than 50% full. Meanwhile, larger particles are

show lower displacement for a greater range of volume fractions. Therefore, smaller sized particles are better dissipaters than larger particles.

In Figure A7, the results of Experiment 3 are shown, where the effect of the surface on which the container rolls is investigated. In this figure,  represents hard wood polished floor, which is considered a low friction surface; while  represents carpet which is considered a high friction surface. The measurements are performed in 50 ml increments and therefore, there are fewer data points per curve than in the previous experiments. The lines largely follow the same patterns shown in previous figures. The carpet, with high friction, shows a smoother curve, while the glass and polished floorboards show more variation between points. Experiment 3 clearly illustrates that the surface on which the container rolls affects the distance travelled. Not surprisingly, a rougher surface, with a higher coefficient of friction stops the rolling motion in a shorter distance. Such a surface also provides results with a smaller variance. In contrast, a smooth, low-friction surface is somewhat less effective in stopping the vessel's motion.

A high friction, damped surface shows more consistent results with lesser variation between data points than a low friction undamped surface. While this is an important discovery, it is unlikely to be used in an application of such an absorber for structural control, since the high friction damped surface would be subject to high maintenance costs.

One anomaly observed during this experiment has been the container sliding on the ramp, prior to, or in tandem with, the rolling motion. This observation and its influence on the results is what inspired the investigation between the perfect roll and perfect slide, Experiment 4. The sliding and

rolling motion on the container has been observed mainly at higher energy levels.

In Figure A8 the results of Experiment 4a are shown, the perfect slide ($\rightarrow\blacklozenge$) and 4b perfect roll ($\rightarrow\blacksquare$ and $\rightarrow\blacktriangle$), utilising the same axes as previous graphs. The results show that perfect sliding is an inefficient energy dissipation technique, which caused all further experiments in this direction to be ceased. In contrast, perfect roll is an efficient energy dissipater whose level of energy dissipation depends on the volume fraction. In Figure A9, the same data is the incident potential energy as the independent parameter which takes into consideration the added mass of the setup for the perfect slide. No change is observed between the two figures.

In Experiment 4b, the effect of perfect rolling of the container is further explored. Perfect rolling on the ramp and surface were encouraged through the use of rubber on the ramp and a section of the surface. In Figure A10, the three lines represent the results with no rubber on the ramp ($\rightarrow\blacktriangle$), a 50 cm length of rubber ($\rightarrow\blacklozenge$), and 90 cm length of rubber ($\rightarrow\blacksquare$), while all other variables remain unchanged.

When the container is less than 50% full, both lengths of rubber show remarkably better results. However, as the vessel fills further past 50%, the rubber on the ramp causes significantly further travel. The reason for this is that at higher energy levels, the absence of the rubber causes both translation and rotation while the container is on the ramp. The translation, or sliding, dissipates some of the energy of the container while still on the ramp. This effect is not considered to desirable as its presence adds uncertainty which cannot be predicted clearly. In Experiment 4b the efficiency of energy dissipation when the container is forced to roll on the

ramp is demonstrated. The case when the long rubber is attached to the ramp is marginally better while the container is under 50% full.

Despite the dry friction the sliding motion experiences, overall, perfect roll is the better energy dissipation method. Meanwhile, perfect sliding motion proved to be an inefficient dissipater.

In Figure A11 the performance of the previously used particles is compared to that of sand when the container is rolled on the ramp lined with rubber. Sand is a better energy dissipater at small volume fractions. However, as the volume fraction increases, the larger particles (beans) seem to produce better results.

In Figure A12 the same data is represented as Figure A11, however the energy in the system is shown along the horizontal axis. The data points for particle 4, sand, are shifted right, while those of particles 1 and 2 maintain their relative positions. This shift indicates that sand can dissipate more incident energy over the same distance travelled by the container.

As seen in Figure A12, sand is the most efficient energy dissipater, both in terms of stopping distance at low volumes and amount of initial energy dissipated. Due to the promising results, further investigation, which included video recordings of the experiments, was conducted. These visual observations are detailed in the following sections, together with drawn sketches of the motion of particles inside the container at 1/25 second intervals.

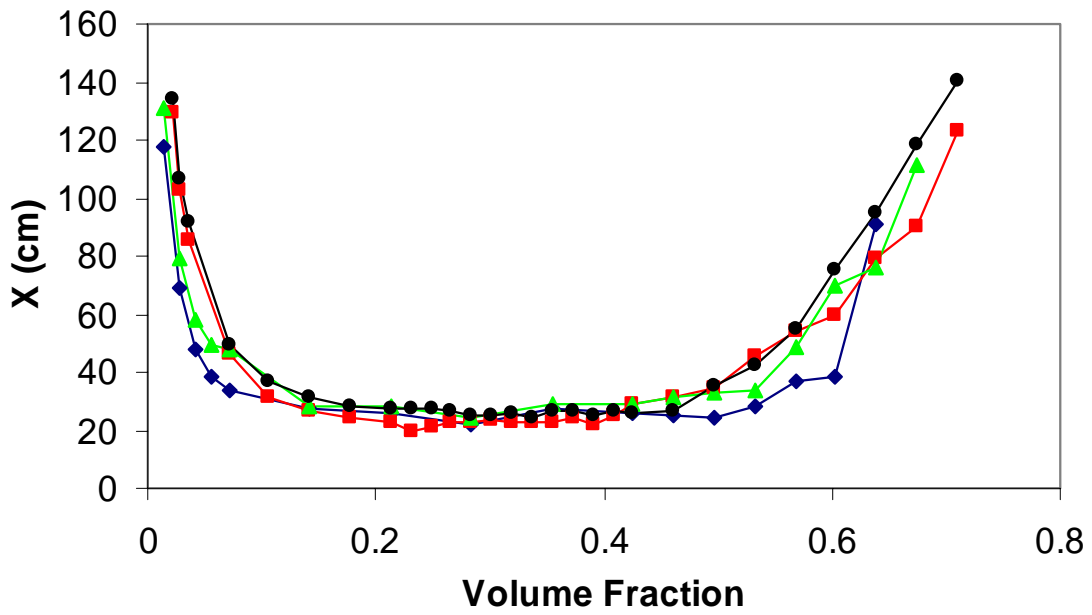


Figure A4. Effect of container and ramp. —■— Container 1, Ramp 1; —●— Container 1, Ramp 2; —◆— Container 2, Ramp 1; —▲— Container 2, Ramp 2. Vertical axis represents X, the distance travelled by the container. Horizontal axis represents the number of particles in the container, measured as a percentage of the container capacity. All experiments with Particle 2, on glass surface.

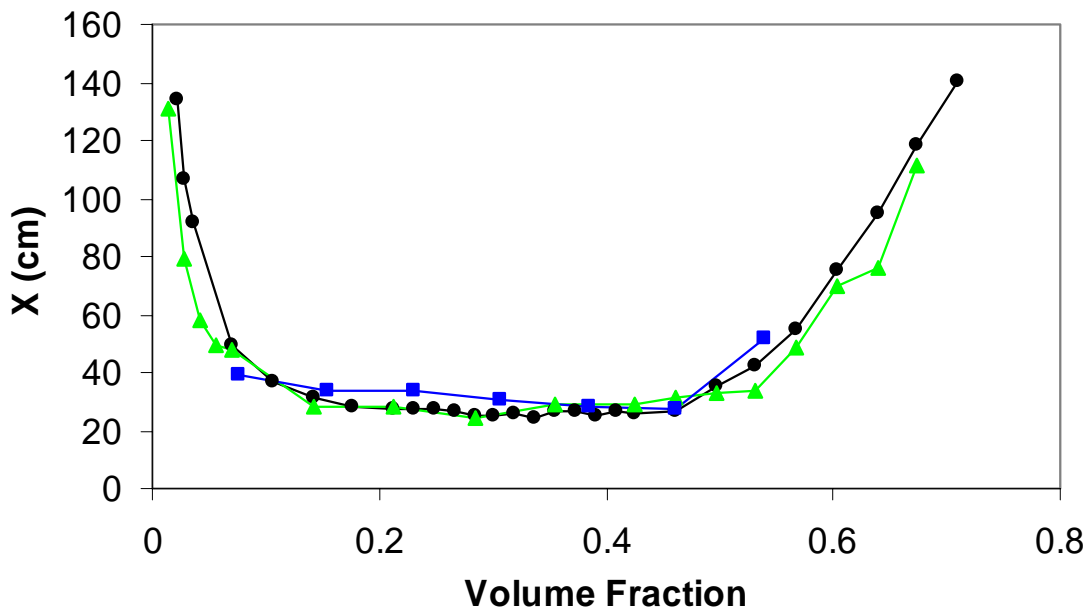


Figure A5. Effect of Containers 1, 2 and 3. —●— Container 1; —▲— Container 2; —■— Container 3. All experiments with Ramp 2, Particle 2 on glass surface. Axes are the same as in Figure A4.

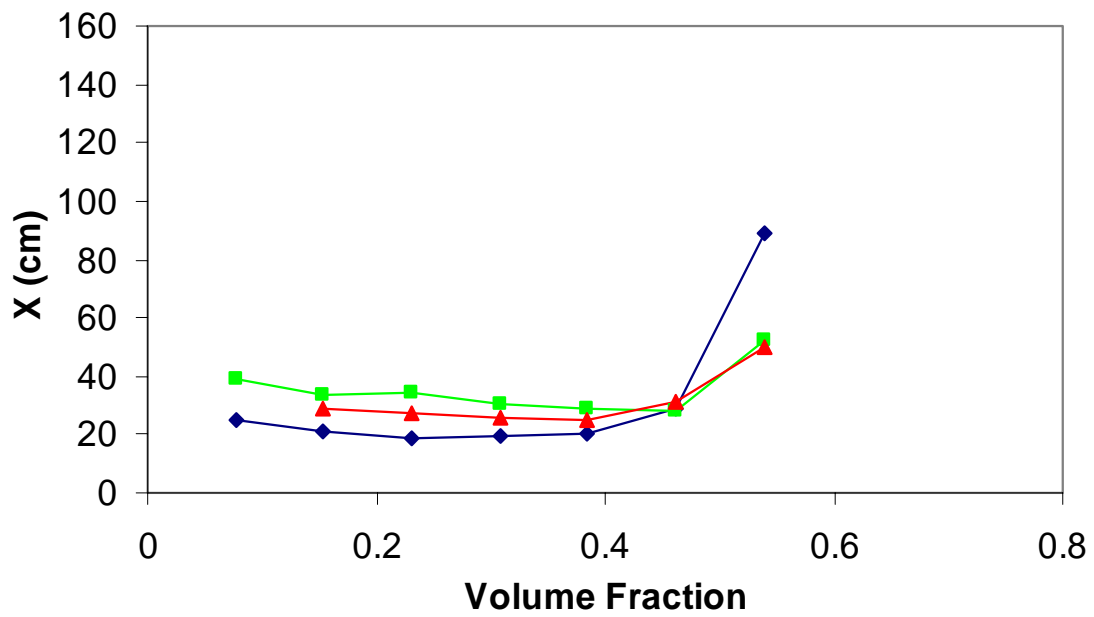


Figure A6. Effect of Particles. —◆— Lentil; —■— Bean; —▲— Broad Bean. All experiments use Container 3, Ramp 2 and glass surface. The axes describe the same quantities as in Figure A4.

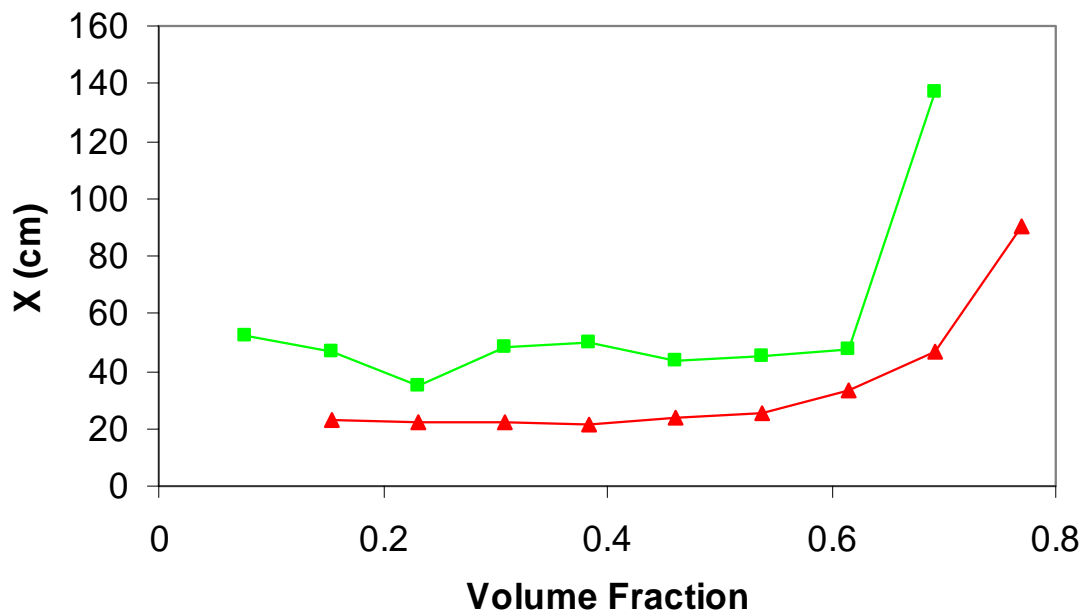


Figure A7. Effect of Surface. —■— Hard wood polished floor; —▲— carpet. All experiments with Container 3, Particle 2 and Ramp 4. Axes represent the same dimensions as in Figure A5.

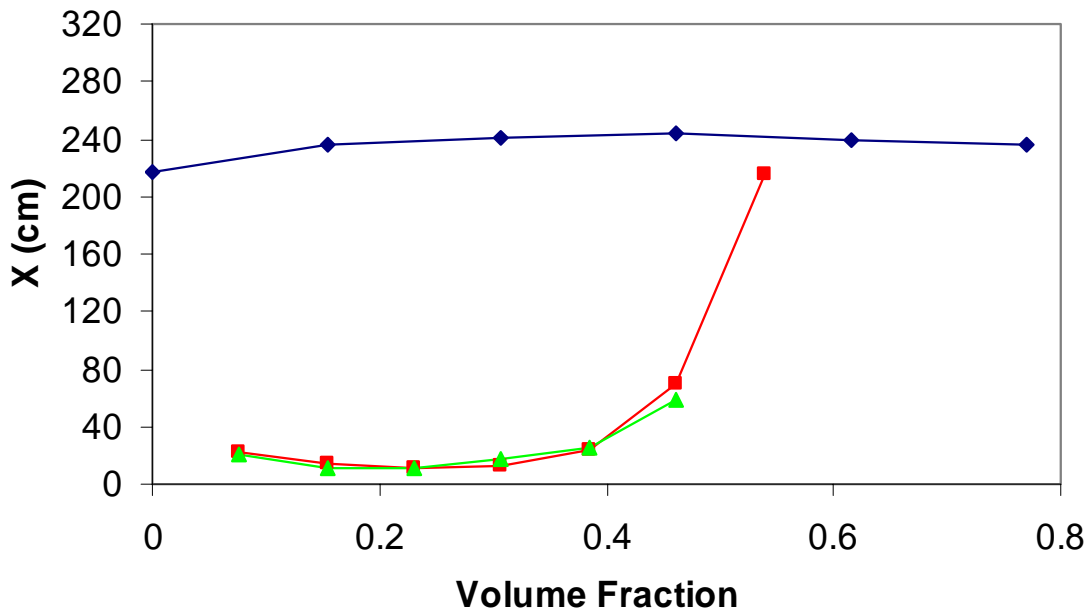


Figure A8: Comparison between perfect slide and perfect roll. —◆— Perfect slide; —■— Perfect roll, long rubber; —▲— Perfect roll, short rubber. The axes represent the same dimensions as previous figures, however X has twice the scale of Figures A4 to A7. All experiments use lentils, and Containers 3 and 4, which are identical. Ramp for perfect roll is Ramp 3.

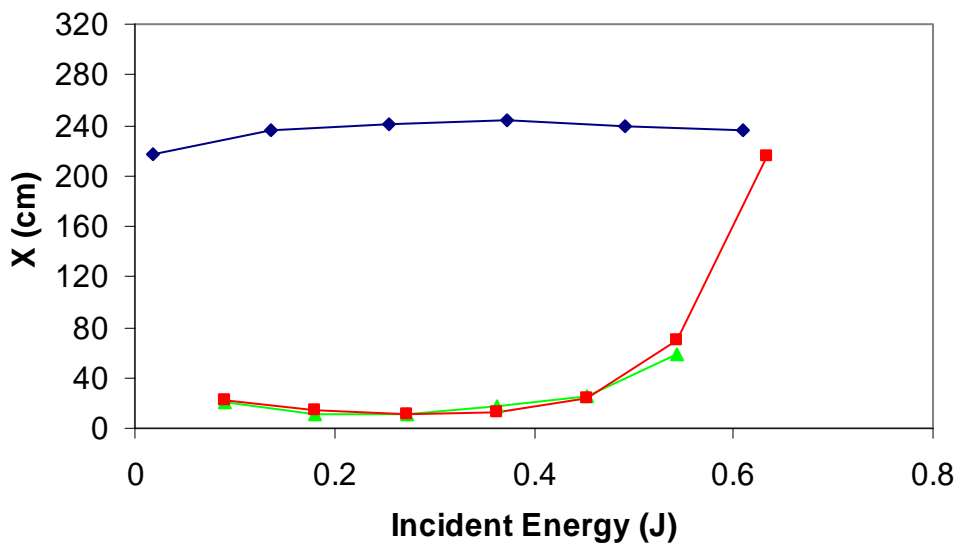


Figure A9. Potential Energy graph of Figure 8. The added mass of the car shows little change in potential energy. The Incident Energy is approximated to be the Potential Energy of the container when at rest, at the top of the ramp.

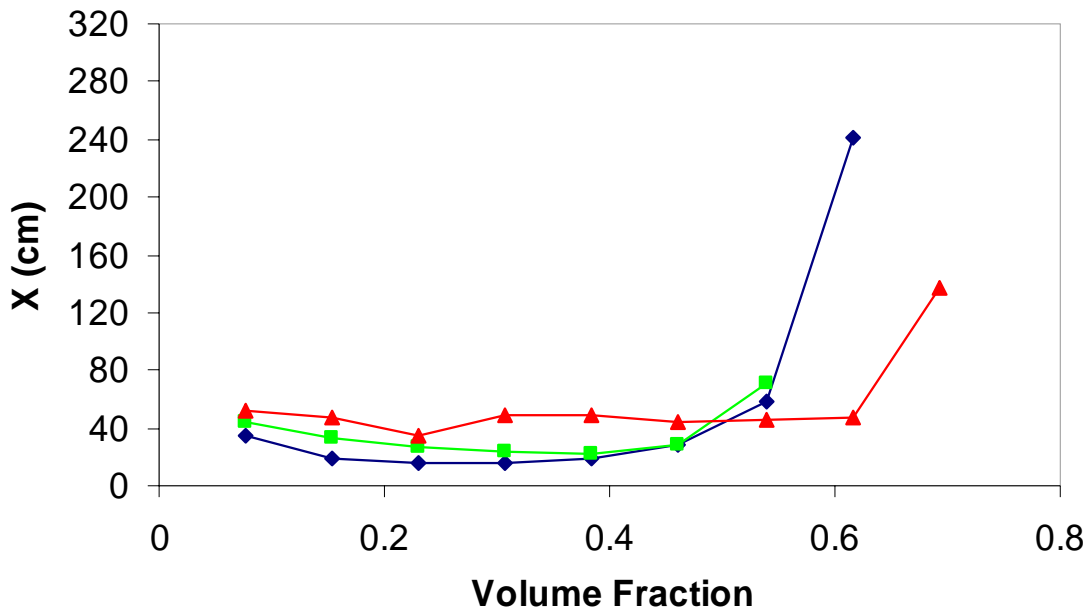


Figure A10. Effect of rubber on ramp. —◆— Long rubber; —■— Short rubber; —▲— No rubber. All experiments with Particle1, Ramp 4 and Container 3. Ramp leads onto polished floor. Axes represent the same quantities as in Figure A4. The scale of X is the same as in Figure A8.

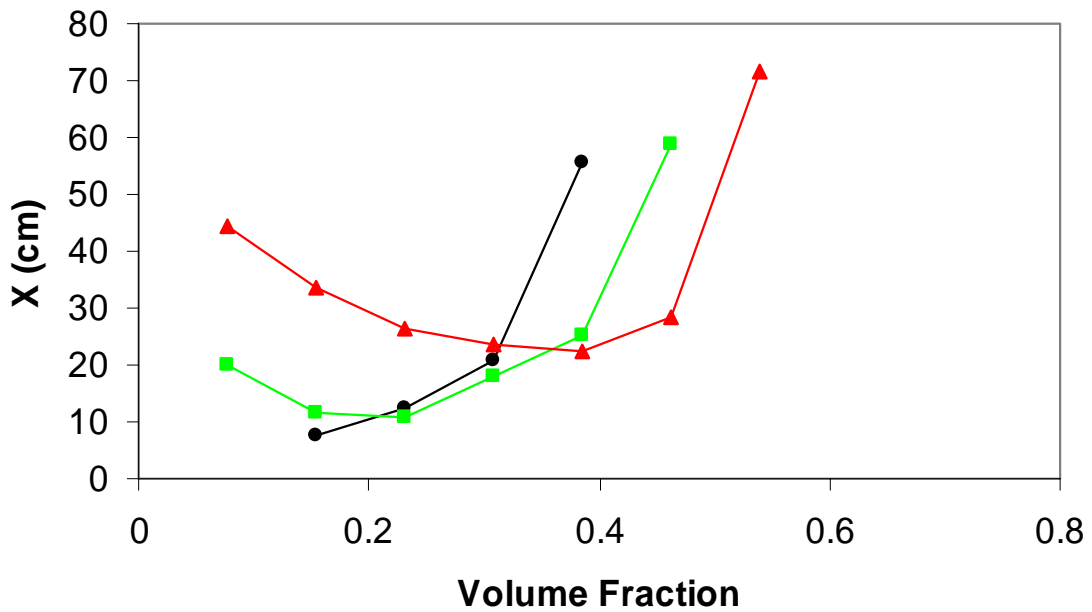


Figure A11. Comparison of particles with rubber covered ramp. —■— Particle 1; —▲— Particle 2; —●— Particle 4. All experiments with Ramp 4, covered with 50 cm. of rubber, using Container 3, on polished floor boards. Axes represent the same dimensions as Figure A4, however X range is between 0 and 80 cm, which is half the range in Figure A4

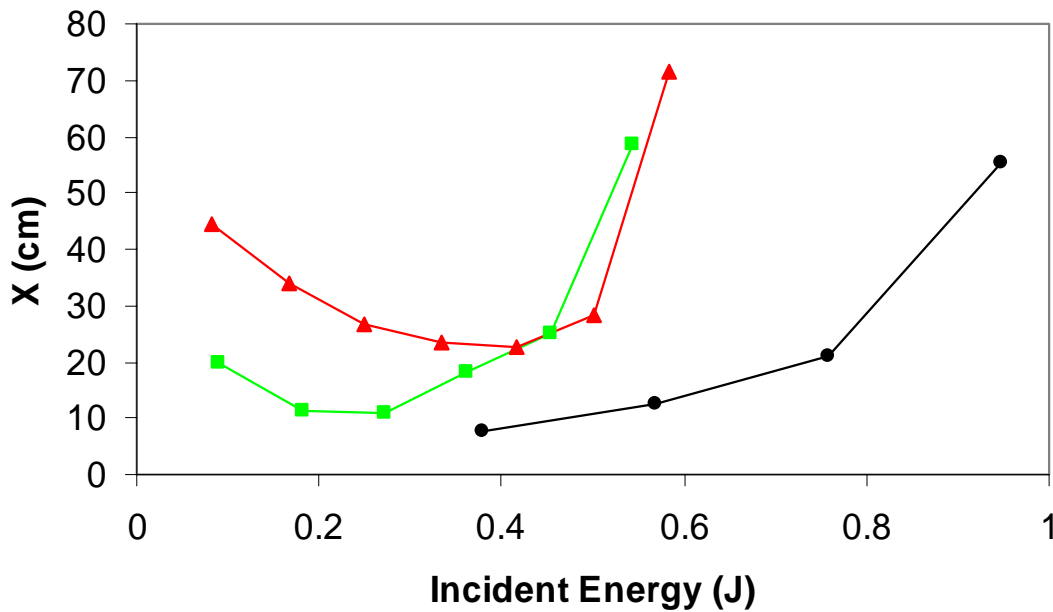


Figure A12. Comparison of Incident Energies for Figure 11. —■— Particle 1; —▲— Particle 2; —●— Particle 4. The Incident Energy is approximated to be the Potential Energy of the container when at rest, at the top of the ramp.

3.1. Visual description of experiments using sand as a particle

Sand was the most efficient energy dissipation particle. Therefore, the experiments involving sand have been repeated, and recorded. Observations regarding the motion of particles in the container, and method of dissipation of energy have been made, and are presented in the following paragraphs. These include graphical representations of the motion of particles inside the container, at various time steps.

Particles in a rolling container create waveforms during rotation and subsequent settling. These shapes are repeatable, and their presence can be defined based on important events of the experiment. One such event, defined as time ‘ t ’ is the moment when the container leaves the ramp and touches the surface. At this stage the container has already been in motion for a period of time, which varies between 10 and 12 time steps. Each time

step is $1/25$ of a second. This is because the experiments were filmed at a frame rate of 25 FPS, and observations are based on these recordings.

➤ **50 ml – 0.077 Vol. Fraction – 0.190 J incident energy**

The container rolls on the ramp for an average of 10.75 time steps. By definition, the container reaches the surface at time ' t '. Between times $(t+1)$ and $(t+4)$ two wavefronts are observed in the container. The first, 'leading wavefront' are particles which can be said are 'climbing' on the wall of the container which is in the direction of movement. The second, 'trailing wavefront' are particles which are lifted on the surface of the container that is in the opposite direction. The leading wave has a larger amplitude than the trailing wave for this time interval. The leading particle wave has a peak which is located around the midsection of the container, as viewed from the direction of motion (see Figure A13 (a)). The trailing wave has a lower amplitude, and is more uniformly distributed. In Figure A13(b) a side view of the two waves, and the trough between them, is shown.

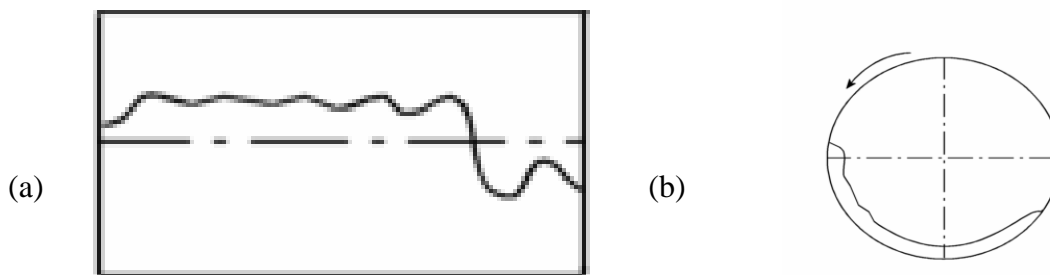


Figure A13 (a): front view of the leading wavefront. (b) side view of the container, including the amplitude of both the leading and trailing wavefronts.

Time intervals $(t+4)$ and $(t+8)$ define the collapse of the leading and trailing wavefronts (in order). This implies the particles are re-distributed evenly over the surface of the container, however equilibrium is not reached for a

while. This is evident due to the ‘rocking’ motion of the container which continues for an undetermined, but lengthy period of time (in excess of 2 seconds). In conclusion, the potential energy of the container is dissipated in $(10.75 + 8 =) 18.75/25$ seconds, which includes ramp descent time. The stopping distance averages 12 cm from the bottom of the ramp.

➤ **100 ml – 0.154 Vol. Fraction – 0.380 J incident energy**

When compared to the previous experimental case, the two wave fronts do not change significantly when the container is filled with 100 ml of sand particles. The leading wave front exists between times $(t+1)$ until $(t+4)$, while the trailing wave collapses at time $(t+7)$. Overall, the container travels $12/25$ s. on the ramp, and a further $7/25$ on the surface, for a combined total energy dissipation time of $19/25$ seconds. Importantly, both the distance travelled and the time the container experiences the ‘rocking’ motion once the rolling stops are reduced. The stopping distance is 9 cm.

➤ **150 ml – 0.231 Vol. Fraction – 0.569 J incident energy**

At this particle level, a change in the waveform of the leading wave is observed for a short period ($2/25$ s). Figure A14 (a) shows the progression of the leading wavefront for time intervals $(t+1)$, $(t+2)$ and $(t+3)$. This anomaly is unexplained, yet present in all experimental runs. Furthermore, the amplitude of the trailing wavefront from time $(t+2)$ is larger than that of the leading wavefront. The leading wavefront collapses and dissipates at time $(t+4)$, while the trailing wavefront gains amplitude until time $(t+4)$, when it folds over, and its particle mass returns to the centre of the container $(t+5)$. Figure A14 (b) shows a side view of the container for the period $(t+1)$ until $(t+5)$, and the evolution of the two wavefronts over the interval.

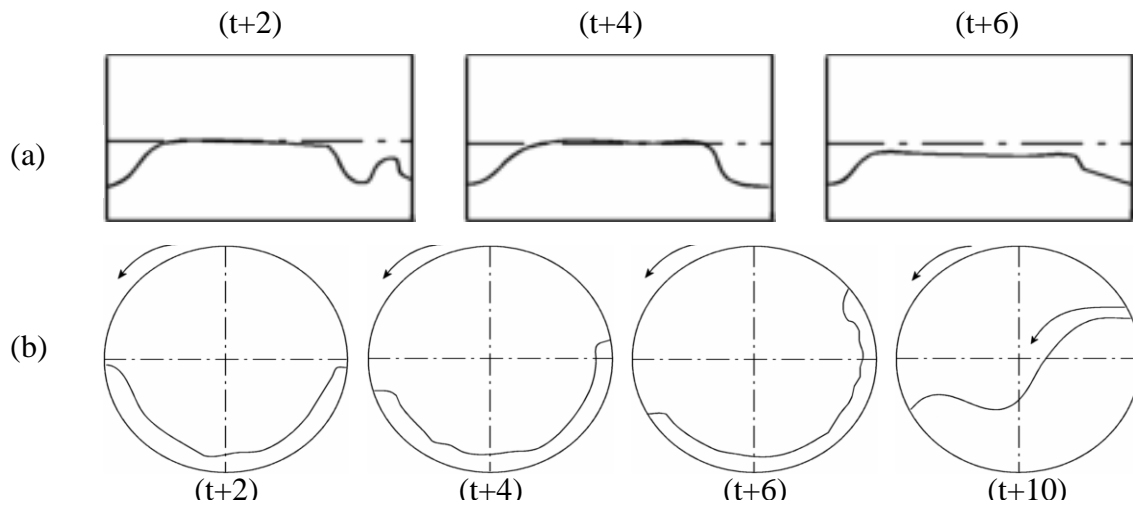


Figure A14 (a), front view of leading wave front at times $(t+1)$, $(t+2)$ and $(t+3)$,
 (b) side view of both wave fronts at times $(t+1)$, $(t+2)$, $(t+3)$ and $(t+5)$.

The folding of the trailing is interesting both visually and in terms of the effect of this large energy dissipation in one time step. Further, the rocking motion once the rolling has stopped is again observed for an extended period of time. Stopping distance is 11.5 cm, with 11.5/25 seconds on ramp and 5.5/25 seconds on surface.

➤ **200 ml – 0.308 Vol. Fraction – 0.759 J incident energy**

When the container is filled with 200 ml of sand, the distance travelled increases considerably over previous experiments. While the descent time is similar (12/25 s) the time on the surface until rest is longer. After time t , the following event takes place at two amplitude levels (initial, higher amplitude, and second, lower amplitude)

The leading wave front has low amplitude (lower than particle level at rest), while trailing wave has a very high amplitude and is ready to fold/break. This happens at $(t+2)$ (high energy) and $(t+7)$ (lower amplitude)

Breaking/folding of the trailing wave at times $(t+3)$ and $(t+8)$

After the first occurrence, because the particles have higher energies (and velocities), the particles are pushed outwards of the centre of the container and container rolls $(t+3) \Rightarrow (t+5)$. After the second occurrence, the container roll stops, however there is some rocking motion of the container $(t+8) \rightarrow (t+13)$.

In Figures A15 (a) and 15 (b) the progression of the leading and trailing wavefronts from both a side and front view are shown. They are compared to particle level at rest during the $(t+2) \rightarrow (t+3)$ and $(t+7) \rightarrow (t+8)$ intervals.

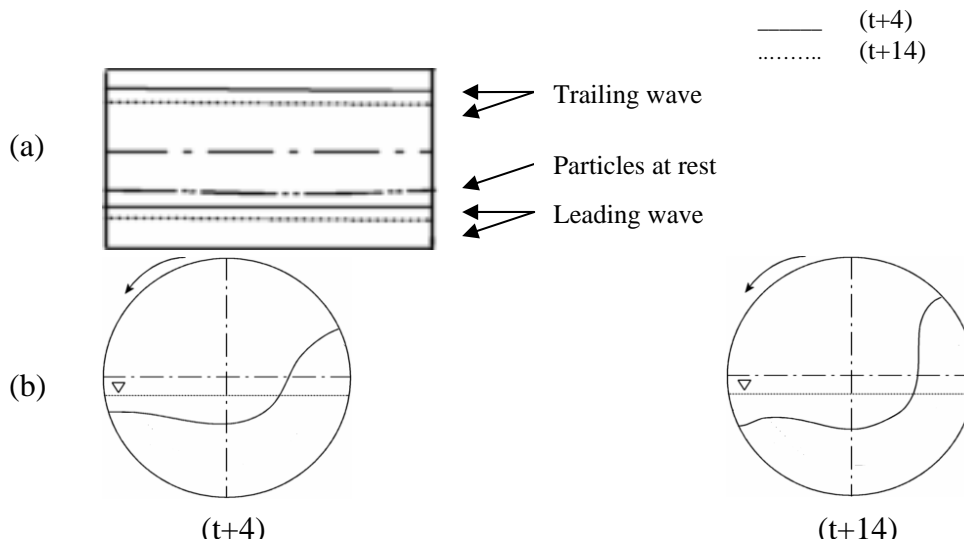


Figure A15 (a) amplitude of leading and trailing waves at times $(t+2)$ and $(t+7)$ as well as particle level when at rest. (b) side view of particles in container at times $(t+2)$ and $(t+7)$.

The most significant changes at this particle level are the increased distance travelled, the amplitude of the trailing wave is larger than that of the leading wave for significant time intervals, and dissipation of energy through the folding of the wave is observed. Interestingly, the time required for the rolling motion to dissipate the energy is similar to lower particle volumes at

20/25 seconds total time on ramp and surface. The stopping distance increases to 26 cm.

➤ **250ml – 0.385 Vol. Fraction – 0.949 J incident energy**

At 250 ml, the container is 40% full, and the stopping distance is significantly longer than previous experiments. Also, there are greater distance and time variations between individual experimental runs, some of which can be attributed to starting conditions. A generalisation based on the commonalities between the runs can be summarised as follows:

At time (t+1) the leading wavefront has a high amplitude and is followed by a lower amplitude trailing wavefront.

At time (t+2), the opposite is observed, especially during the first and fourth experimental run, where the trailing wavefront has increased in amplitude and is already breaking/folding towards the centre of the container. In the other experimental runs, this has already taken place, and the container is in the next phase, where it is rolling until time (t+13)

(t+13)->(t+20) leading wave front has lower amplitude than the trailing wave. The mass of particles forming the trailing wave is slowly collapsing.

(t+20)->(t+24) marks the settling of the particles in the container.

Interestingly, the amplitude of the trailing wave does not appear to be sufficiently large to lead to a folding of the wave during the time when the particles can be observed. Naturally, with the longer stopping distance, now there is an increase in the time required to dissipate the energy (36/25 seconds). The motion of the particles during the time (t+13) -> (t+20) leave room for speculation whether they are involved in a repeatedly collapsing

trailing wave at high velocity, or whether the centripetal acceleration dictates the position of the particles. The stopping distance increases again to 56 cm.

In summary, the most effective energy dissipation occurs when particles move inside the container and collide with other particles and walls. Furthermore, the folding of the secondary waves onto themselves provides good dissipation, for a range of volume fractions between 0.15 and 0.35. However, as the initial energy increases so does the container velocity, causing particles to move towards the surface of the container, which does not dissipate energy.

3.2. Effect of starting conditions

Ideally, all experimental runs forming an experiment enjoy identical starting conditions. During these experiments, some observations regarding initial starting conditions and their effect have been made. One of these would explain why some of the results have much higher or lower values than the average. Specifically, this correlates the angle between the free surface of particles and the ramp surface to the distance travelled. When this angle is minimised the distance travelled is shorter, while when maximised the distance increases considerably. This angle has a large variation because the friction between particles allows a large range of ‘stable’ positions. Generally, the experimenter attempted to always maintain the same angle during each set of experiments, however, as some results clearly show, some of the runs have large deviations from the mean. This is not desired, as small changes in the angle of the free surface of particles causes a significant change in the distance travelled.

4. Conclusion

Further research in the area is required to determine the means of improving the efficiency of such an absorber, as well as defining the requirements for an absorber which can be used for structural control.

At this stage, important discoveries are that by using Volume Fraction as the horizontal scale of which the vertical scale represents distance travelled, all data points of containers of different sizes using the same particle collapse onto a single line. Further, the distance travelled by the partially filled container is directly dependent on the number of particles inside. When the container is between 10 and 50% filled, it travels a shorter distance than when it has more or less than ‘this many’ particles.

Additional experiments have shown that encouraging rolling motion of the container makes for a good energy dissipater, rather than encouraging sliding motion, or simply allowing nature to take its course.

While experiments have been run in order to determine if particle size affects energy dissipation, they can only conclusively show that our smallest particle was the best dissipater for in some experiments, and that they consistently performed better than the larger particles for certain ranges of Volume Fractions. Further experiments are required to determine the relationship between the particle size and the efficiency of energy dissipation. Complementary to this, a small, dense, and densely packed particle proved to be the most efficient dissipater of all.

B.1 Undamped Tuned Vibration Absorber

A Dynamic Vibration Absorber is an auxiliary system whose properties are chosen such that it eliminates vibrations for a specific tuned frequency. These vibrations are caused by an excitation force which causes the system to vibrate excessively. In Figure B1 (a), the system to be controlled is shown with a mass of m_1 , and a total stiffness of k_1 . An absorber of mass m_2 is attached to m_1 by means of a spring k_2 . While the auxiliary system m_2, k_2 can make the amplitude of the system's oscillations zero at the tuned frequency (usually chosen as the natural frequency), it may cause another difficulty. This difficulty is associated with the addition of the new oscillator as an absorber which gives an additional resonance peak for the combined system. One of these spectral peaks is at a frequency lower and one at a frequency higher than the natural frequency of the undamped system. In Figure B1 (b), the uncontrolled response is shown with a dashed line (- -), whereas a solid line (---) indicates the response with the absorber. In this figure, vertical axis is the oscillation magnitude of the system to be controlled, X_1 , the horizontal axis is the non-dimensional oscillation frequency ratio $\frac{\omega}{\omega_1}$, ω_1 being the tuning frequency and also the natural frequency of $m_1 - k_1$. Ω_1 and Ω_2 mark the two resonances of the combined system.

The control method presented above poses a problem for machines, as during the start-up and shut-down phases, they have to pass through the lower

resonance frequency, even though ideal control is achievable at the tuning frequency $\frac{\omega}{\omega_1} = 1$.

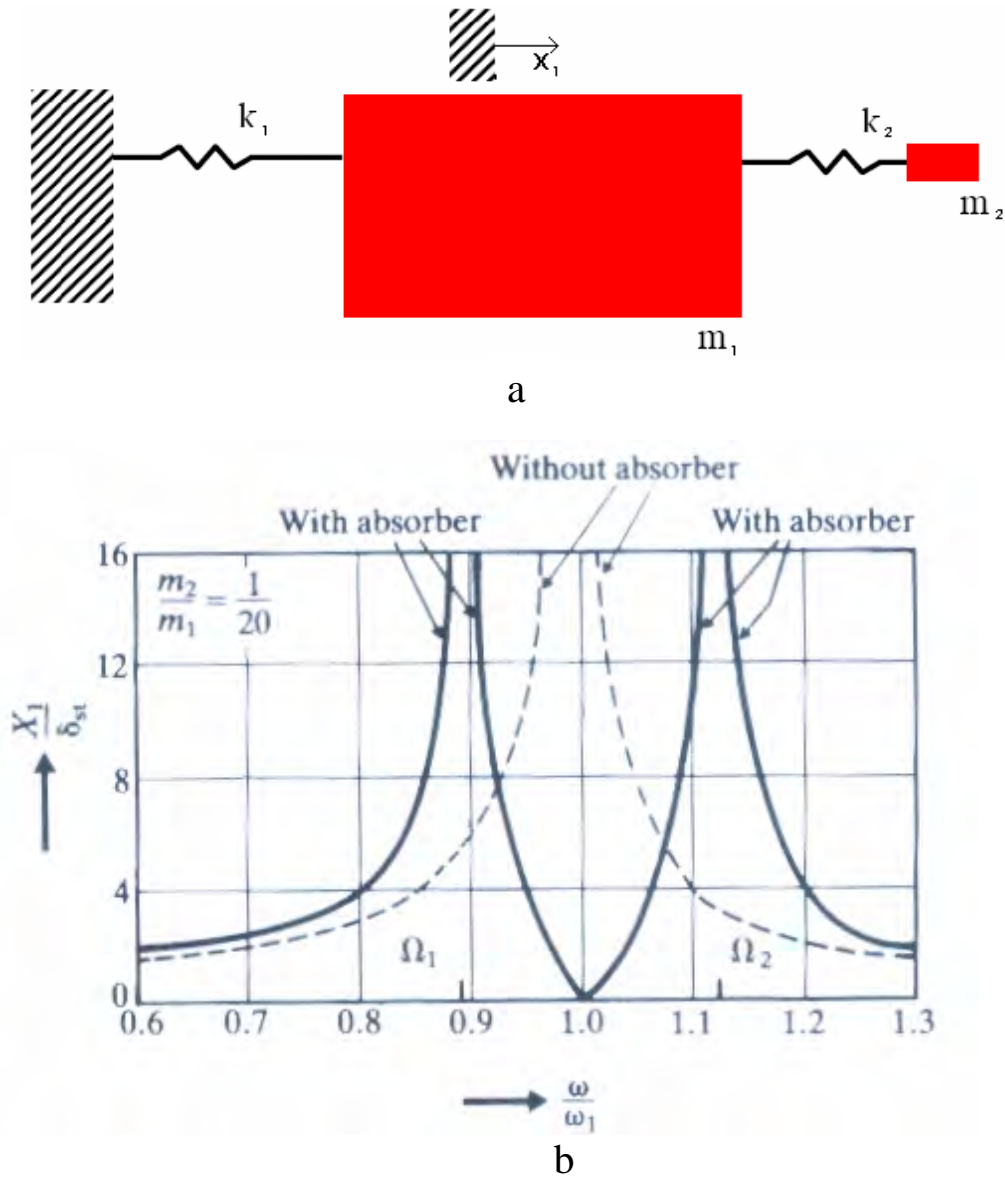
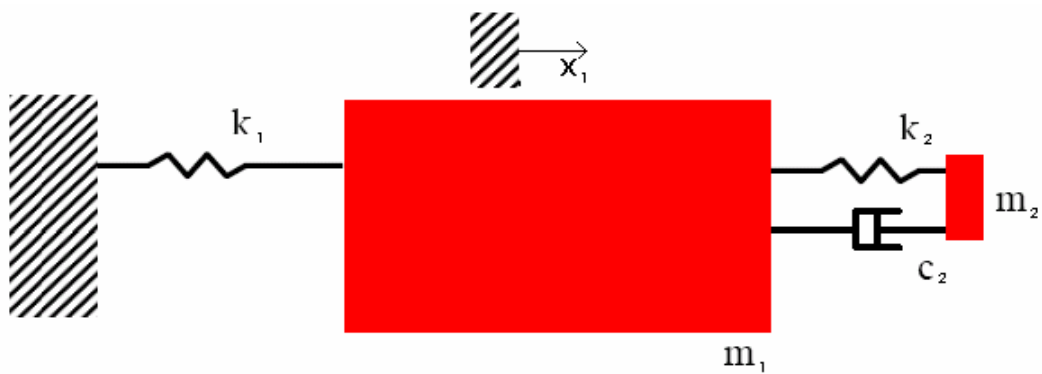


Figure B1. (a) Schematic representation of system to be controlled m_1, k_1 and absorber m_2, k_2 and (b) response amplitude X_1 of m_1 with (---) and without the absorber (- -), as a function of excitation frequency ratio, as can be seen in (Rao 1995)

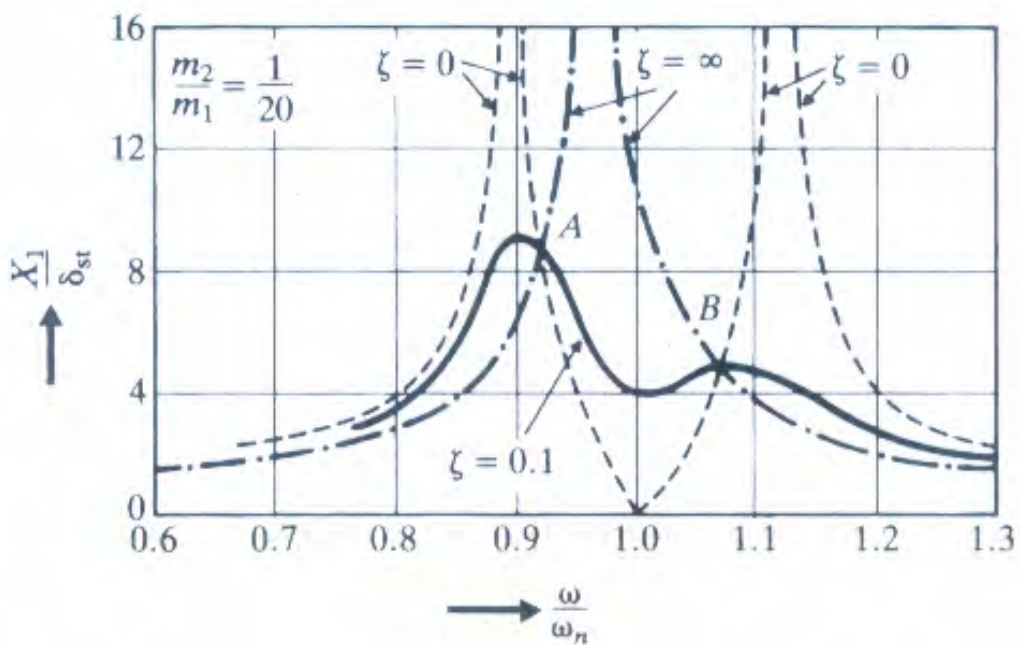
B.2 Damped Tuned Vibration Absorber

In order to minimise the large amplitude oscillations observed in Figure B1 (b), a damper may be included, as suggested in Figure B2 (a). The resulting system still has two spectral peaks which are smaller in magnitude, as compared to Figure B1 (b). In Figure B2 (b), parameter ζ indicates the level of damping, and called the critical damping ratio. The trough at $\frac{\omega}{\omega_1} = 1$, coincides with the original tuning frequency where the amplitude is zero in the undamped dynamic absorber system. Hence, addition of damping represents a trade off between the ideal tuning condition of the undamped absorber (-- --) and the smaller spectral peaks of the damped absorber (----). Points A and B in Figure B2 (b) represent the first and second location where the response lines meet. The most efficient absorber is suggested to be the one for which the ordinates for points A and B are equal (Rao 1995).

A Damped Tuned Vibration Absorber is an efficient controller and it is extensively used in the building industry. However, the damper which makes the control effective is also a high maintenance component, making the controller impractical.



a



b

Figure B2. (a) Schematic representation of system to be controlled m_1, k_1 and damped absorber m_2, k_2, c_2 and (b) response amplitude of m_1 with damped absorber (----), with undamped absorber (---), and without absorber (-.-.-), as can be seen in (Rao 1995).

B.3 Tuned Liquid Damper

Requirement of high maintenance of a damped tuned absorber may be overcome with Tuned Liquid Dampers. A Tuned Liquid Damper utilizes sloshing of a liquid inside a container in place of the auxiliary oscillator of a tuned absorber. In Figure B3, a schematic of a Liquid Sloshing Absorber is shown. The advantage of a Liquid Sloshing Absorber over a damped tuned vibration absorber comes from the low maintenance requirements of a tuned liquid damper (Anderson, 2000). Also, in buildings, an existing water storage container can be redesigned for the additional purpose of vibration absorption (Anderson, 2000).

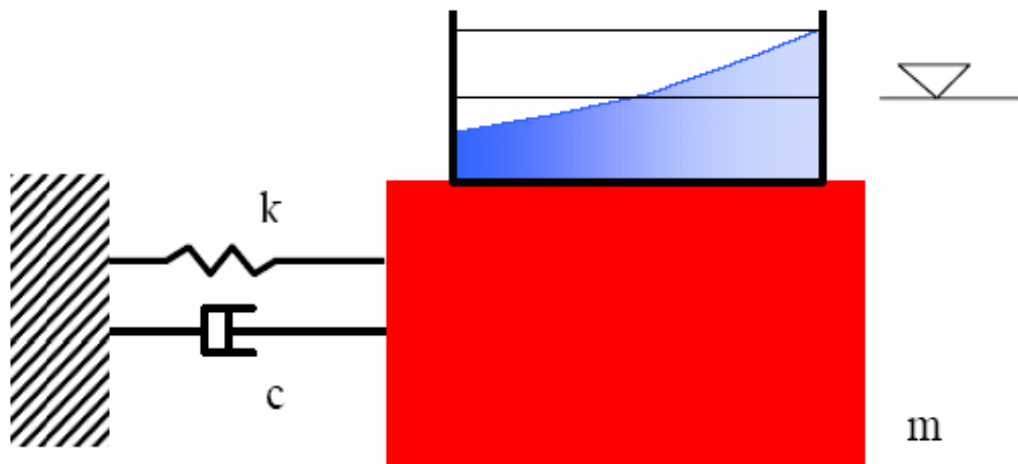


Figure B3. Schematic showing a sloshing absorber attached on a single degree of freedom mechanical oscillator

Similar to a vibration absorber, tuning a sloshing absorber involves designing the sloshing frequency to be the same as the critical natural frequency of the structure to be controlled. The sloshing frequency may be predicted using the following expression (Sakamoto et al 2001):

$$f = \frac{1}{2\pi} \sqrt{\frac{\pi g}{l} \tanh\left(\frac{\pi h}{l}\right)}$$

where g is the gravitational acceleration, while l and h are the length and height of the container, respectively. Hence, tuning a sloshing absorber involves selecting the appropriate values of the liquid depth and the length of the container.

Tuning of a Tuned Liquid Damper for multiple frequencies has been explored through the use of an Electro-Rheological fluid (Birhan et al 2004) (which changes its apparent viscosity when an electric potential is applied to it). A specially designed tank, with electrodes at one end has been used, and the length of the tank, (l in equation above) has been adjusted by solidifying the Electro-Rheological fluid between the electrodes, which adjusted the sloshing frequency.

Another method of tuning a Tuned Liquid Damper is by means of a flexible container. This work is currently under development by the research group at Victoria University and shows a possible future direction for commercial designs (Birhan et al 2004, Gradinscak et al 2004)

Appendix B: Damped Tuned Vibration Absorbers

Liquid sloshing inside a rotating container has been investigated by Rocca et al., primarily from the perspective of liquid sloshing in a satellite revolving around the Earth (Rocca et al 2000).

Methods of improving absorber efficiency are adding a wire mesh in the container, using sloped surface on the sides of the container and using a cap on the container which then employs the principles of an impact damper (Warnitchai et al 1998, Truong et al 2003, Tait et al 2006, Semercigil et al 2007, Semercigil et al 2007). Despite its positive attributes, a drawback of a Tuned Liquid Damper is that when the liquid level is comparable to the length of the container, it becomes an inefficient dissipater of energy. Such a deficiency may make it an ineffective controller.

REFERENCES

Anderson, J. G. , Semercigil S. E., and Turan, O. F.,: A standing-wave-type sloshing absorber to control transient oscillations, *Journal of Sound and Vibration*, V. 232, No. 5 (2000), pp. 839-856.

Anderson, J. G.,: *Liquid Sloshing in Containers: its Utilisation and Control*, Ph. D. Thesis, Melbourne 2000.

Barker, C. G.,: Computer simulations of granular materials, *Granular Matter, A Interdisciplinary approach*, Ed. A. Mehta, Springer, NY, 1994, pp. 35-84.

Batina, T.,: A gridless Euler/Navier-Stokes solution algorithm for complex aircraft applications, AIAA Paper 93-0333, American Institute of Aeronautics and Astronautics, 1993.

Bekdaş, G., Nigdeli, S. M.,: Estimating optimum parameters of tuned mass dampers using harmony search. *Engineering Structure*, in press. doi:10.1016/j.engstruct.2011.05.024

Belytschko, T., Lu, Y. Y., and Gu, L.,: Element free Galerkin methods, *International Journal of Numerical Methods Engineering*, 37 (1994).

Benz, W.,: Smoothed Particle Hydrodynamics: a review, in *The Numerical Modelling of nonlinear stellar pulsations - Problems and Prospects*, Kluwer Academic, 1989, p. 269.

Campbell, C. S.,: Granular material flows - An overview, *Powder Technology*, V. 162, N. 3 (2006), pp. 208-229.

References

- Chen, S. R., Chang, C. C., and Cai, C. S.,: Study on Stability Improvement of Suspension Bridge with High-Sided Vehicles under Wind using Tuned-Liquid-Damper, *Journal of Vibration and Control*, V. 14, No. 5 (2008), pp. 711-730.
- Cleary, P. W., Morrisson R., Morrell S.,: Comparison of DEM and experiment for a scale model SAG mill. *International Journal of Mineral Processing* 68 (2003), pp. 129-165
- Cleary, P. W., Sinnott, M. D.,: Assessing mixing characteristics of particle-mixing and granulation devices. *Particuology* 6 (2008), pp. 419-444
- Cleary, P. W.,: Predicting charge motion, power draw, segregation, wear and particle breakage in ball mills using discrete element methods, *Minerals Engineering*, 11 (1998), pp. 1061-1080.
- Cleary, P. W.,: Recent advances in DEM modelling in tumbling mills, *Minerals Engineering*, 14 (2001), pp. 1295-1319.
- Cleary, P. W.,: The effect of particle shape on simple shear flows, *Powder Technology*, 179 (2008), pp. 144-163.
- Dragomir, S. C., Semercigil, E. S., Turan, O. F.,: Induced particle sloshing in a rotating container. *Proceedings of the 16TH Australasian Fluid Mechanics Conference*, 2007, pp. 1207-1212
- Dragomir, S. C., Semercigil, S. E., and Turan, Ö. F.,: Induced Particle Sloshing in Rotating Container, Report No. MEDV071 Victoria University.
- Dragomir, S. C., Sinnott M., Semercigil, E. S., Turan, O. F.,: Energy dissipation characteristics of particle sloshing in a rotating cylinder. *Journal of Sound and Vibration*, Vol. 331, Iss. 5, 2012.

References

Dragomir, S.C., Sinnott M., Semercigil, E. S., Turan, O. F.,: Predicting Energy Dissipation Characteristics of a Tumbling Granular-Flow Damper Using DEM, 7th International Conference on CFD in the Minerals and Process Industries, December 2009.

Dragomir, S. C., Sinnott M., Semercigil, E. S., Turan, O. F.,: Energy dissipation characteristics of a granular flow damper. Proceedings of the 17TH Australasian Fluid Mechanics Conference, 2010

Dragomir, S. C., Sinnott M., Semercigil, E. S., Turan, O. F., Critical speed and energy dissipation in a rotating cylinder, *Granular Matter*, (under consideration 2012).

Dury, C. M., Ristow, G. H.,: Boundary effects on the angle of repose in rotating cylinders. *Physical Review E* 57 (1997), pp. 4491 – 4497

Fischer, O.,: Wind-excited vibrations – Solution by passive dynamic vibration absorbers of different types. *Journal of Wind Engineering and Industrial Aerodynamics* 95 (2007), pp. 1028-1039

Fiscoa, N. R., Adeli, H.,: Smart structures: Part I—Active and semi-active control. *Scientia Iranica*, in press. doi:10.1016/j.scient.2011.05.034

Gradinscak, M., Güzel, B. U., Semercigil, S. E., and Turan, Ö. F.,: Control of liquid sloshing in flexible containers: part 2. Top straps, in 15th Australian Fluid Mechanics Conference, Sydney 2004.

Greenspan, D.,: A particle model of fluid sloshing, *Mathematical and Computer Modeling* 41 (2005), pp. 749-757.

References

- Güzel, B.U., Gradinscak, M., Semercigil, S. E., and Turan, Ö. F.:. Control of liquid sloshing in flexible containers: part 1. Added mass, in 15th Australian Fluid Mechanics Conference, Sydney 2004.
- Güzel, B.U., Prakash, M., Semercigil, S. E., and Turan, Ö. F.:. Energy dissipation with sloshing for absorber design, Proceedings of American Society of Mechanical Engineers, Orlando 2005.
- Koshizuka, S., Ikeda, H., and Oka, Y.:. Numerical simulation of fragmentation processes in vapor explosions using moving particle semi-implicit method, in Proceedings of International Meeting on Advanced Reactors Safety, Florida 1997.
- Koshizuka, S., Tamako, H., and Oka, Y.:. A particle method for incompressible viscous flow with fluid fragmentation, Computational Fluid Dynamics Journal, 4 (1995), pp. 29-46.
- La Rocca, M., Sciortino, G., and Boniforti, M.:. A fully nonlinear model for sloshing in a rotating container, Fluid Dynamics Research, 27 (2000), pp. 23-52.
- Liu, K. and Liu, J.:. The damped dynamic vibration absorbers: revisited and new result, Journal of Sound and Vibration, 284 (2005), pp. 1181-89.
- Lochner, R. H., Matar, J. E.:. Designs for Quality. White Plains, N. Y., American Society of Quality Control. S., 1990
- Mao, K., Wang, M.Y., Xu, Z., and Chen, T.:. DEM simulation of particle damping, Powder Technology, 142 (2004), pp. 154-165.
- Monaghan, J. J.:. An introduction to SPH, Comput. Phys. Commun., 48 (1988).

References

- Ottino, J. M., Khakhar D. V.,: Mixing and Segregation of Granular Materials. *Annu. Rev. Fluid Mech.* 33 (2000), 55-91
- Panossian, H. V.,: An overview of NOPD: a passive damping technique, *Shock and Vibration*, 6 (1991), pp. 4-10.
- Panossian, H. V.,: Structural damping enhancement via non-obstructive particle damping technique, *Journal of Vibration and Acoustics*, 114 (1992), pp. 101-105.
- Papalou, A., and Masri, S.F.,: Response of impact dampers with granular materials under random excitation, *Earthquake Engineering and Structural Dynamics*, V. 25 (1996), pp. 253-267.
- Rao, S.S.,: *Mechanical Vibrations*, Third Ed., Adison Wesley, 1995, Ch. 9.
- Ristow, G. H.,: *Flow Properties of Granular Materials in Three-Dimensional Geometries*. Philipps University, 1998, pp. 63–92
- Rose H. E., Sullivan, R. M. E.,: *A Treatise on the Internal Mechanics of Ball Tube and Rod Mills*. Constable, London, 1958
- Sakamoto, D., Osima, N., and Fukuda, T.,: Tuned sloshing damper using electro-rheological fluid, *Smart Materials and Structures*, 10 (2001), pp. 963-969.
- Semercigil, S. E., Turan, Ö. F., and Kopp, G. A.,: Tuning a sloshing absorber by designating its slope alone, to be submitted to *Journal of Wind Engineering*, 2007.

References

Semercigil, S. E., Turan, Ö. F., Kopp, G. A., and Terrés-Nicoli, J.M.: A sloshing absorber for limiting torsional buffeting oscillations of a long-span bridge deck, to be submitted to *Journal of Wind Engineering*, 2007.

Sinnott, M, Cleary, P. W., and Morrison, R.: Analysis of stirred mill performance using DEM simulation: Part 1 - Media motion, energy consumption and collisional environment, *Minerals Engineering*, 19, (2006), pp. 1537-1550

Snowdon, J. C.: *Vibration and Shock in Damped Mechanical Systems*, 1968, John Wiley & Sons, Inc. New York.

Souto-Iglesias, A., Delorme, L., Perez-Rojas, L. and Abril-Perez, S.: Liquid moment amplitude assessment in sloshing type problems with smoothed particle hydrodynamics, *Ocean Engineering*, 33 (2006), pp. 1462-1484.

Steidel Jr, R.F.: *An Introduction to Mechanical Vibrations*, Third Ed., J. Wiley & Sons, 1989.

Tait, M.J., Isyumov, N., and Damatty, A.A.: Tuned Liquid Dampers to mitigate wind-induced motions of buildings, in *Proceeding of Structures Congress*, St. Louis 2006.

Tamura Y., Kohsaka R., Nakamura, O., Miyashita K., and Modi V. J.: Wind-induced responses of an airport tower - efficiency of tuned liquid damper, *J. Wind Eng. Ind. Aerodyn.*, V. 65, (1996), pp. 121-131.

Troung, T. D., Semercigil, S. E., Turan, Ö. F.: Turan, Experiments for control of structural oscillations using free and restricted sloshing waves, *Journal of Sound and Vibration*, 264 (2003), pp. 235-244.

References

Walton, O. R., Braun, R. L.,: Proceedings of the joint DOE/NFS workshop on the flow of particulates and fluids, Ithaca, New York, 1993

Walton, O. R.,: Numerical simulation of inelastic frictional particle-particle interaction, Particulate two-phase flow, Ed. M. C. Roco, Butterworth-Heinemann, 1992, pp. 884-911.

Warnitchai, P., and Pinkaew, T.,: Modeling of liquid sloshing in rectangular tanks with flow-dampening devices, Engineering structures, 20 (1998), pp. 563-600.

Watanabe, H.,: Critical rotation speed for ball-milling. Powder Technology 104 (1999), 95-99

Wong, C.X., Daniel, M.C., and Rongong, J.A.,: Energy dissipation prediction of particle dampers, Journal of Sound and Vibration, 319 (2009), pp. 91-118.

Xu, Z., Yang M.Y., and Chen, T.,: Particle damping for passive vibration suppression: numerical modelling and experimental investigation, Journal of Sound and Vibration, 279 (2005), pp. 1097-1120.

Yoon, H. Y., Koshikuza, S., and Oka, Y.,: A particle-gridless hybrid method for incompressible flow, International Journal of Numerical Methods in Fluids, 30 (1999) pp. 407-424.